

**Risk Assessment of Submarine Slope
Stability - Hydroplaning**

by

**Stephen G. Wright, Professor, Geotechnical Engineering
Hongrui Hu, Graduate Research Assistant
University of Texas at Austin**

**Final Project Report
Prepared for the Minerals Management Service
Under the MMS/OTRC Cooperative Research Agreement
1435-01-04-CA-35515
Task Order 39323
MMS Project Number 556**

February 2007

OTRC Library Number: 2/07B178

“The views and conclusions contained in this document are those of the authors and should not be interpreted as representing the opinions or policies of the U.S. Government. Mention of trade names or commercial products does not constitute their endorsement by the U. S. Government”.



For more information contact:

Offshore Technology Research Center

Texas A&M University
1200 Mariner Drive
College Station, Texas 77845-3400
(979) 845-6000

or

Offshore Technology Research Center

The University of Texas at Austin
1 University Station C3700
Austin, Texas 78712-0318
(512) 471-6989

A National Science Foundation Graduated Engineering Research Center

Table of Contents

Table of Contents	i
Executive Summary	vi
Chapter 1: Introduction	1
Chapter 2: Background	3
2.1 Previous Research on General Hydroplaning	3
2.2 Experimental Study on hydroplaning of subaqueous slides	4
2.3 Analytical Solution on Hydroplaning of Subaqueous Slides.....	8
2.3.1 Dynamic Lubrication Theory.....	8
2.3.2 Harbitz et al.'s Solution	12
2.4 Numerical Models on Post-Initiation Movement of Subaqueous Slides	15
2.4.1 Numerical Models involving No Hydroplaning	15
2.4.1.1 Lumped mass models.....	16
2.4.1.2 Miao, et al.'s model	16
2.4.1.3 Continuum models	16
2.4.1.4 Fluid models.....	16
2.4.1.5 Disadvantage of models involving no hydroplaning	18
2.4.2 De Blasio, et al.'s Model.....	19
2.5 Examination of Previous Research on Hydroplaning of Slides.....	21
2.5.1 Examination of Harbitz et al.'s solution	21
2.5.1.1 Numerical method.....	21
2.5.1.2 Numerical results	24
2.5.1.3 MODIFICATION OF HARBITZ ET AL.'S SOLUTION	28
2.5.1.4 Limitations of Harbitz et al.'s solution	32
2.5.2 Examination of on-set condition for hydroplaning.....	32
2.6 Future Research on hydroplaning of subaqueous slides	34
Chapter 3: Study of Hydrodynamic Stresses	35
3.1 Numerical Model	35
3.2 Numerical Cases	41
3.3 Numerical Results.....	41
3.3.1 Hydrodynamic Stresses.....	42
3.3.1.1 Kinetic pressures.....	46
3.3.1.2 Reexamination of the on-set condition of hydroplaning.....	47
3.3.1.3 Viscous shears.....	48
3.3.2 Effect of Inflow Velocity	51
3.3.2.1 Effect of inflow velocity on kinetic pressures	51
3.3.2.2 Effect of inflow velocity on viscous shears	51
3.3.3 Effect of Distance between the Bottom Surface of the Slide Mass and Underlying Ground.....	54
3.3.3.1 Effect of distance h on kinetic pressures	54
3.3.3.2 Effect of distance h on viscous shears.....	65
3.3.3.3 Summary on the effect of distance h	72
3.3.4 Effect of Hydroplaning	72
3.3.4.1 Effect of hydroplaning on kinetic pressures	74
3.3.4.2 Effect of hydroplaning on viscous shears	75

3.3.5 Effect of Height-to-Width Ratio	76
3.3.5.1 Effect of height-to-width ratio H/w on kinetic pressures	79
3.3.5.2 Effect of height-to-width ratio H/w on the on-set condition of hydroplaning	80
3.3.5.3 Effect of height-to-width ratio H/w on viscous shears	81
3.3.5.4 Discussions	81
3.4 Conclusions	82
Chapter 4: Development of Block Model for Subaqueous Slides involving Hydroplaning	84
4.1 Governing Equations of Motion	84
4.2 Occurrence of Hydroplaning	85
4.3 Forces on Block	87
4.3.1 Effective Weight	89
4.3.2 Kinetic Pressure	89
4.3.2.1 Along the leading edge	90
4.3.2.2 Along the trailing edge	90
4.3.2.3 Along the top surface	90
4.3.2.4 Along the bottom surface	91
4.3.3 Viscous Shear	93
4.3.4 Support by Underlying Ground	93
4.3.5 Resistance by Underlying Ground	95
4.3.6 Damping Effect	95
4.3.6.1 Kinetic damping	95
4.3.6.2 Soil damping	98
4.4 Time Integration Scheme	99
4.4.1 Initial Conditions	99
4.4.2 Newmark Scheme	99
4.5 Implementation	101
4.5.1 Input and Output	101
4.5.2 Flow Chart	103
4.6 Summary	108
Chapter 5: Validation of the Block Model	109
5.1 Experimental Conditions	109
5.2 Input parameters	111
5.2.1 Parameters Determined Directly	113
5.2.2 Parameters determined by trial and error	114
5.3 Comparison of Numerical Results with Experimental Data	115
5.3.1 Front Velocity vs Run-out Distance	115
5.3.2 Occurrence of Hydroplaning	117
5.4 Conclusions	120
5.5 Sequence of Sliding Stages	120
Chapter 6: Summary and Conclusions	123
6.1 Summary of Work	123
6.2 Conclusions	124
6.3 Suggestions on Future Research	126
References	128

List of Tables and Figures

Table 2.1: Properties of sliding mass used in experimental studies of hydroplaning.....	6
Table 2.2: Setup of experiments and observations	7
Table 2.3 Input parameters and their physical meanings.....	22
Table 2.4 Output variables and their physical meanings	22
Table 2.5 Input conditions for numerical cases	25
Table 3.1: Flow conditions and functions for numerical cases.....	41
Table 4.1. Possible stresses on the block.....	88
Table 4.2 Input parameters and physical meanings.....	102
Table 4.3 Output variables and physical meanings	103
Table 4.4 Parameters in subroutine force and their physical meanings.....	105
Table 5.1 Input parameters for experimental cases	110
Table 5.2 Input parameters for block model.....	112
Table 5.3 Trial for length-to-height ratio L/H	115
Table 5.4 Ranges of run-out distance over which the block hydroplanes	120
Fig. 2.1 2-D flow between plates.....	9
Fig. 2.2 Stresses on an element of fluid.....	9
Fig. 2.3 Steady-state hydroplaning of a sliding block on a slope	13
Fig. 2.4 Major variables for Harbitz et al.'s solution.....	14
Fig. 2.5 Forces and moments on the hydroplaning block.....	14
Fig. 2.6 Imran et al.'s model of slides	17
(a) Coordinate system and geometry of the slide mass.....	19
(b) Geometry of the wedge between the slide mass and underlying ground.....	19
Fig. 2.7 Geometry and coordinate system for De Blasio, et al.'s model	19
Fig. 2.8 Flow chart of program noproessure.cpp.....	24
Fig. 2.9 Calculated length of the block using Harbitz et al.'s solution.....	26
Fig. 2.10 Calculated height of the block using Harbitz et al.'s solution.....	26
Fig. 2.11 Calculated velocity of the block using Harbitz et al.'s solution.....	27
Fig. 2.12 Calculated flow rate between the bottom surface of block and underlying ground using Harbitz et al.'s solution	27
Fig. 2.13 Calculated length of the block using Harbitz et al.'s original solution and modified solution	29
Fig. 2.14 Calculated height of the block using Harbitz et al.'s original solution and modified solution	29
Fig. 2.15 Calculated velocity of the block using Harbitz et al.'s original solution and modified solution	30
Fig. 2.16 Calculated flow rate between the bottom surface of block and underlying ground using Harbitz et al.'s original solution and modified solution	30
Fig. 2.17 Variation of the ratios R_{add}/R with slope angle ϕ	31
Fig. 2.18 Variation of the ratios L/H with slope angle ϕ	31
Fig. 3.1 Geometry of the numerical model.....	38

Fig. 3.2 Front of the slide mass.....	39
Fig. 3.3 Curve from point <i>I</i> to point <i>S</i>	39
Fig. 3.4 Curve from point <i>I</i> to point <i>J</i>	39
Fig. 3.5 Boundary conditions for the numerical model	40
Fig. 3.6 Geometry for Case 1 ($U = 1 \text{ m/s}$; $h = 0.01 \text{ m}$; $H/w = 0.5$)	43
Fig. 3.7 Boundary conditions for Case 1 ($U = 1 \text{ m/s}$; $h = 0.01 \text{ m}$; $H/w = 0.5$).....	44
Fig. 3.8 Mesh for Case 1 ($U = 1 \text{ m/s}$; $h = 0.01 \text{ m}$; $H/w = 0.5$)	45
Fig. 3.9 Non-dimensional kinetic pressures for Case 1($U = 1 \text{ m/s}$; $h = 0.01 \text{ m}$; $H/w = 0.5$)	49
Fig. 3.10 Non-dimensional shear stress for Case 1($U = 1 \text{ m/s}$; $h = 0.01 \text{ m}$; $H/w = 0.5$)	50
Fig. 3.11 Non-dimensional shear stress for Case 1($U = 1 \text{ m/s}$; $h = 0.01 \text{ m}$; $H/w = 0.5$) and Case 2($U = 10 \text{ m/s}$; $h = 0.01 \text{ m}$; $H/w = 0.5$).....	52
Fig. 3.12 Non-dimensional shear stress for Case 2($U = 10 \text{ m/s}$; $h = 0.01 \text{ m}$; $H/w = 0.5$)	53
Fig. 3.13 Non-dimensional kinetic pressure for Case 3($U = 1 \text{ m/s}$; $h = 0.02 \text{ m}$; $H/w = 0.5$)	56
Fig. 3.14 Non-dimensional kinetic pressure Case 4($U = 1 \text{ m/s}$; $h = 0.05 \text{ m}$; $H/w = 0.5$)	57
Fig. 3.15 Non-dimensional kinetic pressure for Case 5($U = 1 \text{ m/s}$; $h = 0.1 \text{ m}$; $H/w = 0.5$)	58
Fig. 3.16 Non-dimensional kinetic pressure for Case 6($U = 1 \text{ m/s}$; $h = 1 \text{ m}$; $H/w = 0.5$)	59
Fig. 3.17 Non-dimensional kinetic pressure for Case 7($U = 1 \text{ m/s}$; $h = 10 \text{ m}$; $H/w = 0.5$)	60
Fig. 3.18 Non-dimensional kinetic pressure for Case 8($U = 1 \text{ m/s}$; $h = 50 \text{ m}$; $H/w = 0.5$)	61
Fig. 3.19 Change of non-dimensional kinetic pressure with distance h	62
Fig. 3.20 Marked non-dimensional kinetic pressures vs h/H	63
Fig. 3.21 Non-dimensional kinetic pressure at tail end of the slide mass vs h	64
Fig. 3.22 Non-dimensional shear stress for Case 3($U = 1 \text{ m/s}$; $h = 0.02 \text{ m}$; $H/w = 0.5$)	66
Fig. 3.23 Non-dimensional shear stress for Case 4($U = 1 \text{ m/s}$; $h = 0.05 \text{ m}$; $H/w = 0.5$)	67
Fig. 3.24 Non-dimensional shear stress for Case 5($U = 1 \text{ m/s}$; $h = 0.1 \text{ m}$; $H/w = 0.5$)	68
Fig. 3.25 Non-dimensional shear stress for Case 6($U = 1 \text{ m/s}$; $h = 1 \text{ m}$; $H/w = 0.5$)	69
Fig. 3.26 Non-dimensional shear stress for Case 7($U = 1 \text{ m/s}$; $h = 10 \text{ m}$; $H/w = 0.5$)	70

Fig. 3.27 Non-dimensional shear stress for Case 8($U = 1 \text{ m/s}$; $h = 50 \text{ m}$; $H/w = 0.5$)	71
Fig. 3.28 Geometry for Case 9($U = 1 \text{ m/s}$; $h = 0$; $H/w = 0.5$)	73
Fig. 3.29 Boundary conditions for Case 9($U = 1 \text{ m/s}$; $h = 0$; $H/w = 0.5$)	73
Fig. 3.30 Mesh for Case 9($U = 1 \text{ m/s}$; $h = 0$; $H/w = 0.5$)	74
Fig. 3.31 Non-dimensional kinetic pressure for Case 9($U = 1 \text{ m/s}$; $h = 0$; $H/w = 0.5$)	75
Fig. 3.32 Non-dimensional shear for Case 9($U = 1 \text{ m/s}$; $h = 0$; $H/w = 0.5$)	75
Fig. 3.33 Geometry for Case 10($U = 1 \text{ m/s}$; $h = 0$; $H/w = 2.0$)	77
Fig. 3.34 Mesh for Case 10($U = 1 \text{ m/s}$; $h = 0$; $H/w = 2.0$)	78
Fig. 3.35 Non-dimensional pressures for Case 9 ($U = 1 \text{ m/s}$; $h = 0$; $H/w = 0.5$) and Case 10 ($U = 1 \text{ m/s}$; $h = 0$; $H/w = 2.0$)	79
Fig. 3.36 Front portion of the surface for Case 9 ($U = 1 \text{ m/s}$; $h = 0$; $H/w = 0.5$)	80
Fig. 3.37 Front portion of the surface for Case 10 ($U = 1 \text{ m/s}$; $h = 0$; $H/w = 2.0$)	80
Fig. 3.38 Non-dimensional shear for Case 10 ($U = 1 \text{ m/s}$; $h = 0$; $H/w = 2.0$)	81
Fig. 4.1 Geometry and coordinate system for the block model	84
Fig. 4.2 Distance between the block and underlying ground	86
Fig. 4.3 Forces on the block	89
Fig. 4.4 Local coordinate system for the block model	90
Fig. 4.5 The distribution of pressure p_t along the top surface of the block	91
Fig. 4.6 Springs between the block and underlying ground	94
Fig. 4.7 Force-displacement curve of the springs	94
Fig. 4.8 Hydrodynamic stresses producing kinetic damping effect	96
Fig. 4.9 Kinetic pressure \tilde{p}_b for $h_f = h_t$ and $\theta = 0$	97
Fig. 4.10 Flow chart of program rect1.cpp	104
Fig. 4.11 Flow chart of subroutine force	107
Fig. 5.1 Reported front velocity vs run-out distance (Mohrig, et al. (1999))	110
Fig. 5.2 Frontal shape of the sliding soil mass (Mohrig, et al. 1999)	113
Fig. 5.3 Front velocity vs run-out distance for Run 3w	115
Fig. 5.4 Front velocity vs run-out distance for Run 1w	116
Fig. 5.5 Front velocity vs run-out distance for Run 2w	116
Fig. 5.6 Front velocity vs run-out distance for Run 4w	117
Fig. 5.7 Front velocity vs run-out distance for Run 5w	117
Fig. 5.8 Displacements h_f and h_t vs run-out distance for Run 1w	118
Fig. 5.9 Displacements h_f and h_t vs run-out distance for Run 2w	118
Fig. 5.10 Displacements h_f and h_t vs run-out distance for Run 3w	119
Fig. 5.11 Displacements h_f and h_t vs run-out distance for Run 4w	119
Fig. 5.12 Displacements h_f and h_t vs run-out distance for Run 5w	120
Fig. 5.13 Sequence of sliding stages for Run 1w	122

Executive Summary

A number of submarine landslides have traveled large distances (100 kilometers or more) once the slide movement was initiated. A growing amount of evidence suggests that one of the reasons for the relatively large travel distances is that the slide mass hydroplanes on a layer of water as the slide movement progresses. Several theoretical models have been developed to simulate this process of hydroplaning and confirm hydroplaning as a viable mechanism for slide movements. However, the theoretical models have generally made simplifying assumptions regarding how the fluid surrounding a slide mass interacts with the moving soil. The study described in this report was undertaken to understand better the fluid-slide mass interaction and develop a better representation of the hydrodynamic forces acting on a moving slide mass.

Numerical modeling, using commercially available fluid modeling software (FLUENT), was carried out to study the fluid forces on a slide mass. The analyses showed that there is a significant “lift” effect that the surrounding fluid exerts on the slide mass. This lift effect has not been considered in any of the previous models for slide hydroplaning.

Once the hydrodynamic forces on a moving slide mass were understood better, simplified representations of these forces were developed. These representations were then incorporated into a “block” model of the moving slide (soil) mass to simulate the movement of a slide through water, including the formation of a fluid layer between the slide mass and underlying parent material. Once the numerical model for the moving slide mass was developed it was used to simulate soil movements measured in a previous investigation with a series of laboratory-scale model tests. Results of the numerical model developed in the present study were found to agree well with the experimental observations. This good agreement seems to confirm the likelihood that some submarine slides may hydroplane and travel relatively large distances.

The model has not yet been exercised to examine how predicted slide movements might compare with actual field observations. Although all the data necessary to conduct simulations of actual slides is often not available, some comparisons should be feasible

and would provide a valuable confirmation of the model development to date and help guide further developments. These comparisons are recommended as the next step for future studies.

Lastly, the model that has been developed considers the slide mass as a rigid block because of the complexity of the fluid-slide mass interaction. This approach was convenient for developing a computer program to model the progression of slide movements, including the motion of the block, the interaction with the surrounding fluid, and the eventual onset of hydroplaning. For the slide motion prior to the onset of hydroplaning, the interaction with the slide mass and underlying soil foundation was also included. However, the current model developed does not consider deformation of the moving slide mass itself, including the possible separation of portions of the slide mass from each other as they move. There is some evidence from actual slides that this aspect of the movement may also be important and can have an effect on when slide movement stops. Also, the existing model uncouples the soil and water motions, while in actuality the motions are fully coupled. Further studies are still needed to develop a model that includes these additional aspects of slide movement and hydroplaning.

Chapter 1: Introduction

Submarine landslides present an important risk to offshore structures and related facilities such as pipelines. Although submarine slides have many similarities to their subaerial counterparts, there are important differences. Hance (2002) conducted a comprehensive survey and developed an extensive database of submarine slope failures. He reported that out of 399 slides examined, 334 occurred on slopes flatter than 10 degrees. He also reported that among a total of 434 slides, 194 slides traveled a distance greater than 10 km; three slides traveled more than 500 km. The reasons for slides on such flat slopes having such large travel (“run-out”) distances are only partially understood. One possible explanation for such large run-out distances is that hydroplaning occurs where the slide mass moves on a thin layer of water. The layer of water works as a lubricant between the slide mass and underlying ground and thus reduces the resistance on the base of the slide mass.

Experimental, analytical and numerical studies have been conducted to understand hydroplaning and its effect on submarine landslides. However, currently no tools incorporate the mechanism of hydroplaning and predict the process of a landslide from initiation to cessation of movement. The hydrodynamic forces on the slide mass, and the deformation and movement of a slide mass when hydroplaning occurs are not well understood or explained.

The objective of the research reported on herein is to develop a numerical model for submarine slides, with emphasis on possible hydroplaning. The interaction between a sliding mass and the surrounding fluid is decoupled as two problems: 1) the flow around a sliding mass and 2) the movement of the slide mass under the hydrodynamic stresses applied by the surrounding flow.

The research conducted for this dissertation is presented in seven chapters.

- 1) In chapter 2, previous research on hydroplaning of subaqueous slides is summarized.
- 2) In chapter 3, numerical simulations for the hydrodynamic conditions around a slide mass are discussed. Particular emphasis is given to the stresses applied on the slide mass by the surrounding fluid before and during hydroplaning.
- 3) In chapter 4, a block model for subaqueous slides involving possible hydroplaning is presented. The hydrodynamic stresses obtained from the research discussed in chapter 3 are integrated in the block model as stress boundary conditions.
- 4) In chapter 5, the block model is validated by comparison with the experimental results on subaqueous slides reported by Mohrig, et al (1999).
- 5) In chapter 6, conclusions of the research are summarized

Chapter 2: Background

Hydroplaning happens when a thin layer of fluid (air, water, oil, mud or other) is trapped between two objects moving relative to each other. The thin layer of fluid acts as a lubricant and reduces the friction between the two objects.

Hydroplaning was proposed as a mechanism for submarine landslides by Mohrig, et al. (1998). They suggested hydroplaning as a mechanism to explain why submarine landslides have larger run-out distances than their subaerial counterparts even though the resistance from the surrounding water is greater than that from surrounding air.

In this chapter, the research conducted on hydroplaning in general is summarized first. Experimental, analytical and numerical studies on the hydroplaning of subaqueous slides specifically are then summarized. The limitations of this previous research are also discussed.

2.1 PREVIOUS RESEARCH ON GENERAL HYDROPLANING

The study and application of hydroplaning starts in the late 19th century. The term hydroplane first appeared as a name for racing boats in 1870's. American designer, Clinton Crane, produced one of the earliest large racing hydroplanes according to Ewart, W. D. (1962). Hydroplanes obtained a high speed because of an air-cushion formed between the bottom of the boat and the underlying water reducing the resistance on the bottom of the boat.

Harrin, E. N. (1958) reported the first experimental demonstration for hydroplaning of pneumatic tires. He observed a thin layer of water between the tire surface and the pavement in a tire treadmill test. Further research on hydroplaning of pneumatic tires was conducted by the National Aeronautics and Space Administration in

the 1960's. In 1983, Browne and Whicker (1983) developed a model for tire-fluid interaction during steady-state hydroplaning of a tire.

Heim (1882) first suggested that landslides traveled on a thin layer of air (at the early stage of sliding) or mud (at the later stage of sliding). Shreve (1968a, 1968b) concluded that a relatively thin layer of compressed air acted as a lubricant for the Elm and Frank landslides based on the characteristics of the slides and the reports by eyewitnesses. Moriwaki et al. (1985) conducted simple point-mass modeling for the Ontake-san avalanche and recognized that assuming entrainment of water and fluidization of the sliding avalanche boundary resulted in numerical results closest to field conditions. Finally, Mohrig, et al. (1998) pointed out that submarine landslides with long run-out distances might have involved hydroplaning.

2.2 EXPERIMENTAL STUDY ON HYDROPLANING OF SUBAQUEOUS SLIDES

Laval et al. (1988), Mohrig et al. (1998, 1999) and Marr et al. (2001) have all conducted experimental studies of hydroplaning of subaqueous slides. Details from the experiments are summarized in Tables 2.1 and 2.2. Laval et al. (1988) poured sand suspensions into a channel filled with water. They observed a thin layer of water under the front of the slide mass. Mohrig et al. (1998, 1999) used slurry instead of sand suspensions. They conducted parallel experiments on subaqueous slides and on subaerial slides. Hydroplaning was observed in eight of ten subaqueous slides. The run-out distances of subaqueous slides that hydroplaned were longer than those of subaerial slides. Mohrig et al. also proposed a densimetric Froude number, Fr_d , to characterize the onset condition of hydroplaning. The densimetric Froude number Fr_d is defined as:

$$Fr_d = \frac{U}{\sqrt{\left(\frac{\rho_s}{\rho_w} - 1\right)gH \cos \theta}} \quad (2.1)$$

where U is the average velocity of sliding, ρ_s and ρ_w are the densities of the slurry and water, g is the acceleration due to gravity, H is the average thickness of debris and θ is the slope angle of the channel bottom. The minimum value of the Froude number $Fr_{d,crit}$ for hydroplaning to occur was reported to be 0.3 based on Mohrig, et al's experiments. The minimum sliding velocity U_{crit} for hydroplaning to occur can be calculated as:

$$U_{crit} = Fr_{d,crit} \sqrt{\left(\frac{\rho_s}{\rho_w} - 1\right) g H \cos \theta} \quad (2.2)$$

Marr et al. (2001) also used premixed slurry and reported frequent hydroplaning of the slide masses. They reported that hydroplaning resulted in structureless deposits, tension cracks, compression ridges, water-escape structures and detached slide-blocks.

Table 2.1: Properties of sliding mass used in experimental studies of hydroplaning

Tests	Water content	Bulk density ($\times 10^3 \text{ kg} / \text{m}^3$)	D50 (μm)	Mineralogy	Hydraulic conductivity (m/s)	Yield strength (Pa)	Viscosity (Pa-s)
Laval et al. (1988)	Solution or suspension in saline water	1.04-1.32	45-112.5	Quartz only			
Mohrig et al. (1998)	16.5% of tap water	2.08 (± 0.03)	57	Quartz only	3×10^{-5}	29	14
Mohrig et al. (1999)	39% of tap water	1.6	1-3 for clay 57 for silt and sand	40% kaolin, 40% silt and 20% sand	1×10^{-4}	49, 36 and 33	0.035, 0.023 and 0.019
Marr et al. (2001)	25%, 30% and 40% of tap water	1.56-1.93		Clay, silica sand and coal slag		9.9-50.7	

Table 2.2: Setup of experiments and observations

Tests	Equipment	Initiation	Observations
Laval et al. (1988)	Plexiglass channel (4 m long, 0.35 m deep and 0.2 m wide), slope variance from 1 ° to 7 °	2l, 4l or 8l of Saline-water solutions or sand suspensions were released from the gate of the tank	A thin layer of ambient water was incorporated by gravitational instability under the overhung surge front.
Mohrig et al. (1998)	Channel (10 m long, 3 m high and 0.2 m wide) suspended in water tank with two segments, slope variance from 0° (horizontal) to 20°	Approximately 0.16 m ³ of slurry (debris) was poured at the upper end of the tank in a period of 60 seconds or less.	Debris flow hydroplanes when the densimetric Froude number Fr_d is between 0.3 and 0.4. Necking happens behind the head due to the flow attenuation between the lubricated front and the more bed-attached body. The ratio of the height of head to the height of average debris body increases with Fr_d . The penetration distance of water underneath a hydroplaning debris flow increases with Fr_d and can reach 10 times the average flow depth. The debris underlain by water film ceases to flow internally and moves forward as a block. Hydroplaning also increases the frontal velocity. New head forms after the detachment of the former head.
Mohrig et al. (1999)	Channel (10 m long, 3 m high and 0.2 m wide) suspended in water tank with two segments, slopes are 6° and 1°. Two types of channel bottoms are hard bottom consisting of rough, inerodible rubber matting and soft bottom consisting deposit of an antecedent subaerial flow.	Approximately 30 l of slurry (debris) was released from the head tank through a slot (20 mm high and 170 mm wide).	Hydroplaning causes larger run-out distances on inerodible bed and mutes the role of debris rheology. It also causes head to run out ahead of the body and results in a thickness of deposit well below that associated with the yield strength. Hydroplaning suppress the remobilization of an antecedent debris deposit due to 1) thickness of an antecedent deposit well below that associated with yield strength and 2) overpassing subaqueous debris flow on a film of fluid.
Marr et al. (2001)	Glass-walled flume (10 m long and 0.3 m wide) with three segments, slope variance from 0° (horizontal) to 4.6°	91 kg premixed slurry was released from an aperture (0.3 m wide and 0.03 high)	Hydroplaning was most frequently observed in strongly coherent flows and resulted in structureless deposits, major slope-response changes in thickness, tension cracks, compression ridges, water-escape structures and detached slide-blocks.

2.3 ANALYTICAL SOLUTION ON HYDROPLANING OF SUBAQUEOUS SLIDES

Harbitz et al. (2003) developed a one-dimensional analytical solution for a slide under steady-state hydroplaning based on dynamic lubrication theory. In this section, dynamic lubrication theory is first introduced and Harbitz et al. (2003)'s solution is then discussed.

2.3.1 Dynamic Lubrication Theory

Dynamic lubrication theory addresses the two-dimensional flow between two infinitely long flat plates moving relative to each other as shown in Figure 2.1. The forces applied on an element of fluid by the surrounding fluid are shown in Figure 2.2.

Dynamic lubrication theory involves the following assumptions:

1. The distance between the two plates h is small;
2. The fluid between the plates is a Newtonian liquid;
3. The kinetic pressure in the fluid p is constant in the y direction, i.e. $\frac{\partial p}{\partial y} = 0$;
4. The flow is fully developed along the x direction, i.e. $\frac{\partial u}{\partial x} = \frac{\partial v}{\partial x} = 0$, where u and v are the flow velocities in the x and y directions respectively;
5. The flow is steady, i.e. $\frac{\partial u}{\partial t} = \frac{\partial v}{\partial t} = \frac{\partial p}{\partial t} = \frac{\partial \tau}{\partial t} = 0$, where t is time and τ is the

viscous shear in the fluid.

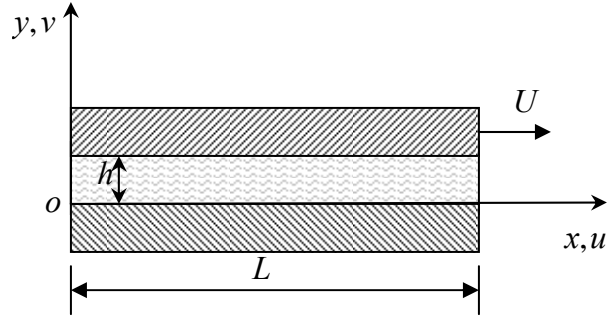


Fig. 2.1 2-D flow between plates

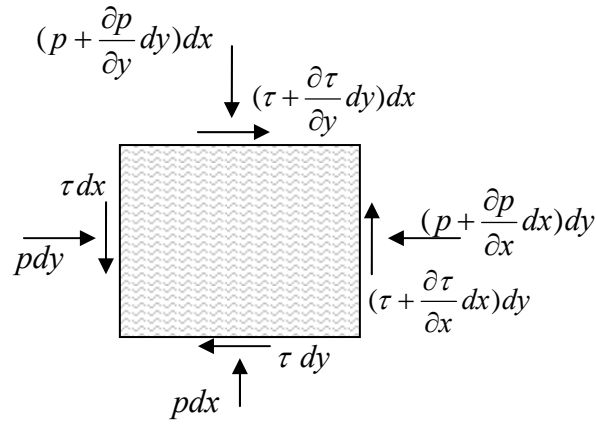


Fig. 2.2 Stresses on an element of fluid

In order to determine the velocities u and v , the continuity equation of flow between the plates and the equilibrium conditions for an element of fluid are considered.

The continuity equation for 2-D flow is

$$\frac{\partial u}{\partial x} + \frac{\partial v}{\partial y} = 0 \quad (2.3)$$

According to Assumption 4 above, the first term of Equation 2.3 is zero, i.e.

$$\frac{\partial u}{\partial x} = 0 \quad (2.4)$$

Substituting Equation 2.4 into Equation 2.3 yields:

$$\frac{\partial v}{\partial y} = 0 \quad (2.5)$$

Integrating Equation 2.5 with respect to y gives:

$$v = c(x, t) \quad (2.6)$$

Where $c(x, t)$ is a function of x and t . According to Assumptions 4 and 5 above, the partial derivatives of velocity v with respect to x and t are zero, i.e.:

$$\frac{\partial v}{\partial x} = \frac{\partial v}{\partial t} = 0 \quad (2.7)$$

Substituting Equation 2.6 into Equation 2.7 gives:

$$\frac{\partial c(x, t)}{\partial x} = \frac{\partial c(x, t)}{\partial t} = 0 \quad (2.8)$$

Equation 2.8 requires that:

$$c(x, t) = \text{constant} \quad (2.9)$$

Combing Equation 2.9 with 2.6 gives:

$$v = \text{constant} \quad (2.10)$$

The boundary conditions for velocity v are:

$$\begin{cases} v = 0 & \text{at } y = 0 \\ v = 0 & \text{at } y = h \end{cases} \quad (2.11)$$

Equations 2.11 and 2.10 yield:

$$v = \text{constant} = 0 \quad (2.12)$$

Equation 2.10 shows that the velocity v is always zero.

According to Assumptions 3 and 5 above, the partial derivatives of kinetic pressure p with respect to y and t are zero, i.e.:

$$\frac{\partial p}{\partial y} = \frac{\partial p}{\partial t} = 0 \quad (2.13)$$

Equation 2.13 then suggests:

$$p = f(x) \quad (2.14)$$

Where $f(x)$ is a function of x only, i.e., kinetic pressure p only varies with x . The partial derivative of kinetic pressure p with respect to x is the same as the derivative of p with respect to x , i.e.:

$$\frac{\partial p}{\partial x} = \frac{dp}{dx} \quad (2.15)$$

Equilibrium of forces on the element in the x direction gives:

$$p dy - \tau dx - \left(p + \frac{\partial p}{\partial x} dx \right) dy + \left(\tau + \frac{\partial \tau}{\partial y} dy \right) dx = 0 \quad (2.16)$$

or
$$\frac{\partial p}{\partial x} - \frac{\partial \tau}{\partial y} = 0$$

Substituting Equation 2.15 into 2.16 yields:

$$\frac{dp}{dx} - \frac{\partial \tau}{\partial y} = 0 \quad (2.17)$$

The relationship between shear stress τ and the rate of shear strain $\frac{\partial u}{\partial y}$ for a Newtonian

fluid can be expressed as

$$\tau = \mu \frac{\partial u}{\partial y} \quad (2.18)$$

where μ is the dynamic viscosity of the fluid. Substituting (2.18) into (2.17) then gives

$$\frac{dp}{dx} - \mu \frac{\partial^2 u}{\partial y^2} = 0 \quad \text{or} \quad \frac{\partial^2 u}{\partial y^2} = \frac{1}{\mu} \frac{dp}{dx} \quad (2.19)$$

Integrating Equation 2.19 with respect to y yields:

$$u = \frac{1}{\mu} \left[\frac{1}{2} \frac{dp}{dx} y^2 + c_1(x)y + c_2(x) \right] \quad (2.20)$$

Where $c_1(x)$ and $c_2(x)$ are functions of x governed by the boundary conditions for velocity, u . The boundary conditions for velocity, u , are as follows:

$$\begin{cases} u = 0 & \text{at } y = 0 \\ u = U & \text{at } y = h \end{cases} \quad (2.21)$$

Where U is the velocity of the upper plate relative to the lower plate as shown in Figure

2.1. From Equations 2.20 and 2.21 we can write:

$$\begin{cases} c_1(x) = \frac{\mu U}{h} - \frac{1}{2} \frac{dp}{dx} h \\ c_2(x) = 0 \end{cases} \quad (2.22)$$

Substituting Equation 2.22 into Equation 2.20 yields:

$$u = \frac{1}{2\mu} \left[\frac{dp}{dx} (y^2 - hy) \right] + \frac{U}{h} y \quad (2.23)$$

Equation 2.23 shows that the velocity u varies quadratically in the y direction.

In summary, according to dynamic lubrication theory, the velocities u and v of the fluid have the following characteristics:

1. The velocity u can be expressed as a quadratic function y ;
2. The velocity v is zero.

The above characteristics of velocities u and v are applied in Harbitz et al.'s solution.

2.3.2 Harbitz et al.'s Solution

Harbitz et al. (2003) solved the problem of steady-state hydroplaning of a slide mass analytically. They assumed that the slide mass is a rigid block sliding along a film of water as shown in Figure 2.3. The length-to-height ratio (L/H) of the block is assumed to be so large that the forces on the leading and trailing edges of the block are negligible. The coordinate system moves with the lower left corner of the block in the x direction as shown in Figure 2.3. The interface between the block and the underlying

slope is assumed to be smooth and the slope angle is constant. The distance between the bottom of the block and the underlying ground h is assumed to vary linearly along the x direction. The distances between the two lower corners of the block and underlying ground are designated as h_f and h_t , respectively. Harbitz et al. applied the conditions from dynamic lubrication theory to the flow between the block and underlying ground. They assumed that the flow velocity in the x direction u is distributed quadratically in the y direction.

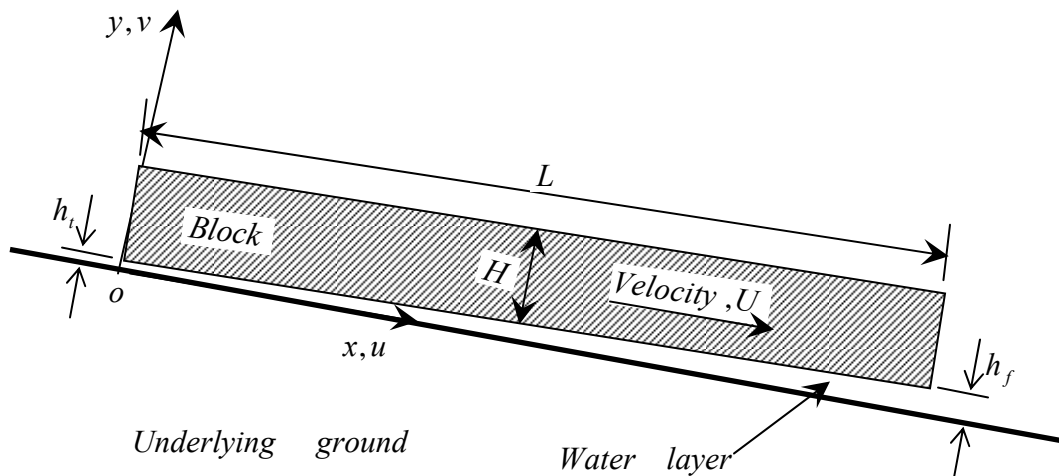


Fig. 2.3 Steady-state hydroplaning of a sliding block on a slope

In Figure 2.4, the symbol Q represents the total flow rate for flow in the x direction between the block and underlying ground. Harbitz et al. (2003) derived an expression for flow rate Q in terms of the length of the block L , distances h_f, h_t and the velocity of the block U . Harbitz et al. assumed that only five types of stresses and forces are applied on the block. These stresses and force are applied by the water and underlying ground as illustrated in Figure 2.5. Hydrostatic pressures are accounted for by using the submerged weight of the block G' . The kinetic pressure p_b and the viscous shear τ_b along the bottom of the block are functions of the flow rate Q , distances h_f, h_t and the velocity of the block U . The kinetic pressure on the top surface of the block p_t

is assumed to be zero. The viscous shear on the top surface of the block τ_t is estimated using the theory for laminar or turbulent flow over a flat plate.

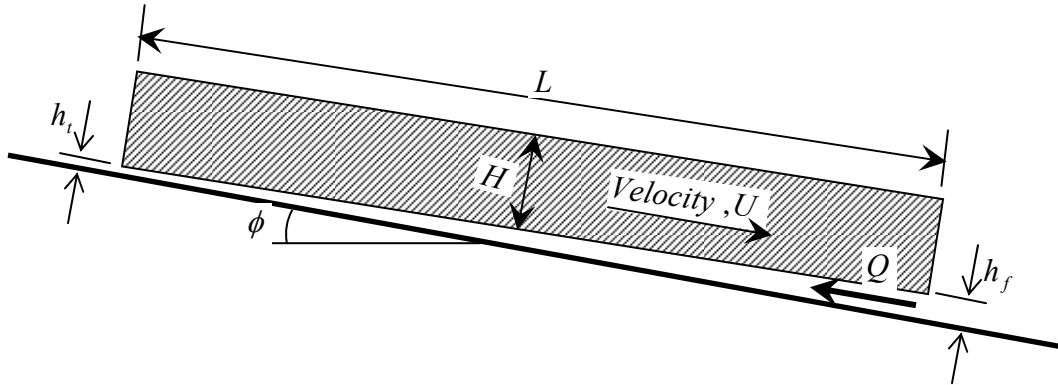


Fig. 2.4 Major variables for Harbitz et al.'s solution

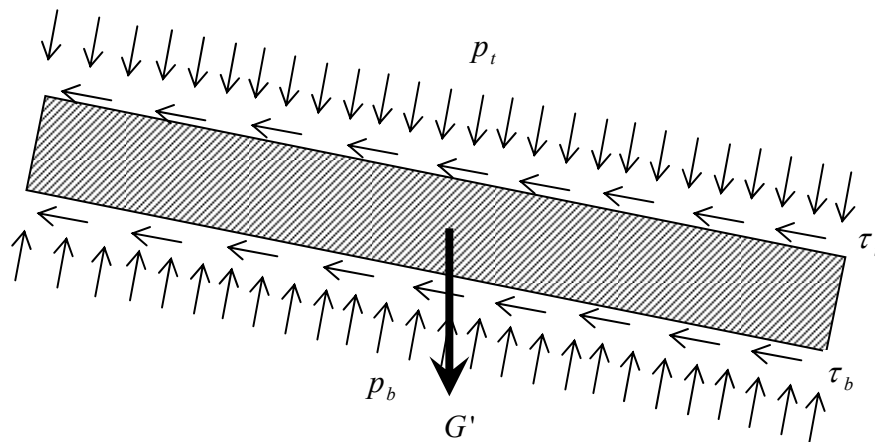


Fig. 2.5 Forces and moments on the hydroplaning block

Equilibrium of the block requires that the total forces and total moments sum to be zero. Equilibrium for the three degrees of freedom and the equation for the flow rate Q provide four simultaneous nonlinear equations as follows:

$$f_1(H, L, U, Q) = 0 \tag{2.24}$$

$$f_2(H, L, U, Q) = 0 \tag{2.25}$$

$$f_3(H, L, U, Q) = 0 \tag{2.26}$$

$$f_4(H, L, U, Q) = 0 \tag{2.27}$$

Here f_1 , f_2 , f_3 and f_4 are non-linear functions of L , H , U and Q . More details of functions can be found in Harbitz et al. (2003). The four equations above constitute Harbitz et al.'s analytical solution; however the actual scheme for solving the four equations together for the block length L , block height H , velocity U and flow rate Q was never provided by Harbitz et al.

2.4 NUMERICAL MODELS ON POST-INITIATION MOVEMENT OF SUBAQUEOUS SLIDES

De Blasio, et al. (2004) presented a one-dimensional numerical model for subaqueous slides that includes possible hydroplaning. Their model is essentially an extension of a viscous model for non-hydroplaning debris flows by Imran et al. (2001). Below Imran et al.'s model and other models that do not include hydroplaning are discussed first. De Blasio, et al.'s model is then discussed.

2.4.1 Numerical Models involving No Hydroplaning

A common assumption for the models that do not involve hydroplaning is that the bottom surface of the slide mass is always in contact with the underlying ground. The detachment of the slide mass from the underlying ground or hydroplaning can not occur. Several major models that do not involve hydroplaning are summarized below.

2.4.1.1 Lumped mass models

Several lumped mass models idealize the slide mass as a single point and only provide estimations for the movement of the center of the slide mass down slope (Körner 1976; Perla et al., 1980; Hutchinson, 1986 and others). No movement of the slide mass normal to the underlying ground is considered.

2.4.1.2 Miao, et al.'s model

Miao, et al. (2001) modeled the slide mass as a set of deformable blocks. They incorporated mass dynamics into the limit equilibrium analysis of blocks considering interaction and deformation of the blocks. All the blocks are assumed to be in contact with the underlying ground along the bottom surfaces.

2.4.1.3 Continuum models

Tacher, L. et al. (2005) modeled the slide mass as a continuous solid. They applied a Mohr-Coulomb model and the Hujeux elasto-plastic model in a finite element simulation of landslides. Along the interface between the slide mass and underlying ground, the displacements of the slide mass normal to the underlying ground were assumed to be zero.

2.4.1.4 Fluid models

Blight, et al. (2005), Fread (1984), Imran et al. (2001) and others modeled landslides as a viscous fluid. Imran et al. (2001)'s model is a representative example of these viscous flow models and is discussed in detail below.

In Imran et al.'s model, the deformation and movement of the slide mass are simulated as an unsteady, non-uniform, laminar slender flow as illustrated in Figure 2.6. Any flow in the z direction is neglected and all flow conditions in the z direction are assumed to be constant. The moving mass is assumed to remain continuous. The effect of static pressures applied on the slide mass by the surrounding fluid is accounted for by using the effective weight of the slide mass. Hydrodynamic stresses applied on the slide

mass by the surrounding fluid are neglected. Imran et al. divided the slide mass into a shear layer and plug layer. In the plug layer, the velocity u is assumed to be constant along the y direction. Therefore the shear strain in the plug layer is zero. The shear layer is the transition between the underlying slope and the plug layer and shear strain occurs.

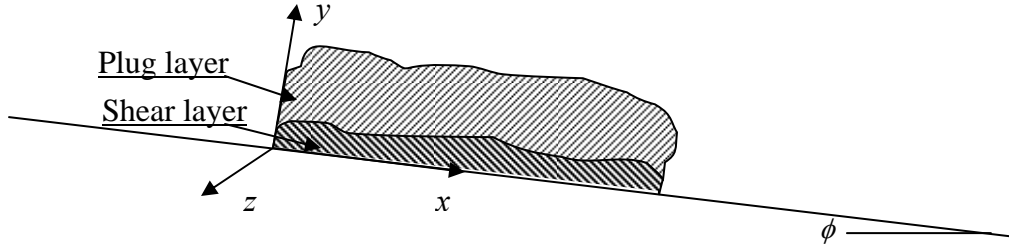


Fig. 2.6 Imran et al.'s model of slides

The continuity and equilibrium equations in a coordinate system fixed on the slope as in Figure 2.6 are as follows.

$$\frac{\partial u}{\partial x} + \frac{\partial v}{\partial y} = 0 \quad (2.28)$$

$$\frac{\partial u}{\partial t} + u \frac{\partial u}{\partial x} + v \frac{\partial u}{\partial y} = - \left(1 - \frac{\rho_w}{\rho_s} \right) g \frac{\partial H}{\partial x} + \left(1 - \frac{\rho_w}{\rho_s} \right) g \sin \theta + \frac{1}{\rho_s} \frac{\partial \tau}{\partial y} \quad (2.29)$$

$$p' = (\rho_s - \rho_w) g (H - y) \quad (2.30)$$

where u and v are the velocities in the x and y directions, t is time, ρ_w and ρ_s are the densities of the ambient fluid and slide mass, respectively, g is the acceleration due to gravity, H is the height of the slide mass, τ is the shear stress and p' is the pressure due to the effective weight of the slide mass. Imran et al. used the Herschel-Bulkley rheological model to describe the relationship between the rate of shear strain $\dot{\gamma}$ and the shear stress τ . The rate of shear strain $\dot{\gamma}$ can be expressed in term of shear stress τ as:

$$\frac{\dot{\gamma}}{\dot{\gamma}_r} = \begin{cases} 0 & \text{at } \tau \leq \tau_{yield} \\ \left(\frac{\tau}{\tau_{yield}} - 1 \right)^{1/n} & \text{at } \tau > \tau_{yield} \end{cases} \quad (2.31)$$

where τ_{yield} is a yield stress and $\dot{\gamma}_r$ is a reference rate of shear strain. This model reduces to a Bingham model when n is 1.0.

Imran et al. applied the following boundary conditions on the slide mass:

1. There is no slip at the interface between the slide mass and underlying ground, i.e.

$$\begin{cases} u = 0 & \text{at } y = 0 \\ v = 0 & \text{at } y = 0 \end{cases} \quad (2.32)$$

2. The top surface of the slide mass is a kinematic boundary, i.e.

$$v = \frac{\partial H}{\partial t} + u \frac{\partial H}{\partial x} \quad \text{at } y = H \quad (2.33)$$

For initial conditions, the slide mass is assumed to be stationary and not moving. The initial shape and dimensions of the slide mass are specified. The sliding process is assumed to stop when the maximum of velocity u within the slide mass is less than 10 cm/s.

Imran et al. solved Equations 2.28 to 2.30 numerically using an explicit finite difference scheme. They simulated numerically the laboratory experiments on subaerial and subaqueous slides conducted by Mohrig, et al. (1998). The numerical results from the simulations on subaerial slides agreed well with the measurements reported by Mohrig, et al. However the run-out distances of subaqueous slides predicted by Imran et al.'s model were much shorter than those reported by Mohrig, et al.

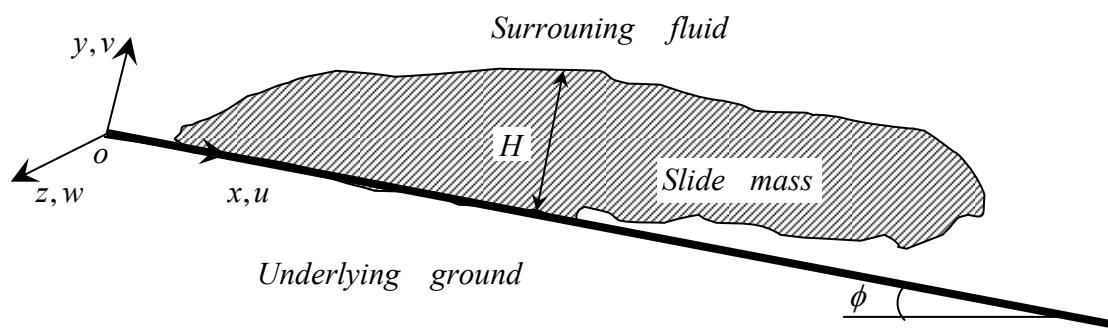
2.4.1.5 Disadvantage of models involving no hydroplaning

None of the numerical models discussed in section 2.4.1 include hydroplaning. In these models, the driving forces on subaqueous slides are considered smaller than those

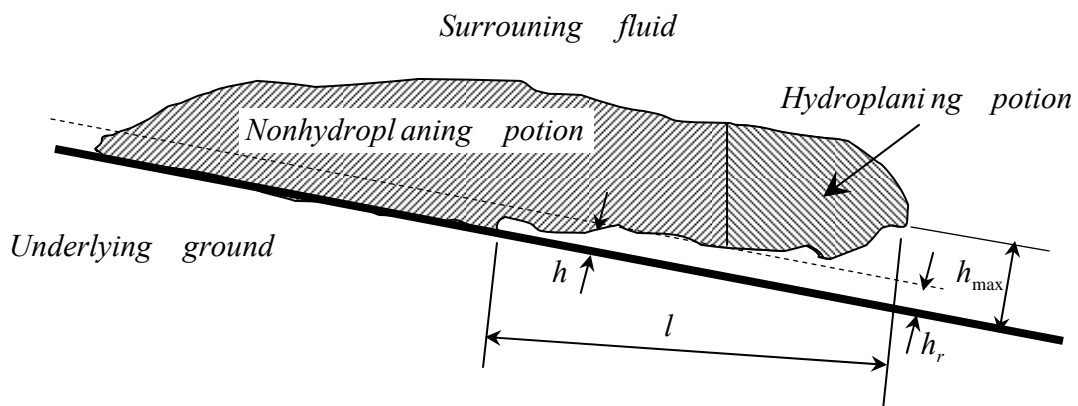
on the subaerial counterparts due to buoyancy. Therefore the predictions of run-out distances for subaqueous slides are smaller than those for their subaerial counterparts. These predictions are inconsistent with the observations by Mohrig, et al. (1998, 1999) discussed earlier.

2.4.2 De Blasio, et al.'s Model

De Blasio, et al. (2004) presented a one-dimensional numerical model for slides that includes possible hydroplaning. They modified Imran et al.'s model by considering the possible detachment of the slide mass from the underlying ground. The geometry and coordinate system of the model are shown in Figure 2.7.



(a) Coordinate system and geometry of the slide mass



(b) Geometry of the wedge between the slide mass and underlying ground

Fig. 2.7 Geometry and coordinate system for De Blasio, et al.'s model

In De Blasio et al.'s model, the slide mass is assumed to be a viscous fluid and the sliding process is divided into four stages. The four stages of sliding are as follows: (1) the slide mass flows directly on the surface of the underlying ground, (2) a wedge of water forms at the interface between the slide mass and underlying ground, but the wedge is not thick enough for the slide mass to hydroplane, (3) the slide mass hydroplanes and (4) hydroplaning stops and the slide mass decelerates. For stages (1), (2) and (4), the viscous shear on the top surface is assumed to be the only hydrodynamic stress applied on the slide mass. This viscous shear is estimated using the coefficient of viscous drag derived for cylinders by Newman (1977). Along the bottom surface of the slide mass, shear stress is assumed to be applied by the underlying ground. For the first stage, the shear stress on the bottom surface of the slide mass is related to the yield stress of the sliding mass. The second stage starts when the velocity of the slide mass reaches a “critical” value. The critical velocity U_{crit} is determined using Equation (2.2) and the critical Froude number $Fr_{d,crit}$ is assumed to be 1.0. For the second stage, a wedge of water is introduced suddenly at the interface between the slide mass and the underlying ground near the front of the slide mass. As shown in Figure 2.7 (b), the thickness of the wedge h is a function of the coordinate x . Initial values of thickness h and length l of the wedge are assumed arbitrarily. Within the wedge, the kinetic pressure p is assumed to vary linearly along the x direction. The velocity u of water within the wedge is assumed to vary quadratically in the y direction as discussed earlier in section 2.3.1. The flow of water within the wedge is solved for together with the flow of the sliding material. The changes of the wedge's dimension (h and l) are also computed. The shear stress on the bottom surface of the slide mass is assumed to be applied by the underlying ground despite the existence of the wedge. Any influence on this shear stress produced by the wedge of water is neglected. The third stage starts when the maximum value of thickness h_{max} is greater than the height of roughness h_r at the interface between the slide mass and the underlying slope. The height of the roughness h_r is assumed to be

several millimeters for laboratory tests and several decimeters for cases in the field. In the third stage, the portion of slide mass under which the thickness h is greater than height h_r is assumed to hydroplane. The shear stress on the bottom of the hydroplaning portion of the slide mass is assumed to be the viscous shear at the top surface of the water wedge. A drag due to kinetic pressure p applied by the surrounding fluid is added on the slide mass. This drag is estimated using the coefficient of pressure-induced drag derived for cylinders by Newman (1977). The fourth stage of sliding is assumed to start when the maximum thickness h_{\max} is smaller than the height of roughness h_r . The fourth stage is similar to the second stage and the slide mass decelerates until it stops.

2.5 EXAMINATION OF PREVIOUS RESEARCH ON HYDROPLANING OF SLIDES

In this section, the previous experimental, analytical and numerical research on hydroplaning of subaqueous slides are examined and limitations are discussed.

2.5.1 Examination of Harbitz et al.'s solution

A numerical method is used to solve Equations 2.24 to 2.27 in Harbitz et al.'s solution for the block length L , block height H , velocity U and flow rate Q . The numerical method and results are discussed further below.

2.5.1.1 Numerical method

For this research, a Newtonian iterative procedure was used to solve Harbitz et al.'s Equations 2.24 to 2.27. A computer program `nopressure.cpp` was written in the C programming language to implement the procedure. Details of the program and Newtonian procedure are discussed below.

The program `nopressure.cpp` reads from a file named `gld.in`. The parameters specified as input data and their physical meanings are summarized in Table 2.3. The program writes the numerical results summarized in Table 2.4 to a file named `gld.out`.

Table 2.3 Input parameters and their physical meanings

Parameter	Physical Meaning
L	The initial value for the length of the block (m)
H	The initial value for the height of the block (m)
U	The initial value for the velocity of the block (m/s)
Q	The initial value for the flow rate (m^2 / s)
ϕ	Slope angle of the underlying ground (degree)
k	The ratio of the distance between the lower corner of the block and underlying ground at the tail h_t to the length of the block L , i.e. $k = \frac{h_t}{L}$
r	The ratio of the distance between the lower corner of the block and underlying ground at the front h_f to that at the tail h_t , i.e. $r = \frac{h_f}{h_t}$
ν_w	The kinematic viscosity of pure water (m^2 / s)
R_s	The effective specific gravity of the sliding block, i.e. $R_s = \frac{\rho_s - \rho_w}{\rho_w}$, where ρ_s is the density of the block, and ρ_w is the density of the surrounding fluid.
s	The ratio of the viscosity of the fluid between the block and underlying ground to that of pure water, i.e. $s = \frac{\nu}{\nu_w}$, where ν is the viscosity of the fluid between the block and underlying ground.

Table 2.4 Output variables and their physical meanings

Parameter	Physical Meaning
L	Calculated value for the length of the block (m)
H	Calculated value for the height of the block (m)
U	Calculated value for the velocity of the block (m/s)
Q	Calculated value for the flow rate (m^2 / s)
$error$	The numerical error in the last iteration

A flow chart for the computer program is shown in Figure 2.8. In the Newtonian iterative procedure, a matrix A is defined as:

$$A_{i,1} = \frac{f_i(L + dL) - f_i(L - dL)}{2dL} \quad \text{for } i = 1 \text{ to } 4 \quad (2.34)$$

$$A_{i,2} = \frac{f_i(H + dH) - f_i(H - dH)}{2dH} \quad \text{for } i = 1 \text{ to } 4 \quad (2.35)$$

$$A_{i,3} = \frac{f_i(U + dU) - f_i(U - dU)}{2dU} \quad \text{for } i = 1 \text{ to } 4 \quad (2.36)$$

$$A_{i,4} = \frac{f_i(Q + dQ) - f_i(Q - dQ)}{2dQ} \quad \text{for } i = 1 \text{ to } 4 \quad (2.37)$$

Where $A_{i,1}$ to $A_{i,4}$ are the four terms at the i th row of matrix A . More details on the Newtonian procedure can be found in Ansorge, et al. (1982). The numerical error for the $(i + 1)$ th iteration is defined as:

$$error_{i+1} = \max \left(\left| \frac{L_{i+1} - L_i}{L_i} \right|, \left| \frac{H_{i+1} - H_i}{H_i} \right|, \left| \frac{U_{i+1} - U_i}{U_i} \right|, \left| \frac{Q_{i+1} - Q_i}{Q_i} \right| \right) \quad (2.38)$$

Where L_i , H_i , U_i and Q_i are the variables calculated in the i th iteration and L_{i+1} , H_{i+1} , U_{i+1} and Q_{i+1} are the variables calculated in the $(i + 1)$ th iteration.

2.5.1.2 Numerical results

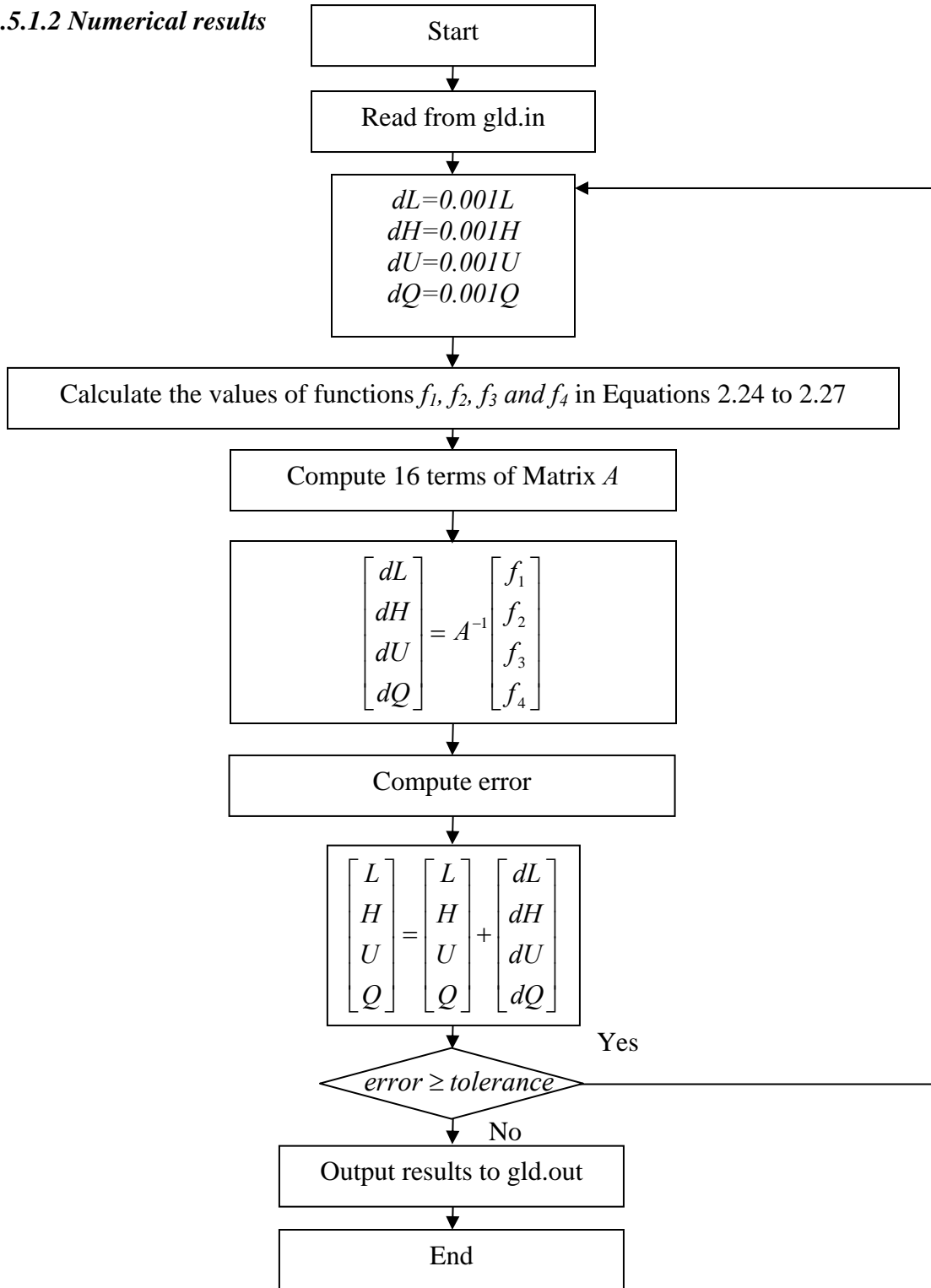


Fig. 2.8 Flow chart of program nopressure.cpp

A total of 22 cases were analyzed using the computer program where the slope angle of the underlying ground ϕ changes from 0.01 to 10 degrees. The input conditions for the numerical cases are listed in Table 2.5. The tolerance of the numerical error defined is 10^{-3} . Calculated values for the unknowns (L, H, U and Q) are plotted versus the slope angle of the underlying ground ϕ in Figures 2.9 to 2.12. Considerable scattering was observed in the computed values, possibly as a result of the error tolerance being too large. However attempts to reduce the apparent scattering by reducing the error tolerance were generally unsuccessful and the iterations were eventually terminated before convergence was achieved.

Table 2.5 Input conditions for numerical cases

Case No.	ν_w (m^2/s)	r	k	ϕ (degree)	R_s	s
1	1.00E-06	4	5.00E-05	0.01	0.8	1.0
2	1.00E-06	4	5.00E-05	0.03	0.8	1.0
3	1.00E-06	4	5.00E-05	0.07	0.8	1.0
4	1.00E-06	4	5.00E-05	0.10	0.8	1.0
5	1.00E-06	4	5.00E-05	0.20	0.8	1.0
6	1.00E-06	4	5.00E-05	0.30	0.8	1.0
7	1.00E-06	4	5.00E-05	0.40	0.8	1.0
8	1.00E-06	4	5.00E-05	0.50	0.8	1.0
9	1.00E-06	4	5.00E-05	0.60	0.8	1.0
10	1.00E-06	4	5.00E-05	0.70	0.8	1.0
11	1.00E-06	4	5.00E-05	0.80	0.8	1.0
12	1.00E-06	4	5.00E-05	0.90	0.8	1.0
13	1.00E-06	4	5.00E-05	1.00	0.8	1.0
14	1.00E-06	4	5.00E-05	2.00	0.8	1.0
15	1.00E-06	4	5.00E-05	3.00	0.8	1.0
16	1.00E-06	4	5.00E-05	4.00	0.8	1.0
17	1.00E-06	4	5.00E-05	5.00	0.8	1.0
18	1.00E-06	4	5.00E-05	6.00	0.8	1.0
19	1.00E-06	4	5.00E-05	7.00	0.8	1.0
20	1.00E-06	4	5.00E-05	8.00	0.8	1.0
21	1.00E-06	4	5.00E-05	9.00	0.8	1.0
22	1.00E-06	4	5.00E-05	10.00	0.8	1.0

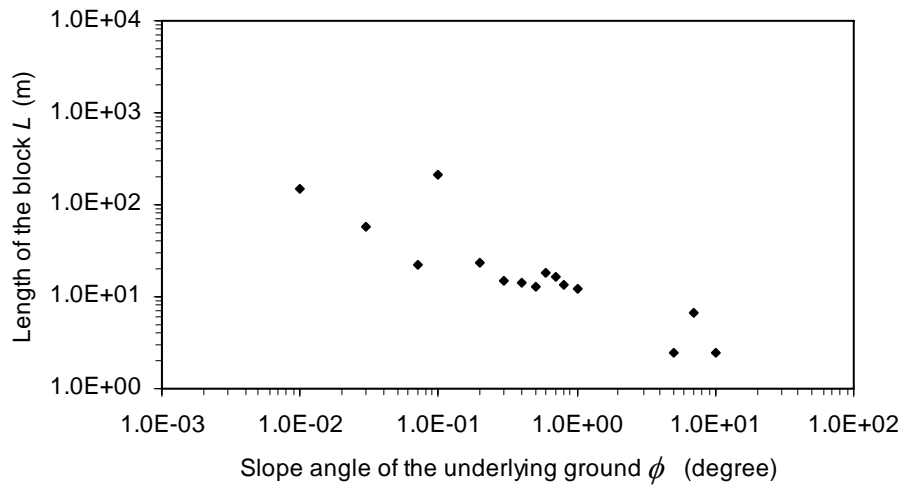


Fig. 2.9 Calculated length of the block using Harbitz et al.'s solution

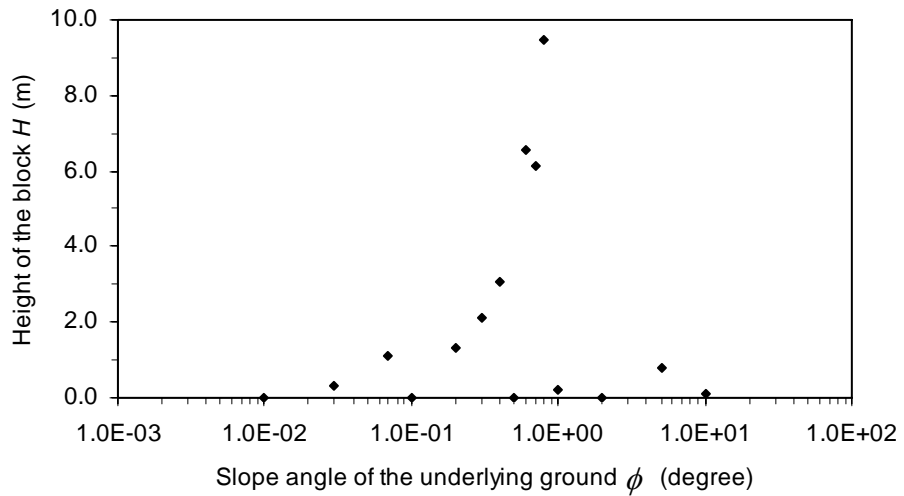


Fig. 2.10 Calculated height of the block using Harbitz et al.'s solution

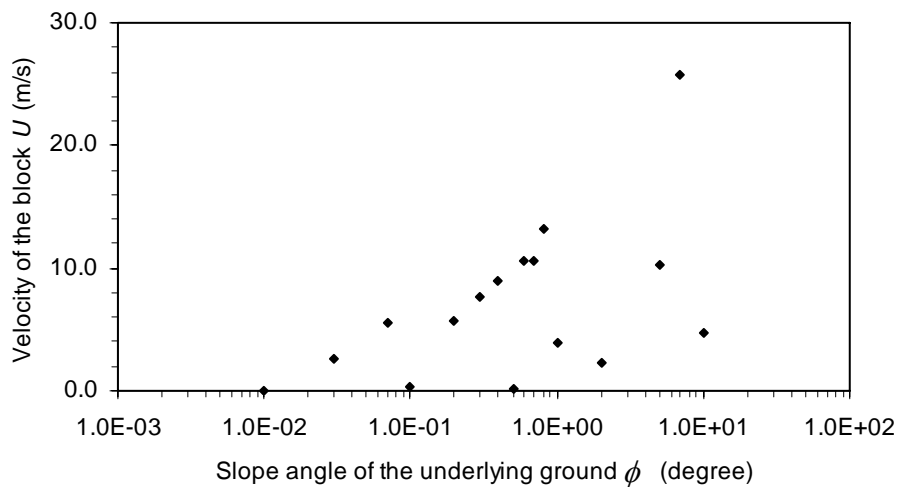


Fig. 2.11 Calculated velocity of the block using Harbitz et al.'s solution

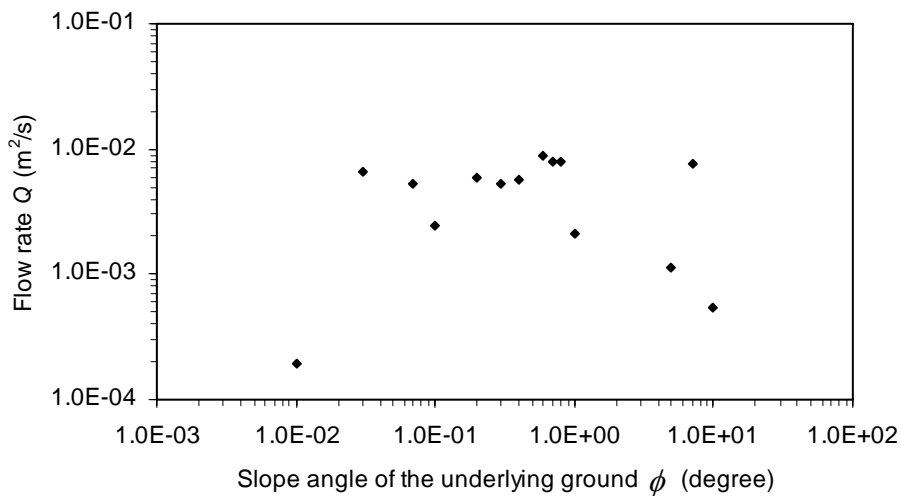


Fig. 2.12 Calculated flow rate between the bottom surface of block and underlying ground using Harbitz et al.'s solution

2.5.1.3 MODIFICATION OF HARBITZ ET AL.'S SOLUTION

In an attempt in this study to reduce the problems of numerical stability in Harbitz et al.'s solution, the solution was modified. A force R_{add} was added to the block in the negative x direction. The force R_{add} was assumed to be produced by a kinetic pressure p_u on the leading edge of the block. The pressure p_u was assumed to be uniform and equal to the stagnation pressure, p_{stag} , calculated as:

$$p_{stag} = \frac{1}{2} \rho_w U^2 \quad (2.39)$$

Using the same input conditions as in Table 2.5, the numerical results from the modified solution are shown in Figures 2.13 to 2.16 along with those from the original solution. In all cases stable numerical results were obtained with the modified solution. The component of the effective weight of the block G' in the x direction is the total driving force applied on the block down slope. This total driving force is equal to the total resistance R on the block because the block is assumed to be in a steady state of motion. Therefore the total resistance R can be calculated as:

$$R = G' \sin \phi \quad (2.40)$$

The ratios of the added force R_{add} to the total resistance R and the slope angles ϕ for all the computed cases are plotted in Figure 2.17. The ratios of the length to the height of the block L/H are also plotted versus the slope angle ϕ in Figure 2.18. As shown in Figures 2.17 and 2.18, when the slope becomes steeper, the effect of the added force R_{add} becomes more significant and the length-to-height ratio (L/H) of the block decreases. Therefore Harbitz, et al.'s assumption that the kinetic pressure p_u along the leading edge of the block was negligible is not reasonable when the slope becomes steep. This unreasonable assumption was the cause of numerical instability in Harbitz et al.'s solution.

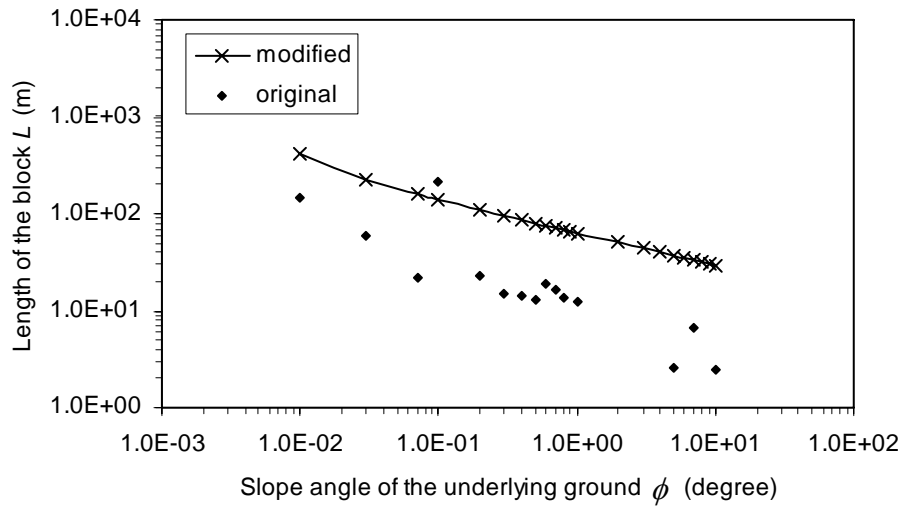


Fig. 2.13 Calculated length of the block using Harbitz et al.'s original solution and modified solution

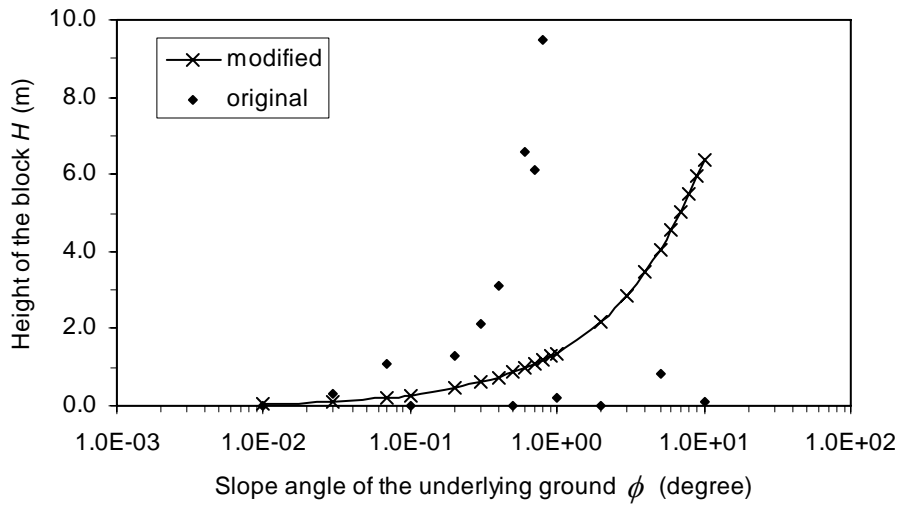


Fig. 2.14 Calculated height of the block using Harbitz et al.'s original solution and modified solution

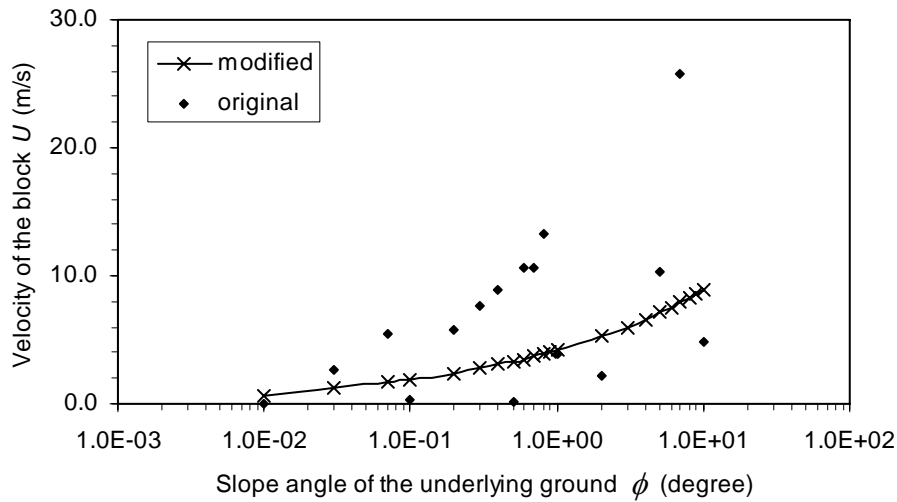


Fig. 2.15 Calculated velocity of the block using Harbitz et al.'s original solution and modified solution

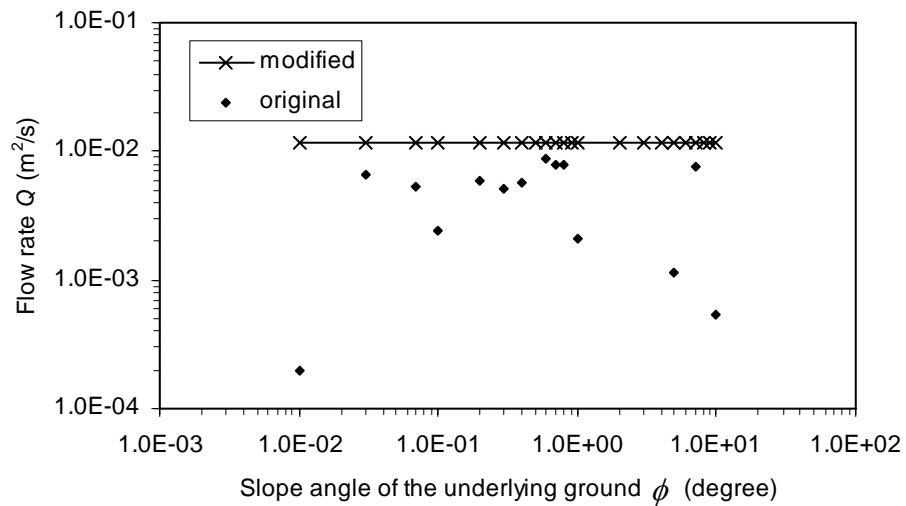


Fig. 2.16 Calculated flow rate between the bottom surface of block and underlying ground using Harbitz et al.'s original solution and modified solution

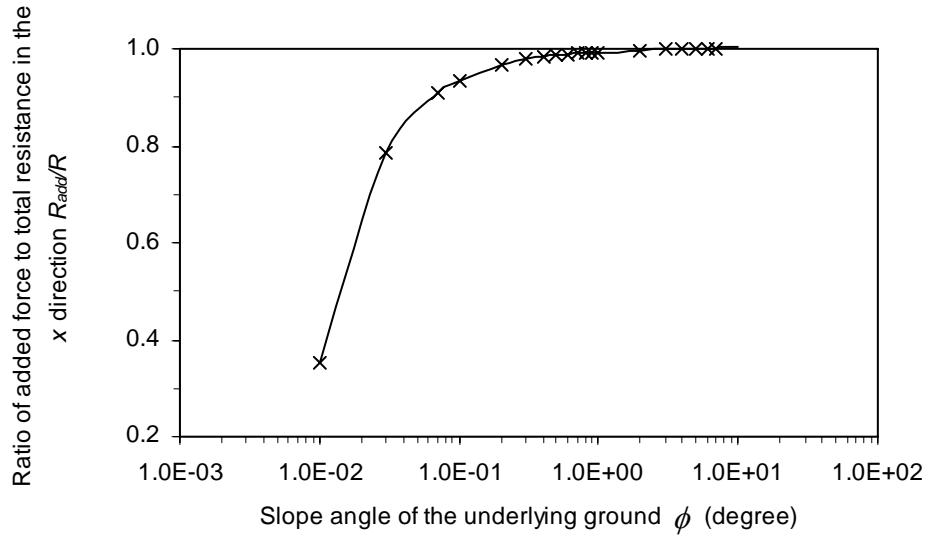


Fig. 2.17 Variation of the ratios R_{add} / R with slope angle ϕ

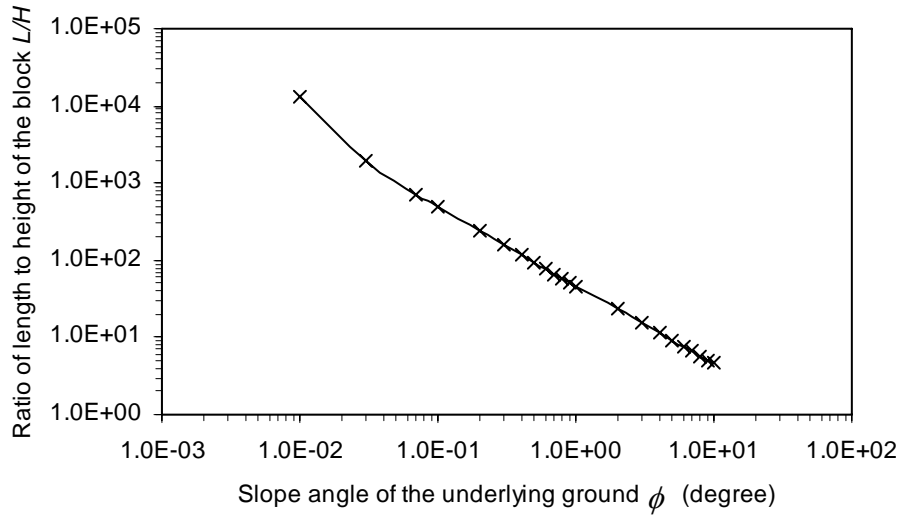


Fig. 2.18 Variation of the ratios L/H with slope angle ϕ

2.5.1.4 Limitations of Harbitz et al.'s solution

Without the modifications described in the previous section, the solution by Harbitz et al. is numerically unstable. The deficiency of Harbitz et al.'s solution is apparently caused by neglecting the kinetic pressure p_u along the leading edge of the block. The effect of the pressure p_u can be significant as the ratio of length to height L/H decreases and the slope angle ϕ increases. Therefore the assumption that the pressure, p_u , along the leading edge of the block is negligible is not valid especially as the slope angle ϕ increases.

2.5.2 Examination of on-set condition for hydroplaning

De Blasio et al. (2004) assumed that the critical value of Froude number $Fr_{d,crit}$ is 1.0 for the slide mass to start hydroplaning. In contrast, Mohrig et al. (1998) reported that the minimum value of the Froude number Fr_d was 0.3 for slide mass to hydroplane. The difference between De Blasio et al.'s assumption and Mohrig et al.'s experimental observations suggests that further study of the physical meaning of Froude number Fr_d is appropriate. Rearrangement of Equation 2.1 gives

$$\frac{1}{2} Fr_d^2 = \frac{\frac{1}{2} \rho_w U^2}{(\rho_d - \rho_w) g H \cos \theta} \quad (2.41)$$

Or in terms of the stagnation pressure given by Equation 2.38

$$\frac{1}{2} Fr_d^2 = \frac{P_{stag}}{(\rho_d - \rho_w) g H \cos \theta} \quad (2.42)$$

The normal stress on the bottom surface σ_w caused by the effective weight of the slide mass can be calculated as

$$\sigma_w = (\rho_s - \rho_w) g H \cos \phi \quad (2.43)$$

Substitute Equation 2.43 into 2.42 gives:

$$\frac{1}{2} Fr_d^2 = \frac{P_{stag}}{\sigma_w} \quad (2.44)$$

Rearrangement of Equation 2.44 gives:

$$Fr_d = \sqrt{\frac{2P_{stag}}{\sigma_w}} \quad (2.45)$$

Thus Froude number Fr_d represents the magnitude of the stagnation pressure p_{stag} relative to the normal stress σ_w and suggests the on-set condition of hydroplaning is related to the stresses and forces applied on the side mass by the surrounding fluid and underlying ground.

In Harbitz et al.'s solution and De Blasio et al.'s model, it was assumed that the kinetic pressure, p_b , along the bottom surface of the slide mass was the only stress applied by the surrounding fluid in the direction normal to the underlying slope. Based on their assumption, hydroplaning should occur when the stagnation pressure p_{stag} is equal to the normal stress σ_w and the total force on the slide mass in the direction normal to the underlying slope is zero. In this case, the theoretical critical Froude number for hydroplaning to happen $Fr_{d,crit}$ should be $\sqrt{2}$ according to Equation 2.45. However values of the critical Froude number $Fr_{d,crit}$ was 1.0 and 0.3 according to De Blasio et al. and Mohrig et al, respectively. The difference among De Blasio et al.'s assumption, Mohrig et al.'s experimental observations and the theoretical value of the critical Froude number $Fr_{d,crit}$ suggests further study is needed for the stresses on the slide mass applied by the surrounding fluid in order to understand hydroplaning of subaqueous slides.

2.6 FUTURE RESEARCH ON HYDROPLANING OF SUBAQUEOUS SLIDES

The limitations of existing models for subaqueous slides involving hydroplaning require further study on the mechanism of hydroplaning and its effect on a slide. In order to better understand hydroplaning, the stresses and forces on the slide mass applied by the surrounding fluid were studied by numerical modeling as described in the next chapter.

Chapter 3: Study of Hydrodynamic Stresses

In order to better understand the motion of subaqueous slides and the occurrence of hydroplaning, the stresses applied on the slide by the surrounding fluid need to be further studied. In this chapter, the flow around a sliding mass and the hydrodynamic stresses applied on the mass by the surrounding fluid are analyzed numerically. Commercial software known as, Fluent 6.1, is used for the numerical modeling. The numerical model, its implementation, results of numerical analyses and conclusions are presented in this chapter.

3.1 NUMERICAL MODEL

A numerical model was constructed to study the forces applied by the surrounding fluid on a slide mass moving through fluid. For the numerical model, the slide mass was assumed to have a constant shape and velocity. The slide mass was represented by a streamline shaped body as shown in Figure 3.1. The front surface of the slide mass is shown in Figure 3.2 with more detail. The portion from point I to point S is a circular arc. In the local coordinate system $q-o-m$ (Figure 3.3), the arc from point I to point S is expressed as:

$$q^2 + m^2 = r^2 \quad \text{for } 0 \leq q \leq r \quad \text{and} \quad 0 \leq m \leq r \quad (3.1)$$

Where r is the radius of the arc as shown in Figure 3.1. The curve from point I to point J is part of an ellipse. In the local coordinate system $b-o-a$ (Figure 3.4), the curve from point I to point J is expressed as:

$$\left(\frac{b}{w}\right)^2 + \left(\frac{a}{H-r}\right)^2 = 1 \quad \text{for } 0 \leq b \leq w \quad \text{and} \quad 0 \leq a \leq (H-r) \quad (3.2)$$

Where H is the height of the slide mass, and w is the width of the front portion of the slide mass as shown in Figure 3.1. The ratio between the height of the slide mass (H) and the width of the front portion (w) is defined as the “height-to-width ratios” (H/w). The width of the slide mass normal to the $x-o-y$ plane in Figure 3.1 is assumed to be infinite. The reference for the coordinate system is on the slide mass, and the surrounding flow is assumed to be steady 2-D flow around a fixed rigid body. The velocities u and v of the surrounding fluid far away from the slide mass are referred to as “inflow velocities”. In the following discussion, the inflow velocity is symbolized as U in the x direction and is assumed to be zero in the y direction. A gap is assumed between the slide mass and the underlying ground for the cases where hydroplaning is assumed to occur. The bottom surface of the slide mass is assumed to be parallel to the surface of the underlying ground. The distance between the bottom surface of the slide mass and the underlying ground is designated as h . The surrounding fluid is considered to be water. The boundary conditions for the flow are illustrated in Figure 3.5 and described as follows:

1. along the left edge of the calculation domain ($x = 0$), the velocities are equal to the inflow velocities, i.e. $u = U$ and $v = 0$;
2. at the top edge of the calculation domain, the velocities are equal to the inflow velocities, i.e. $u = U$ and $v = 0$;
3. along the right edge of the calculation domain, the flow is assumed to be fully developed and, thus, does not change along the horizontal direction, i.e. $\frac{\partial u}{\partial x} = \frac{\partial v}{\partial x} = 0$;
4. the bottom edge of the calculation domain is treated as a moving, non-slip wall representing the ground surface moving relative to the slide mass with a constant horizontal velocity, i.e. $u = U$ and $v = 0$;

5. the surfaces of the slide mass are stationary non-slip walls because the slide mass does not move relative to itself, i.e. $u = 0$ and $v = 0$.

The commercial software known as, Fluent 6.1, was used for the numerical modeling. A Reynolds-Stress turbulent model was used to simulate the flow. Fluent uses an iterative scheme to solve the governing equations of flow. Convergence is determined based on the values of scaled residuals defined as the ratios of the corrections to the primitive variables divided by the primitive variables themselves for any given iteration. The primitive variables include horizontal velocity, vertical velocity and mass flow rate of the fluid. For example, the scaled residual for the horizontal velocity at the $i+1$ iteration is calculated as

$$e_u(i+1) = \frac{|u(i+1) - u(i)|}{|u(i+1)|} \quad (3.3)$$

where $u(i+1)$ is the value of horizontal velocity calculated in the $(i+1)th$ iteration, $u(i)$ is the value of horizontal velocity calculated in the $(i)th$ iteration and i is the number of iterations. In the numerical modeling all scaled residuals were required to be smaller than 10^{-5} for convergence.

The commercial software known as Gambit 2.1 was used as the preprocessor for Fluent. Gambit was used to model the geometry of the calculation domain and to generate meshes.

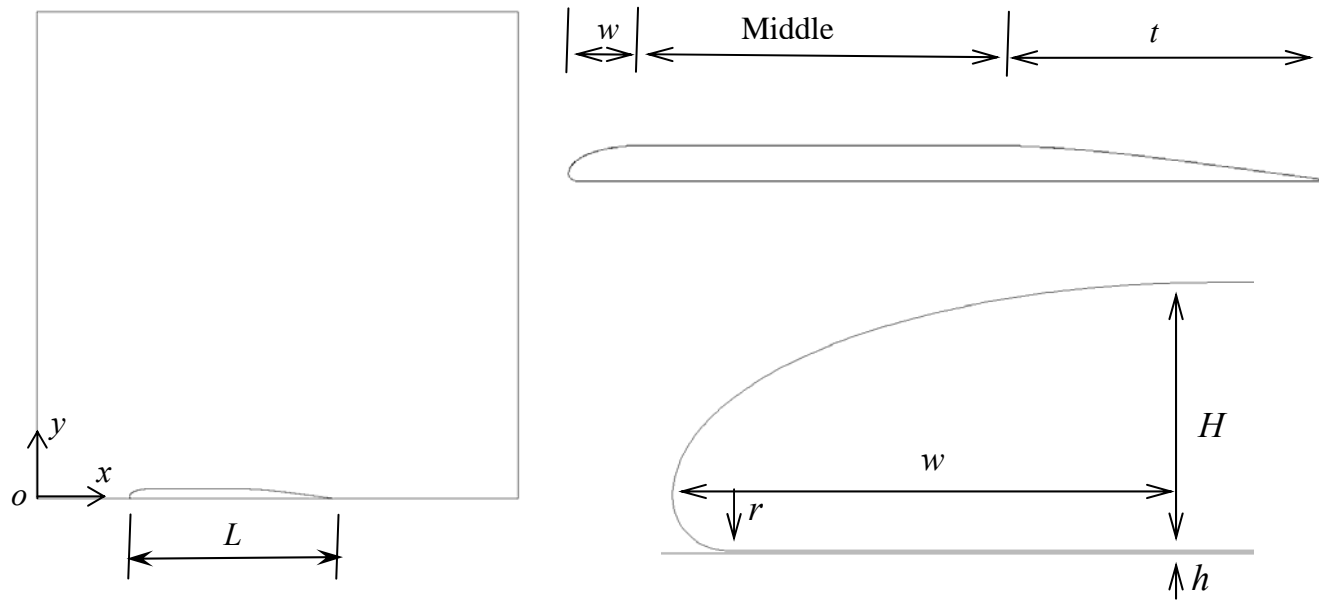


Fig. 3.1 Geometry of the numerical model

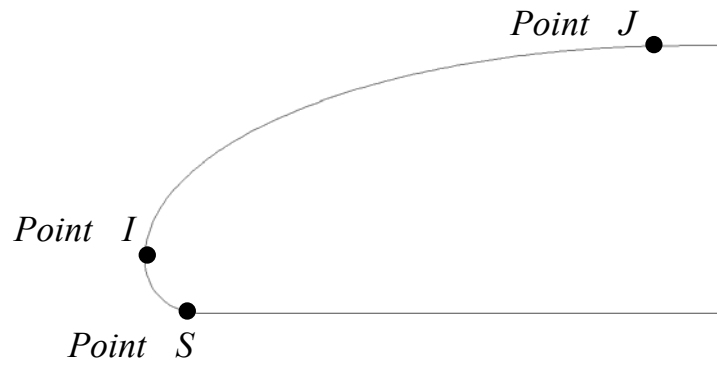


Fig. 3.2 Front of the slide mass

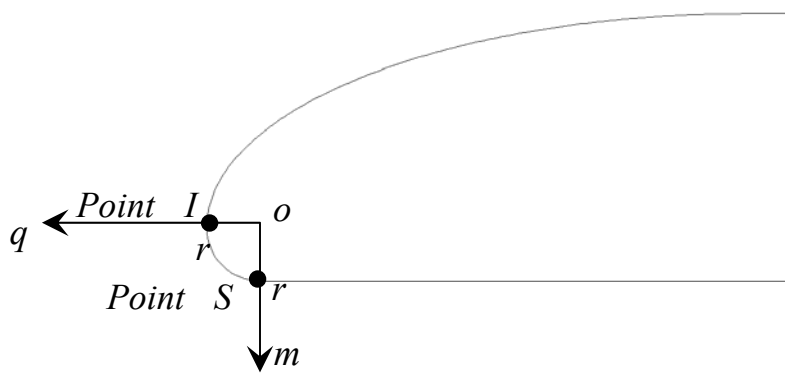


Fig. 3.3 Curve from point I to point S

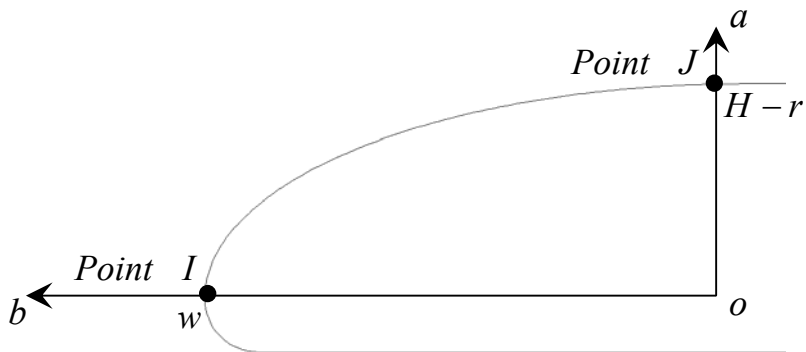


Fig. 3.4 Curve from point I to point J

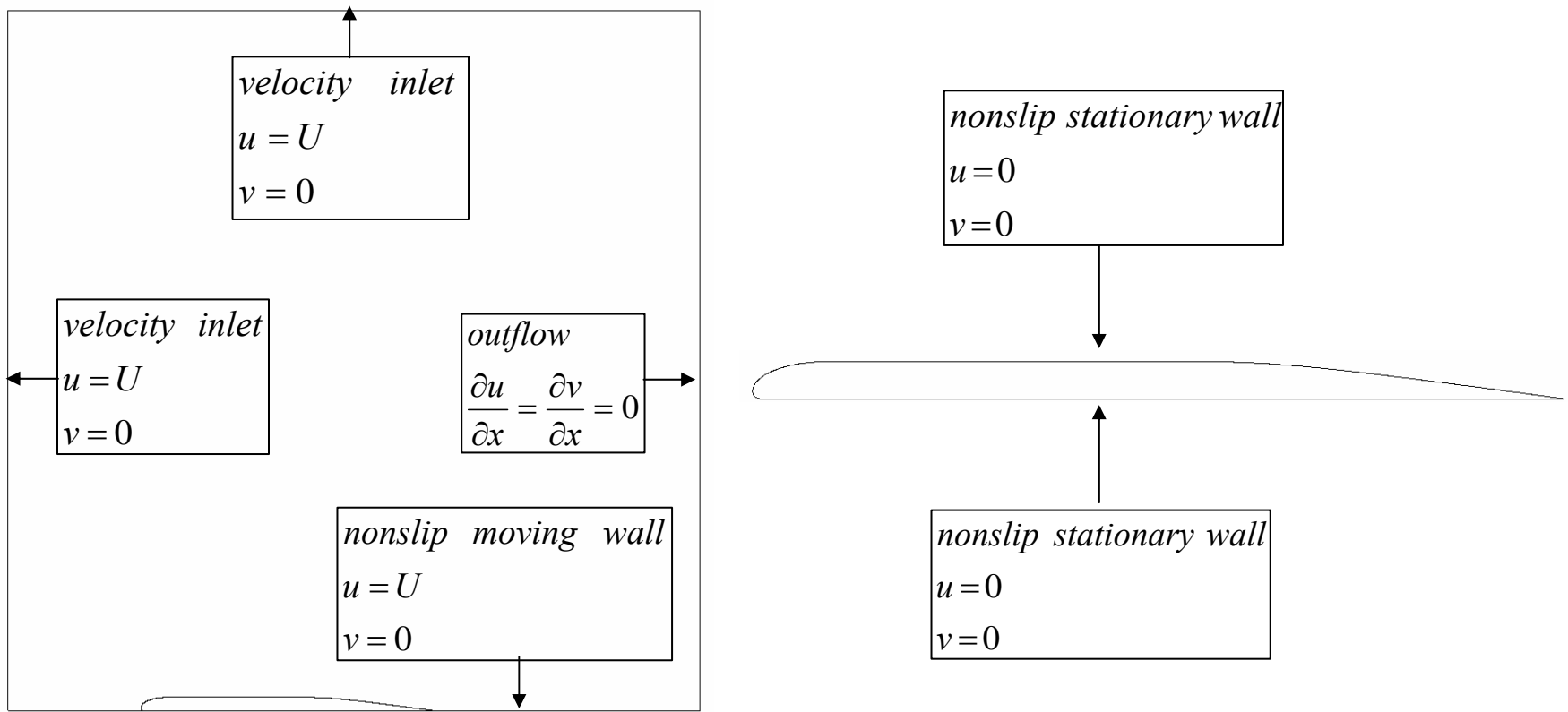


Fig. 3.5 Boundary conditions for the numerical model

3.2 NUMERICAL CASES

Ten cases were analyzed to study the hydrodynamic stresses on the slide mass. The flow conditions and objective of the ten cases are summarized in Table 3.1.

Table 3.1: Flow conditions and functions for numerical cases

Case No.	Inflow velocity U (m/s)	Distance between the bottom surface of the slide mass and underlying ground h (m)	Height-to-width ratio of front (H/w)	Objective
1	$u = 1 \quad v = 0$	0.01	0.5	Base case compared with Cases 2 to 10
2	$u = 10 \quad v = 0$	0.01	0.5	Compared with Case 1 to study the effect of slide velocity
3	$u = 1 \quad v = 0$	0.02	0.5	Compared with Case 1 to study the effect of gap thickness
4	$u = 1 \quad v = 0$	0.05	0.5	
5	$u = 1 \quad v = 0$	0.1	0.5	
6	$u = 1 \quad v = 0$	1	0.5	
7	$u = 1 \quad v = 0$	10	0.5	Compared with Case 9 to study the effect of frontal shape
8	$u = 1 \quad v = 0$	50	0.5	
9	$u = 1 \quad v = 0$	0	0.5	
10	$u = 1 \quad v = 0$	0	2.0	

3.3 NUMERICAL RESULTS

The various flow conditions and numerical results for the ten cases are discussed in this section. The results for selected cases are also compared to examine the effects of flow conditions on the hydrodynamic stresses. For presentation purposes, the hydrodynamic stresses including kinetic pressure and viscous shear are normalized by dividing the values by the corresponding stagnation pressure p_{stag} defined in Equation

2.38. The stagnation pressure p_{stag} is computed from Equation 2.38 using the inflow velocity, U .

3.3.1 Hydrodynamic Stresses

For Case 1, the geometry of the flow domain and boundary conditions are as shown in Figures 3.6 and 3.7. The inflow velocity in the x direction U is 1 m/s. The distance between the bottom surface of the slide mass and underlying ground h is 0.01 m. The height-to-width ratio H/w is 0.5. The mesh is shown in Figure 3.8 and consists of 594812 rectangular and triangular elements.

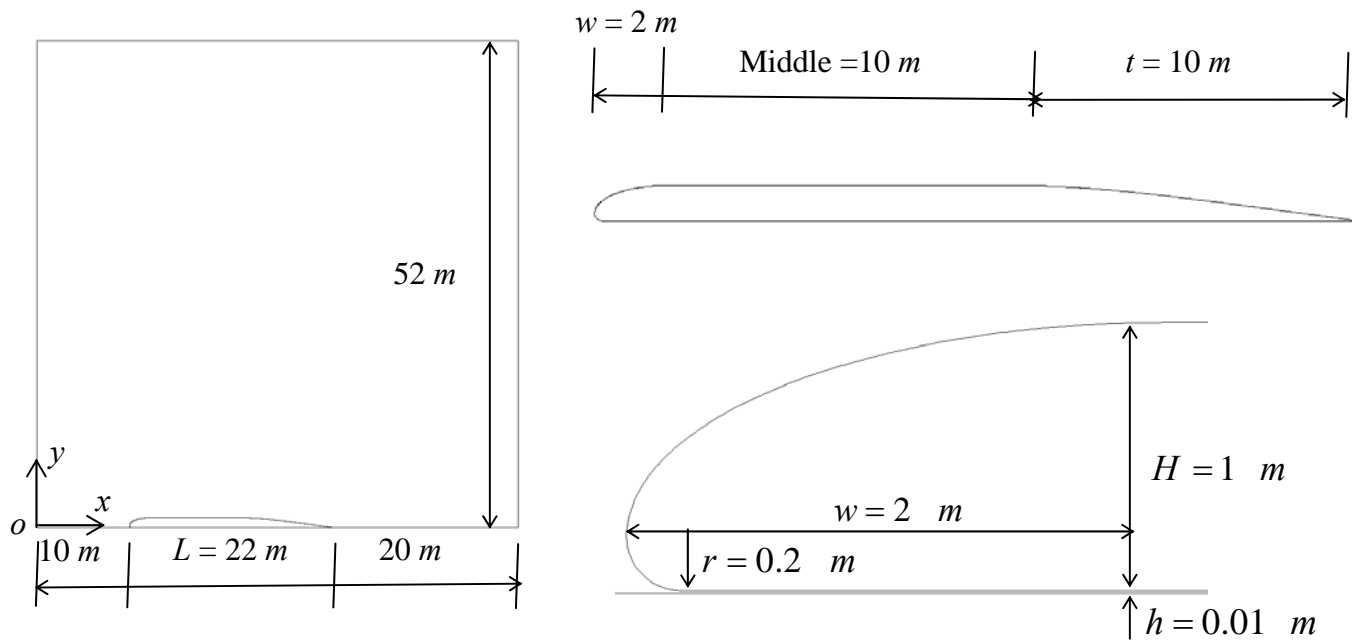


Fig. 3.6 Geometry for Case 1 ($U = 1\text{ m/s}$; $h = 0.01\text{ m}$; $H/w = 0.5$)

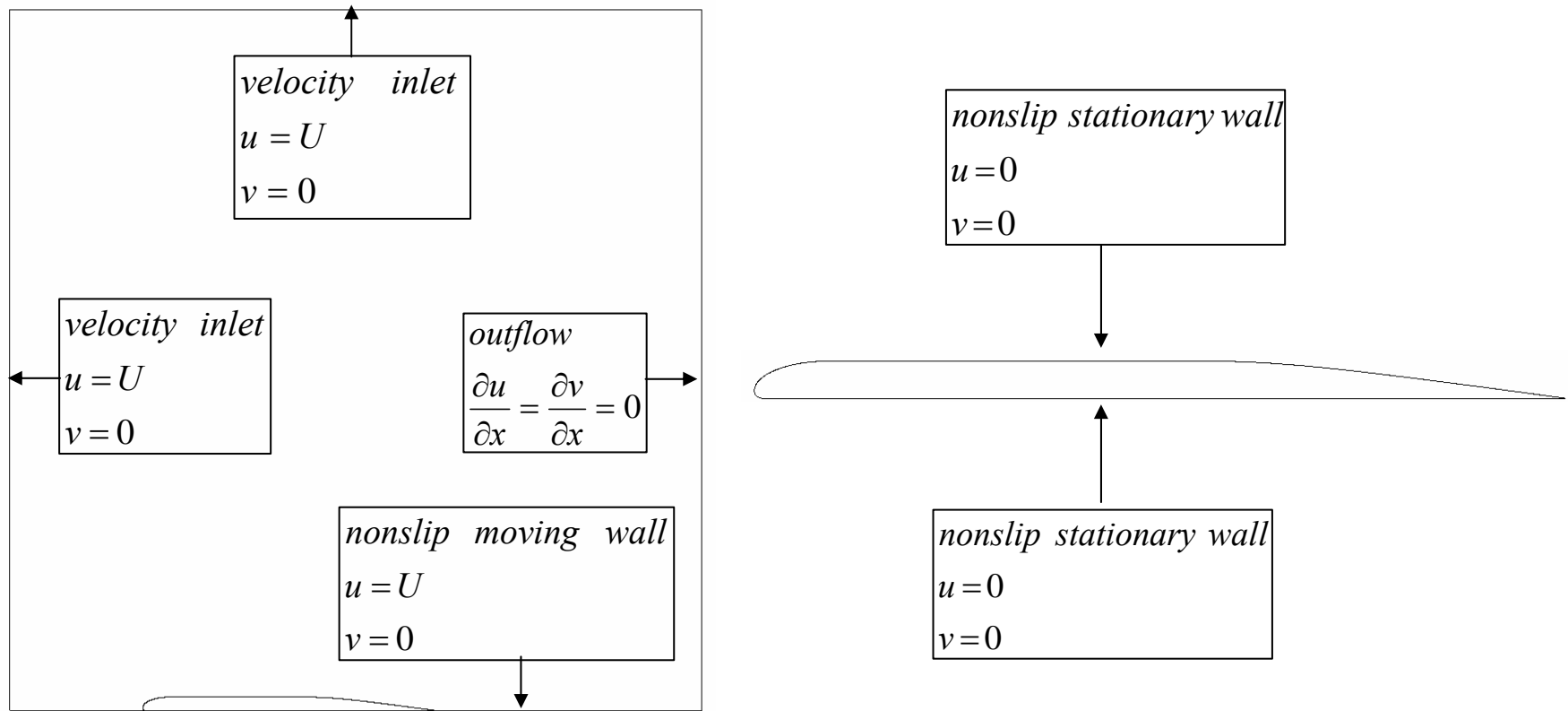


Fig. 3.7 Boundary conditions for Case 1 ($U = 1 \text{ m/s}$; $h = 0.01 \text{ m}$; $H/w = 0.5$)

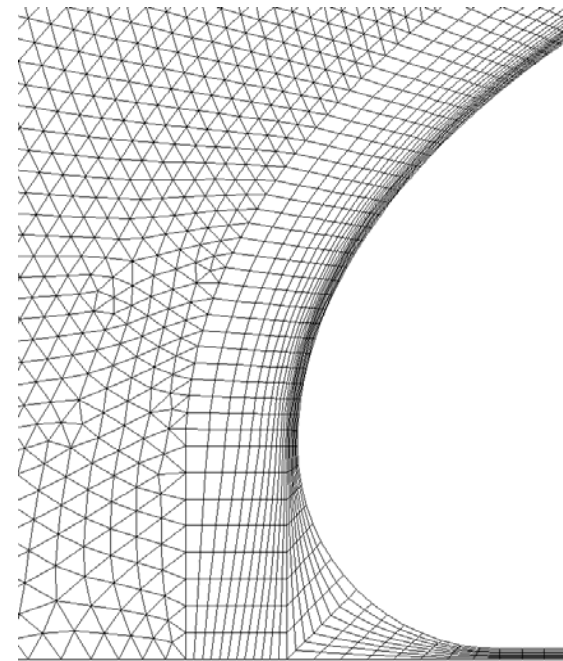
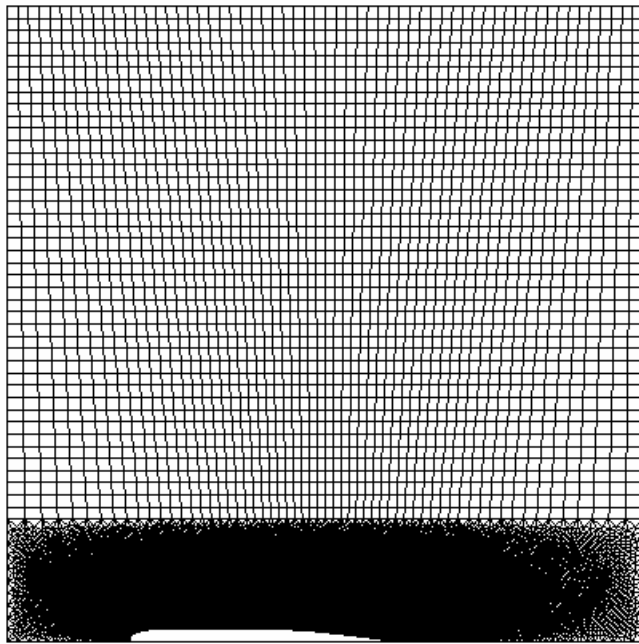


Fig. 3.8 Mesh for Case 1 ($U = 1 \text{ m/s}$; $h = 0.01 \text{ m}$; $H/w = 0.5$)

3.3.1.1 Kinetic pressures

The variation in computed non-dimensional kinetic pressures along the top and bottom surfaces of the slide mass with the horizontal position is shown in Figure 3.9. As shown in Figure 3.9, the non-dimensional kinetic pressure is about 1.0 at the front nose of the slide mass. For discussion of the pressure p_b / p_{stag} along the bottom surface, the bottom surface of the slide mass is divided into two portions. The first portion is the curved portion from point I to point S as shown in Figure 3.2. The second portion is the remainder of the bottom surface. As shown in Figure 3.2, the length of first portion is much smaller than that of the second portion. Therefore, it seems reasonable to neglect the kinetic pressure over the first portion. Along the second portion of the bottom surface, the non-dimensional pressure, p_b / p_{stag} varies linearly. The pressure p_b / p_{stag} at the beginning of the second portion of the bottom surface of the slide mass is about 0.88 and marked by an inverted triangle in Figure 3.9. The pressure p_b / p_{stag} decreases to about 0.3 at the tail of the side mass. For discussion of the normalized pressure p_t / p_{stag} along the top surface of the slide mass, the top surface is divided into three portions. The first portion is the curved portion from point I to point J shown in Figure 3.2. The pressure p_t / p_{stag} along this portion is negative and provides lift on the slide mass. The second portion is the middle portion of the top surface as shown in Figure 3.1. The normalized pressure p_t / p_{stag} in this portion is constant at -0.1. The third portion is the remainder of the top surface. The normalized pressure p_t / p_{stag} in this portion varies linearly from about -0.1 to 0.3 at the tail end of the slide mass.

As discussed above, the normalized pressure, p_t / p_{stag} , along the middle portion of the top surface has a negative value. This negative value of pressure p_t / p_{stag} is believed to be a reflection of limitations of the numerical model. As shown in Figure 3.6, the total height of the calculation domain (slide mass and surrounding fluid) is 52 m, which is only about 2.4 times the length of the slide mass (22 m). For natural submarine

slides, the slide mass moves along the bottom of the ocean and the depth of the sea water is probably more than 10 times the length of the slide mass. Thus for actual submarine slides, it is reasonable to assume that the top edge of the flow domain is essentially infinitely far from the slide mass. The flow above the middle portion of the slide mass can then be approximated as flow above an infinitesimally thin plate. According to the boundary layer theory (Crowe, and et al. 2000), the kinetic pressure above an infinitesimally thin plate is zero. Therefore, the non-dimensional pressure p_t / p_{stag} on the middle portion of the top surface of an actual submarine slide is probably zero. The non-dimensional pressure p_t / p_{stag} on the tail portion of the top surface increases linearly from zero beginning at the start of tail portion to 0.3 at the end of the tail portion.

3.3.1.2 Reexamination of the on-set condition of hydroplaning

As discussed in section 2.5.2, hydroplaning was expected to happen when the Froude number Fr_d was $\sqrt{2}$ according to Equation 2.45. This expectation was based on a common assumption adopted by Harbitz et al. (2003) and De Blasio et al. (2004) that the kinetic pressure, p_b , along the bottom surface of the slide mass was the only stress applied by the surrounding fluid in the direction normal to the underlying slope. This assumption is clearly unrealistic because the pressure p_t / p_{stag} along the front portion of the slide mass, i.e. the curved portion from point *I* to point *J* shown in Figure 3.2, is negative. Taking this negative pressure, p_t / p_{stag} , into consideration, hydroplaning should occur when the stagnation pressure p_{stag} is smaller than the normal stress σ_w along the bottom surface of the slide mass. Therefore the critical Froude number $Fr_{d,crit}$ for hydroplaning to happen should be smaller than $\sqrt{2}$, which agrees with the experimental observations by Mohrig, et al and the arbitrary assumptions made by De Blasio, et al.

3.3.1.3 Viscous shears

The distributions of the normalized shear stresses along the top and bottom surfaces of the slide mass τ_t / p_{stag} , τ_b / p_{stag} are shown in Figure 3.10. The normalized shear stresses shown in Figure 3.10 are much smaller than the normalized pressures shown in Figure 3.9.

For comparison, the shear stresses were also calculated using the analytical solution developed for flow above a smooth flat plate as:

$$\tau_x = \frac{1}{2} \rho_w U^2 \left(\frac{0.027}{\left(\frac{Ux}{\nu} \right)^{1/7}} \right) \quad (3.4)$$

where x is the distance from the upstream end of the plate or slide mass to the location of concern, τ_x is the shear stress at a location x , ρ_w is the density of water, U is the inflow velocity in the x direction, and ν is the kinematic viscosity of water. Further details regarding the analytical solution can be found in Crowe, Roberson and Elger (2000). The shear stresses calculated using Equation 3.4 were also normalized by the stagnation pressure p_{stag} and plotted in Figure 3.10 as the “analytical solution”. It can be seen that the shear stresses calculated using Equation 3.4 are close to the ones from the numerical analyses with Fluent. Thus, the analytical solution for shear stresses developed for flow above a smooth flat plate seems to provide an acceptable approximation for the shear stresses on the slide mass.

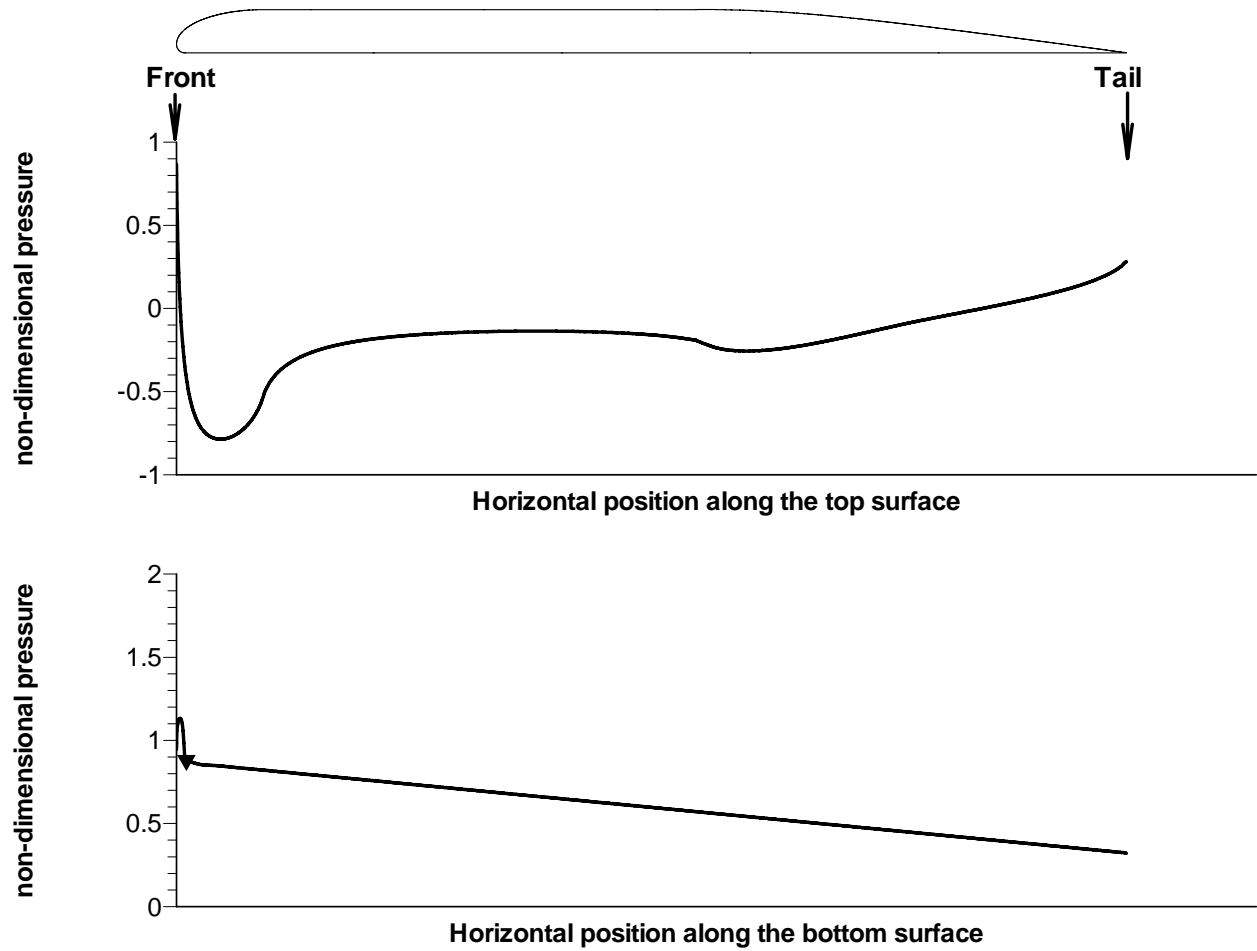


Fig. 3.9 Non-dimensional kinetic pressures for Case 1 ($U = 1 \text{ m/s}$; $h = 0.01 \text{ m}$; $H/w = 0.5$)

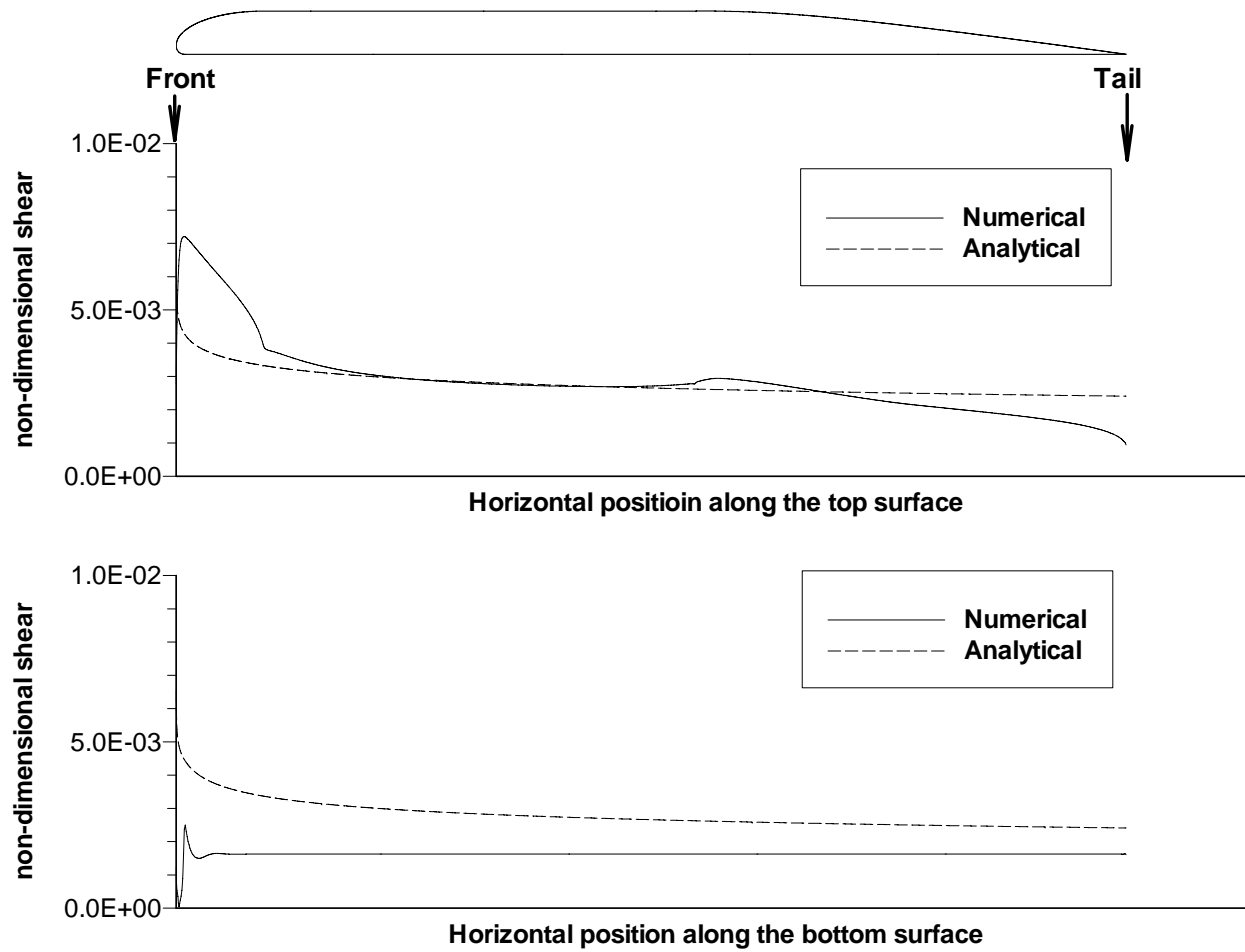


Fig. 3.10 Non-dimensional shear stress for Case 1 ($U = 1 \text{ m/s}$; $h = 0.01 \text{ m}$; $H/w = 0.5$)

3.3.2 Effect of Inflow Velocity

In order to study the effect of the inflow velocity on the hydrodynamic stresses on a slide mass, Case 2 was analyzed with an inflow velocity U of 10 m/s. The geometry for Case 2 is the same as that for Case 1. The distance between the bottom surface of the slide mass and underlying ground h is also 0.01 m, and the height-to-width ratio H/w is 0.5. The same mesh used for Case 1 was used for Case 2.

3.3.2.1 Effect of inflow velocity on kinetic pressures

The normalized kinetic pressures for Cases 1 and 2 are shown together in Figure 3.11. The non-dimensional pressures for these two cases are nearly identical. Along the top surface of the slide mass, the non-dimensional pressure p_t / p_{stag} are so close that it is hard to distinguish the pressures for Case 1 from those for Case 2. Therefore the influence of inflow velocity on the non-dimensional kinetic pressure is negligible.

3.3.2.2 Effect of inflow velocity on viscous shears

The non-dimensional shear stresses on the surface of the slide mass for Case 2 are shown in Figure 3.12. The shear stresses are also computed using Equation 3.4. After divided by the stagnation pressure p_{stag} , the computed shear stresses are also plotted in Figure 3.12 as analytical solution. It can be seen that the shear stresses calculated using Equation 3.4 are close to the numerical results. Therefore the analytical solution for shear stresses developed for flow above a smooth flat plate appears to provide acceptable approximation for shear stresses on the slide mass regardless of the inflow velocity.

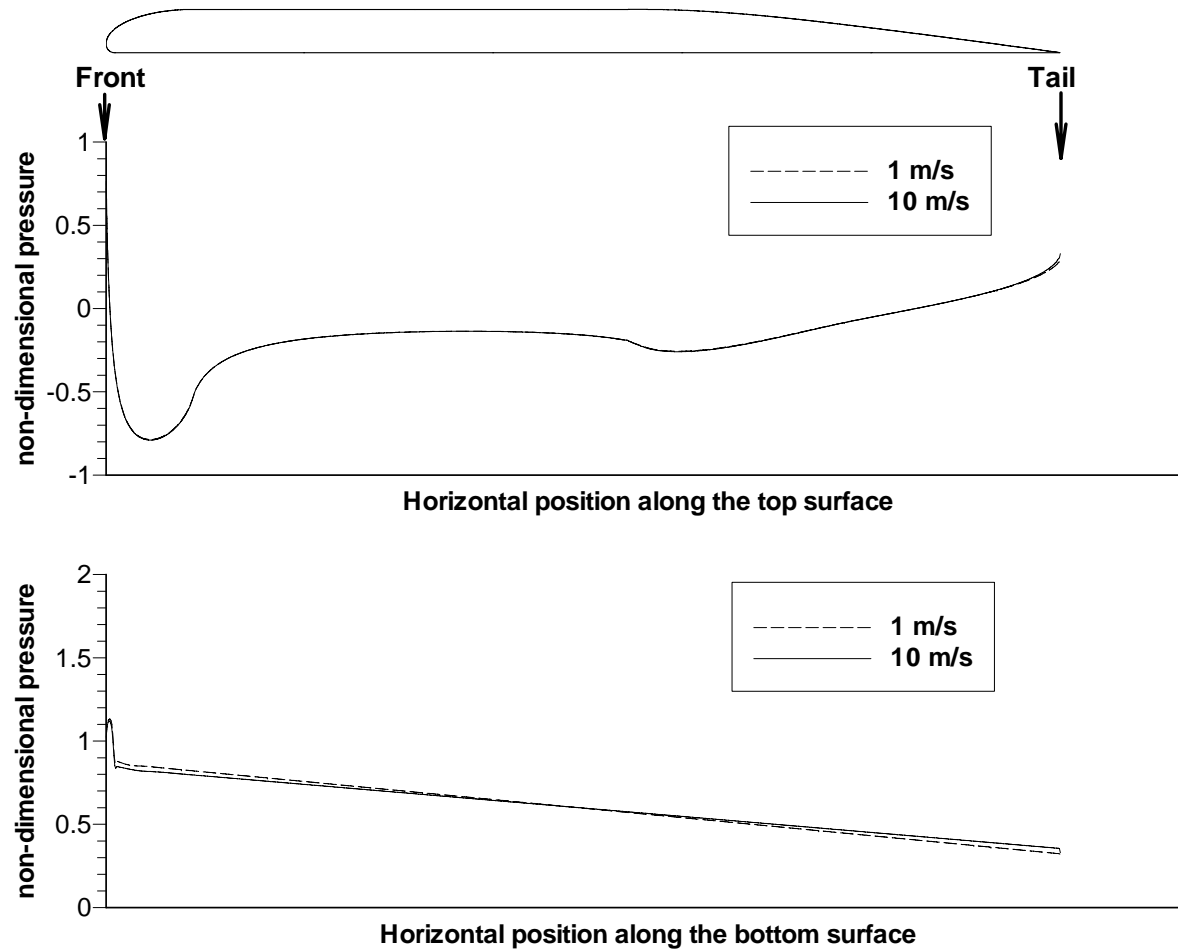


Fig. 3.11 Non-dimensional shear stress for Case 1($U = 1 \text{ m/s}$; $h = 0.01 \text{ m}$; $H/w = 0.5$) and Case 2($U = 10 \text{ m/s}$; $h = 0.01 \text{ m}$; $H/w = 0.5$)

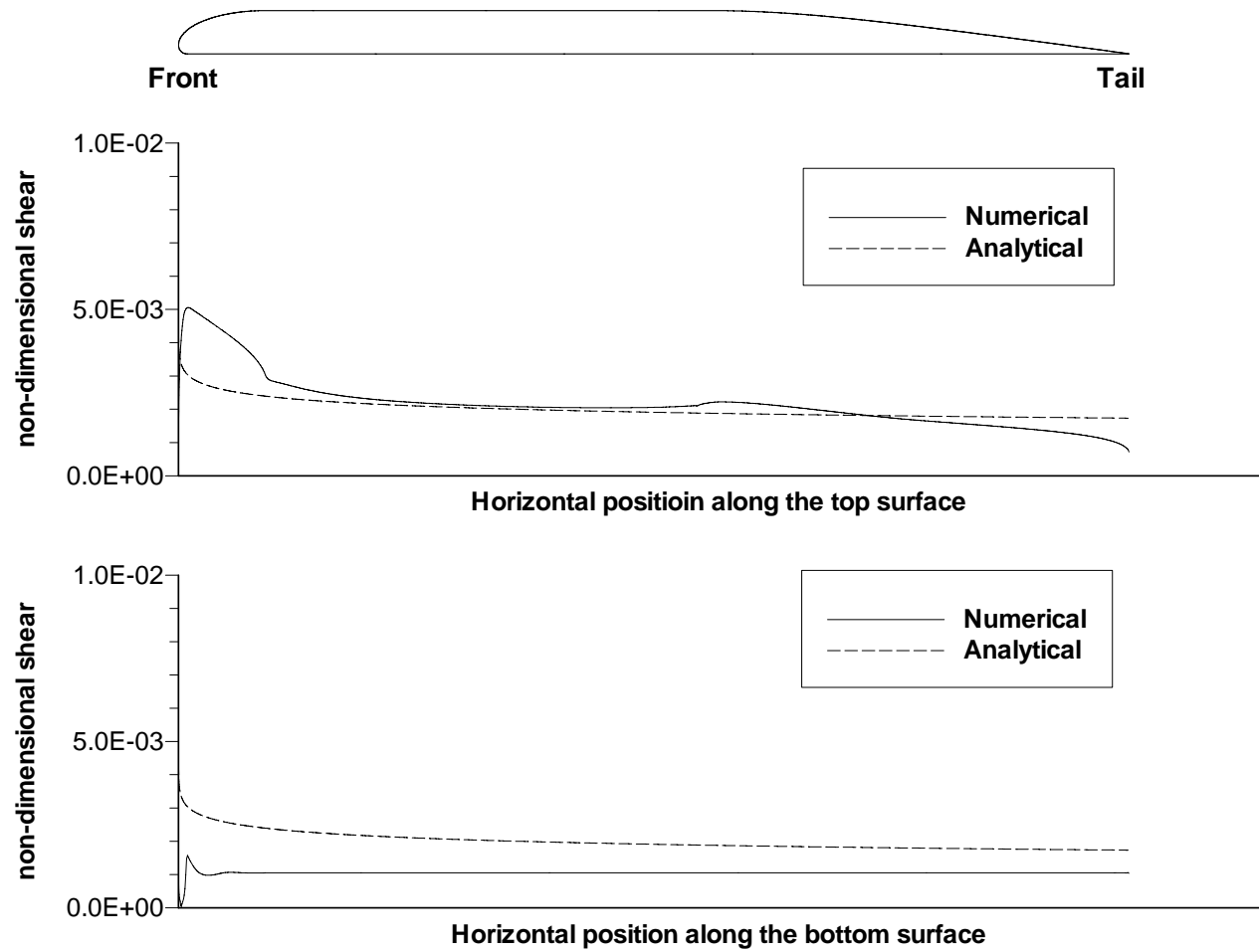


Fig. 3.12 Non-dimensional shear stress for Case 2 ($U = 10 \text{ m/s}$; $h = 0.01 \text{ m}$; $H/w = 0.5$)

3.3.3 Effect of Distance between the Bottom Surface of the Slide Mass and Underlying Ground

In order to study the influence of distance between the bottom surface of the slide mass and underlying ground h on the hydrodynamic forces applied to the surfaces of the slide mass, Cases 3 to 8 were analyzed with distances h of 0.02m, 0.05m, 0.1m, 1m, 10m, and 50m respectively.

3.3.3.1 Effect of distance h on kinetic pressures

The non-dimensional kinetic pressures along the surfaces of the slide mass for Cases 3 to 8 are shown in Figures 3.13 through 3.18, respectively. For comparison, the non-dimensional kinetic pressures along the top surface of the slide mass for all six cases are plotted together in Figure 3.19. It can be seen that the change of pressures along the top surface of the slide mass (p_t / p_{stag}) is insignificant as the distance, h , changes.

As shown in Figures 3.13 to 3.18, along the bottom surface of the slide mass the pressures p_b / p_{stag} decrease almost linearly beginning at a point after a very short distance behind the front nose of the slide mass to the tail of the slide mass. The pressures p_b / p_{stag} at the beginning of this linear variation are marked by triangles in Figure 3.13 to 3.18. Again for comparison, the non-dimensional pressures at the bottom surface p_b / p_{stag} for all six cases are plotted together in Figure 3.19. It can be seen the non-dimensional pressure along the bottom surface of the slide mass p_b / p_{stag} changes when the distance h changes. The non-dimensional pressures marked by triangles in Figures 3.13 to 3.18 are plotted against the ratios of distance h to height of the slide mass H (h/H) in Figure 3.20. The non-dimensional pressures at the tail end of the slide mass are also plotted against the ratios h/H in Figure 3.21. Smooth curves are fitted to the data points in Figures 3.20 and 3.21. The equation for the curves in Figures 3.20 and 3.21 is as follows

$$\frac{p}{p_{stag}} = \frac{1}{1 + \alpha \left(\frac{h}{H}\right)^\beta} \quad \text{for } h > 0 \quad (3.5)$$

where α is 2.57, and β is 0.58 for the curve in Figure 3.20, and α is 0.15, and β is 0.4 for the curve in Figure 3.21.

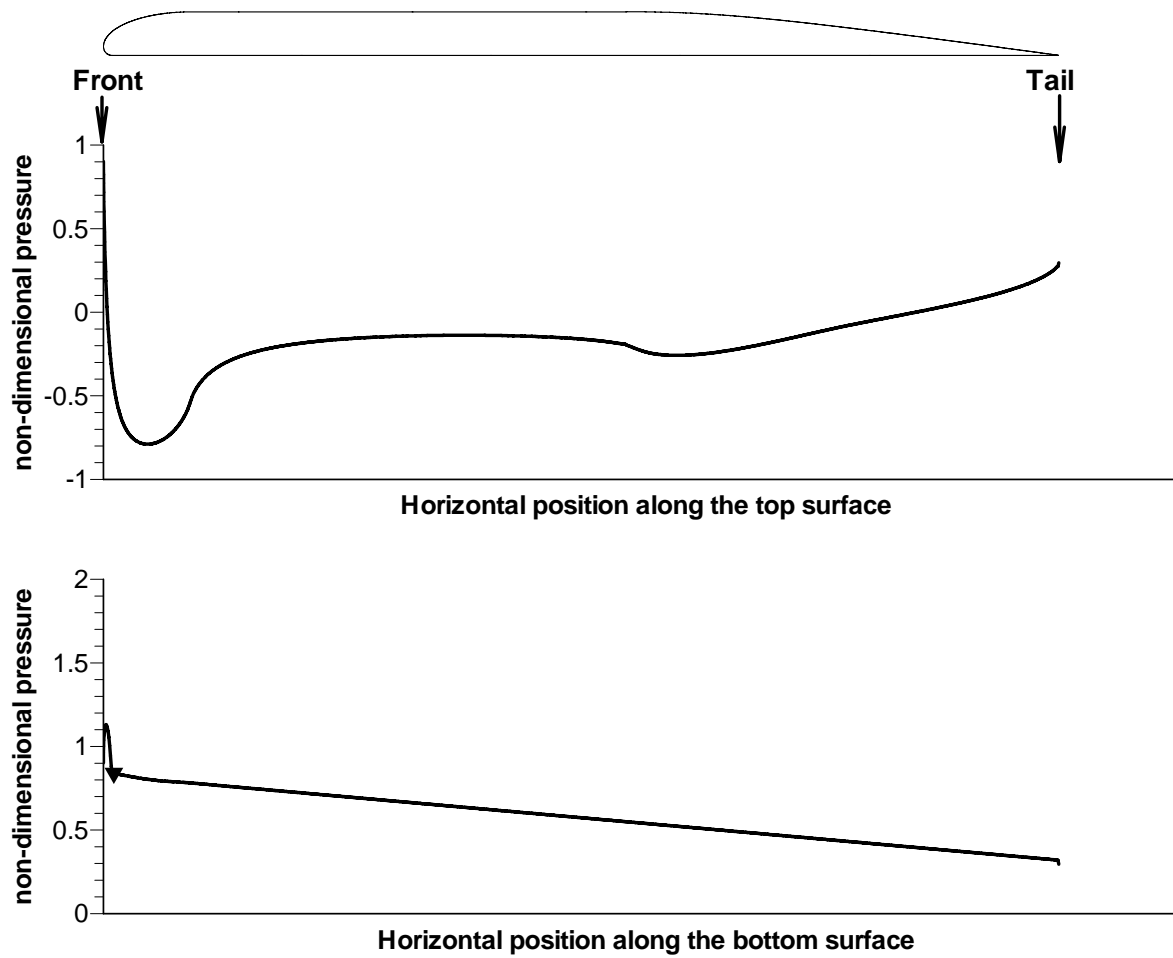


Fig. 3.13 Non-dimensional kinetic pressure for Case 3 ($U = 1 \text{ m/s}$; $h = 0.02 \text{ m}$; $H/w = 0.5$)

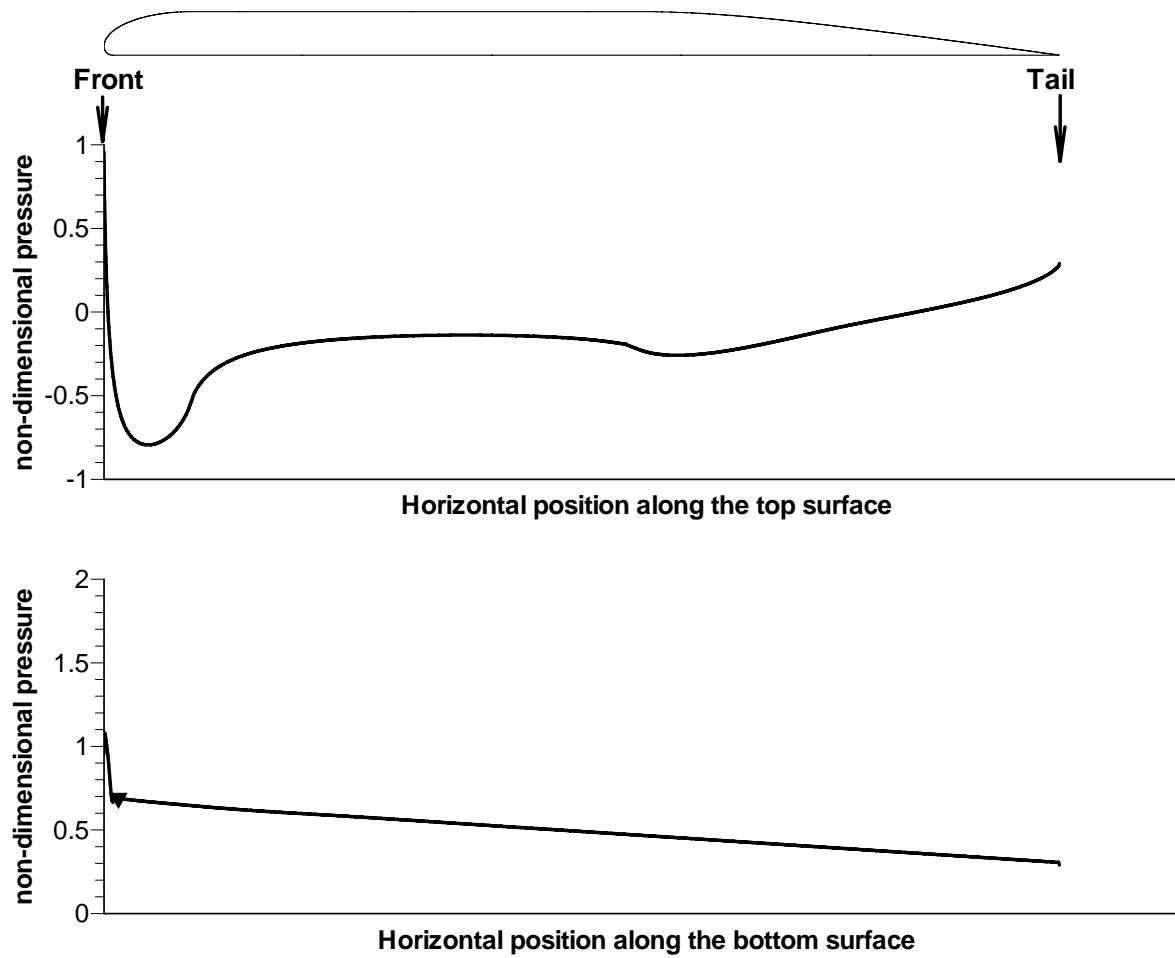


Fig. 3.14 Non-dimensional kinetic pressure Case 4($U = 1 \text{ m/s}$; $h = 0.05 \text{ m}$; $H/w = 0.5$)

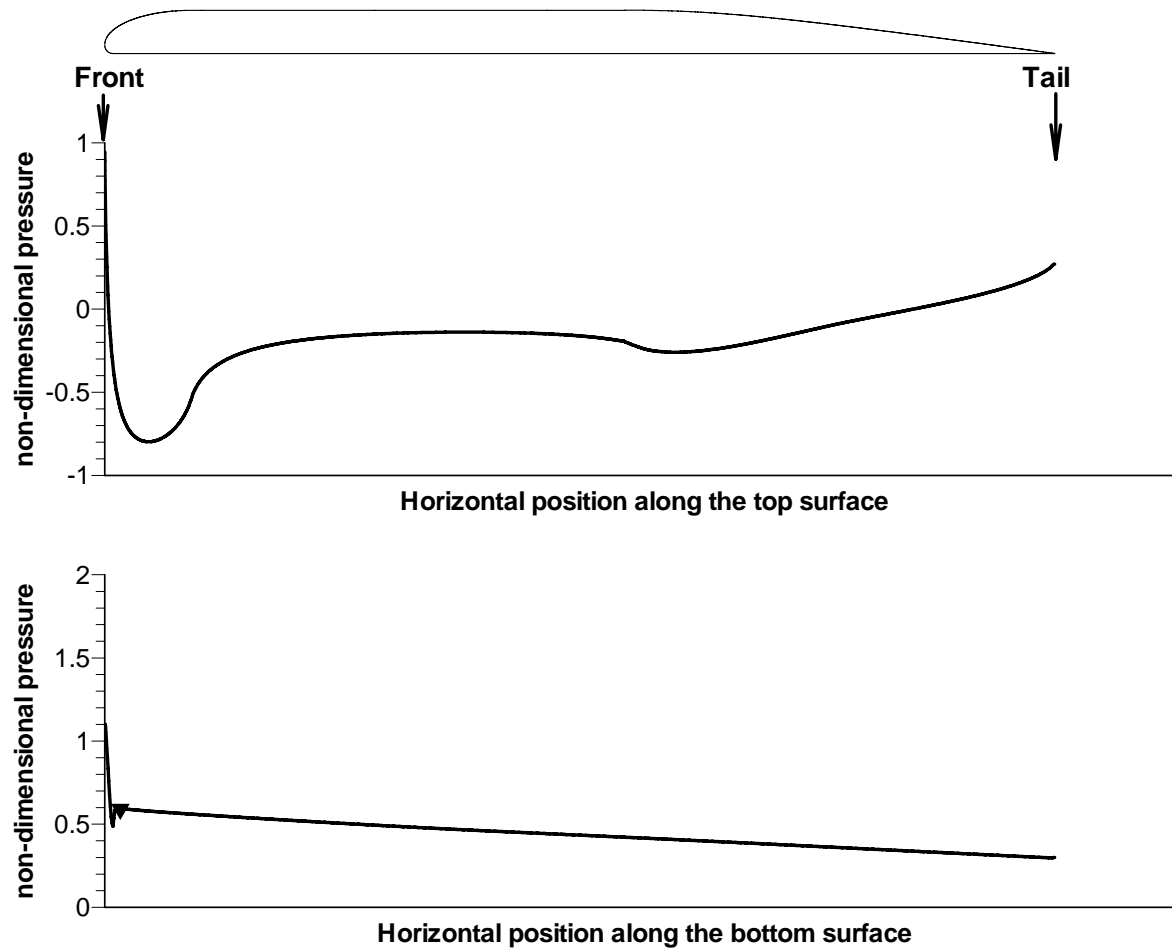


Fig. 3.15 Non-dimensional kinetic pressure for Case 5 ($U = 1 \text{ m/s}$; $h = 0.1 \text{ m}$; $H/w = 0.5$)

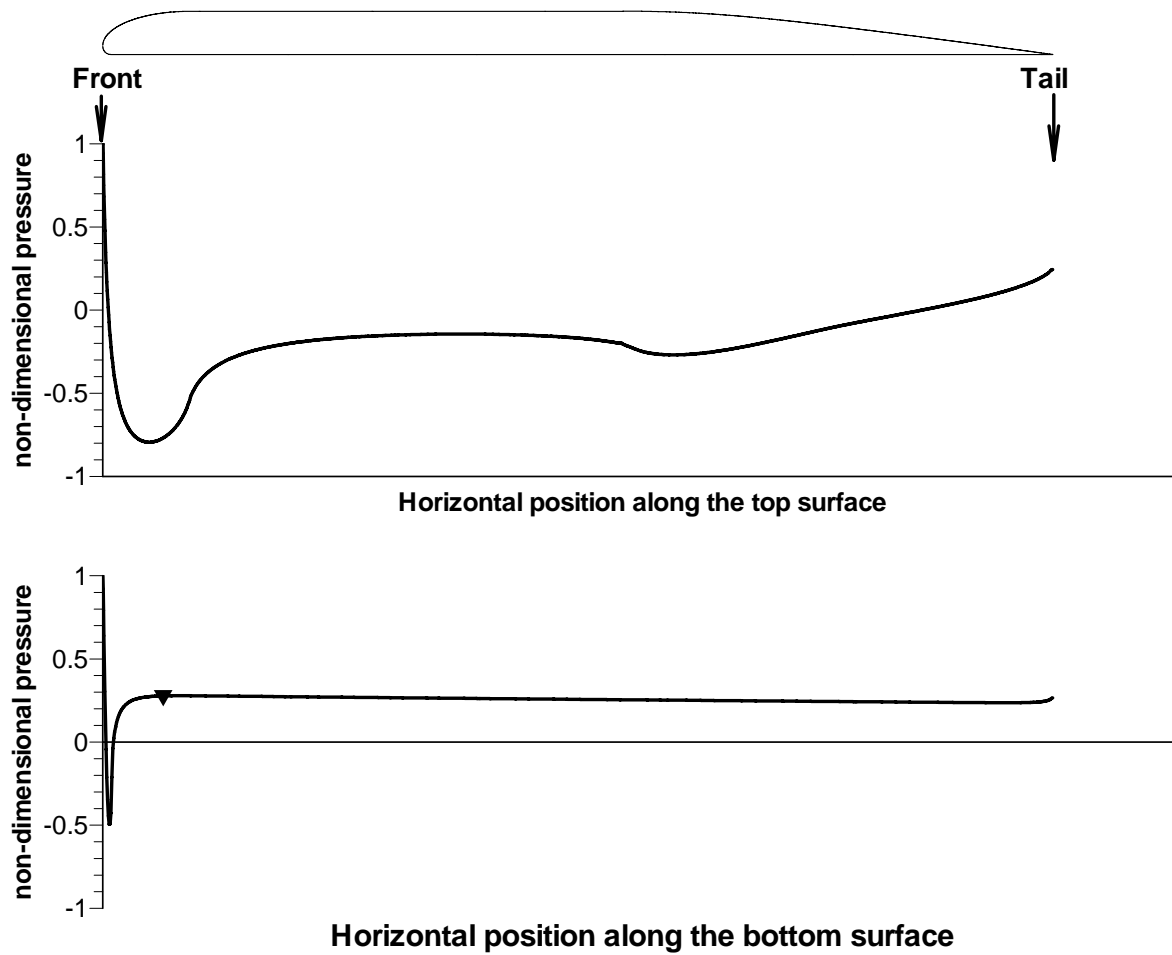


Fig. 3.16 Non-dimensional kinetic pressure for Case 6 ($U = 1 \text{ m/s}$; $h = 1 \text{ m}$; $H/w = 0.5$)

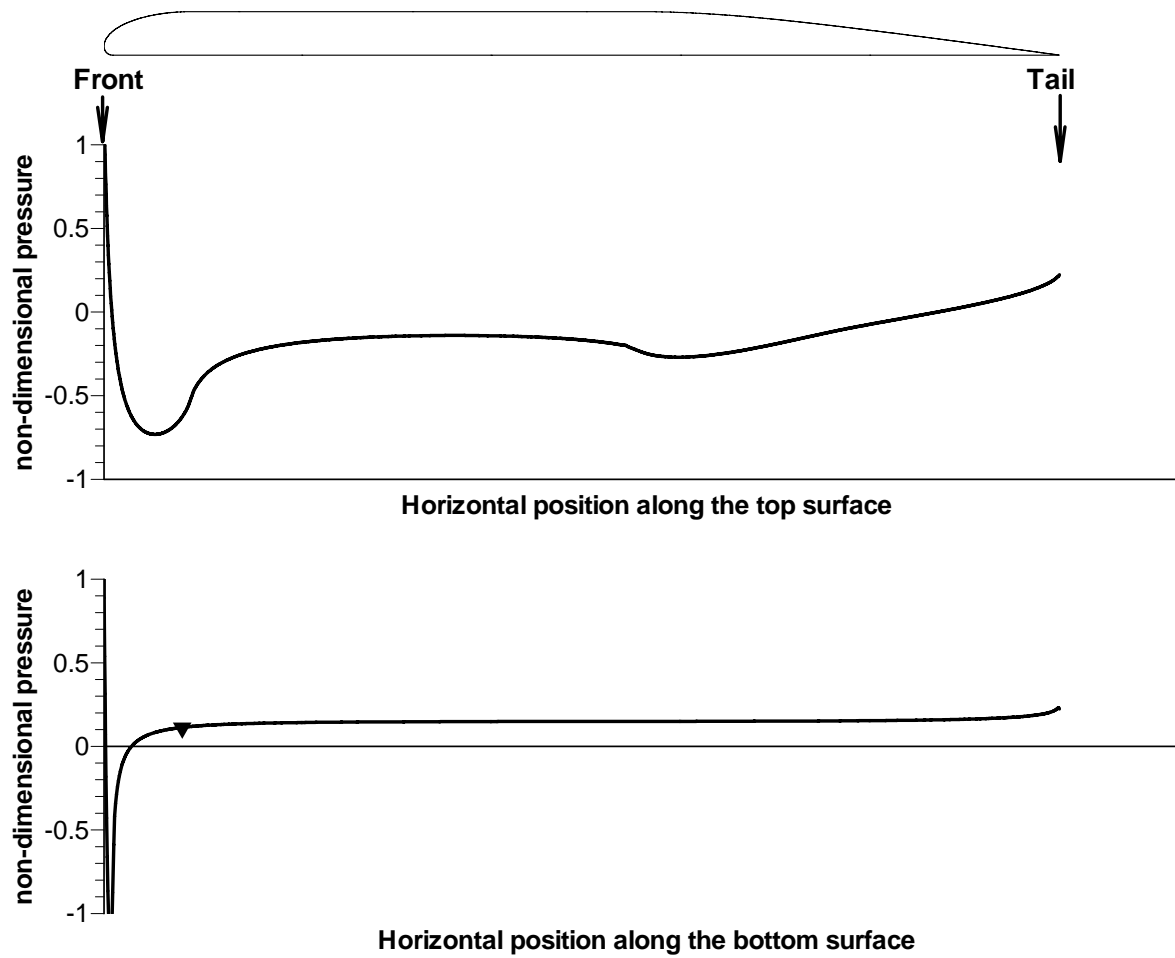


Fig. 3.17 Non-dimensional kinetic pressure for Case 7 ($U = 1 \text{ m/s}$; $h = 10 \text{ m}$; $H/w = 0.5$)

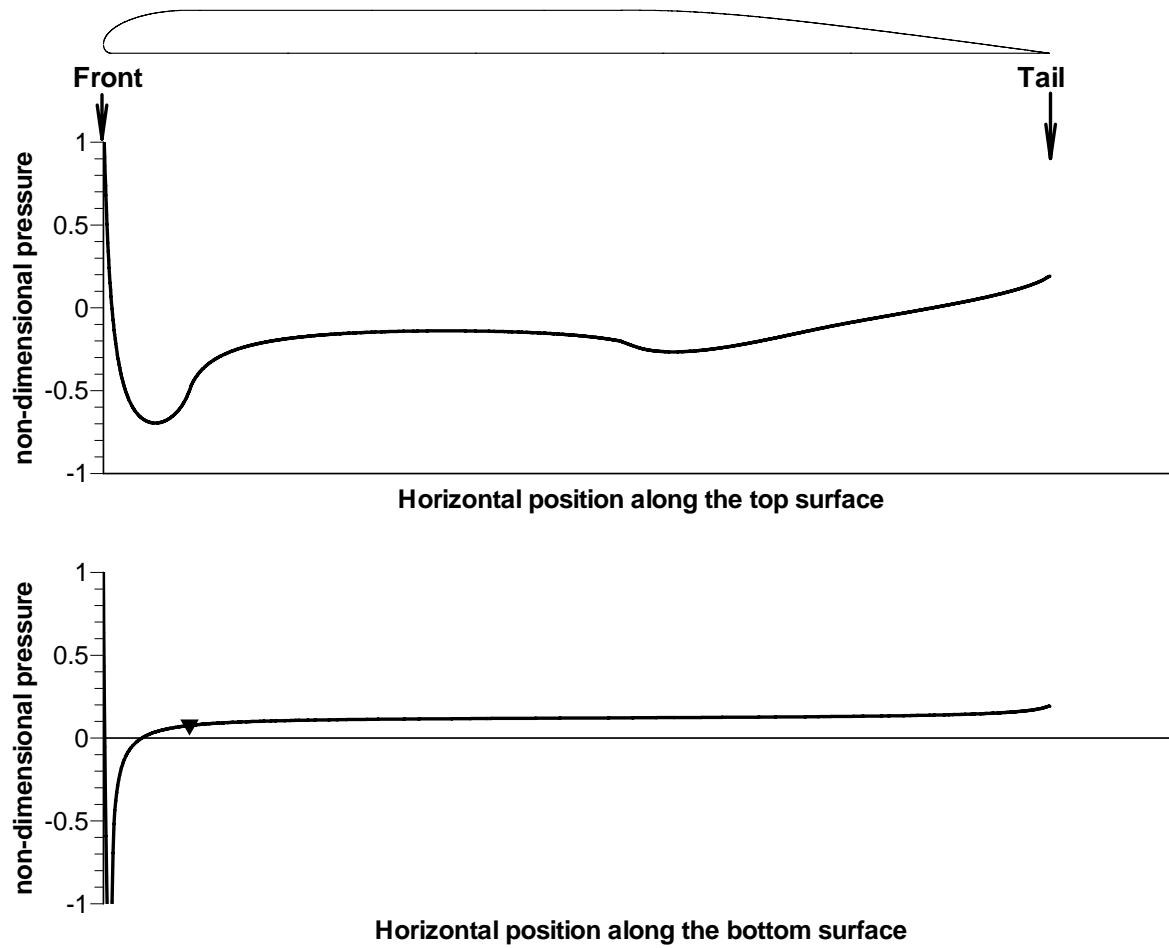


Fig. 3.18 Non-dimensional kinetic pressure for Case 8 ($U = 1 \text{ m/s}$; $h = 50 \text{ m}$; $H/w = 0.5$)

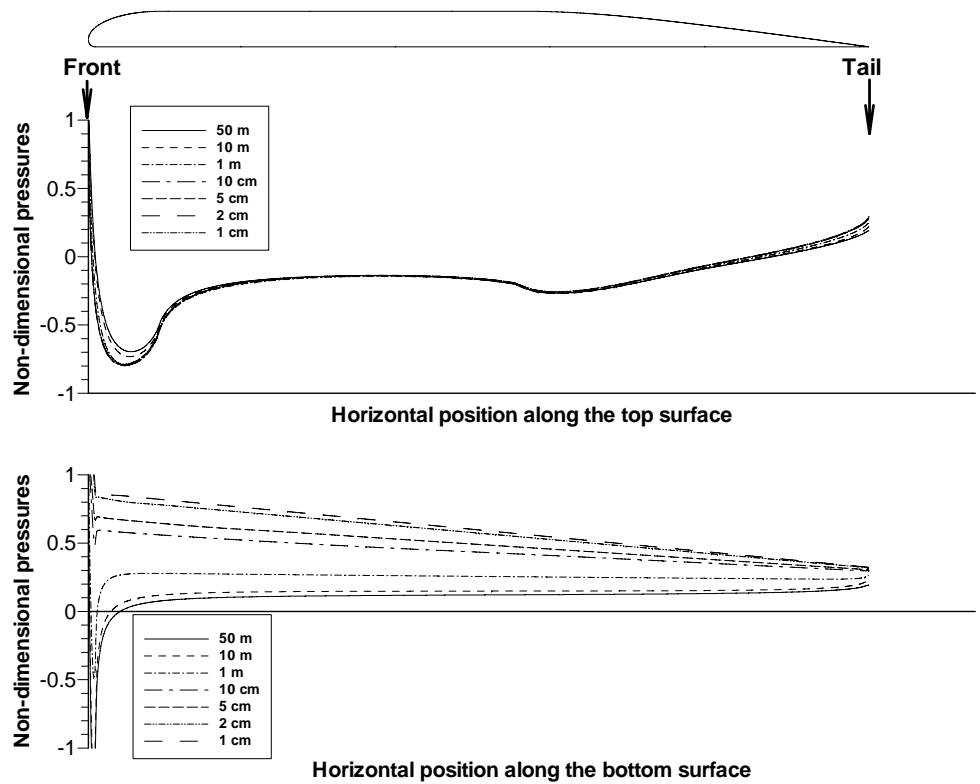


Fig. 3.19 Change of non-dimensional kinetic pressure with distance h

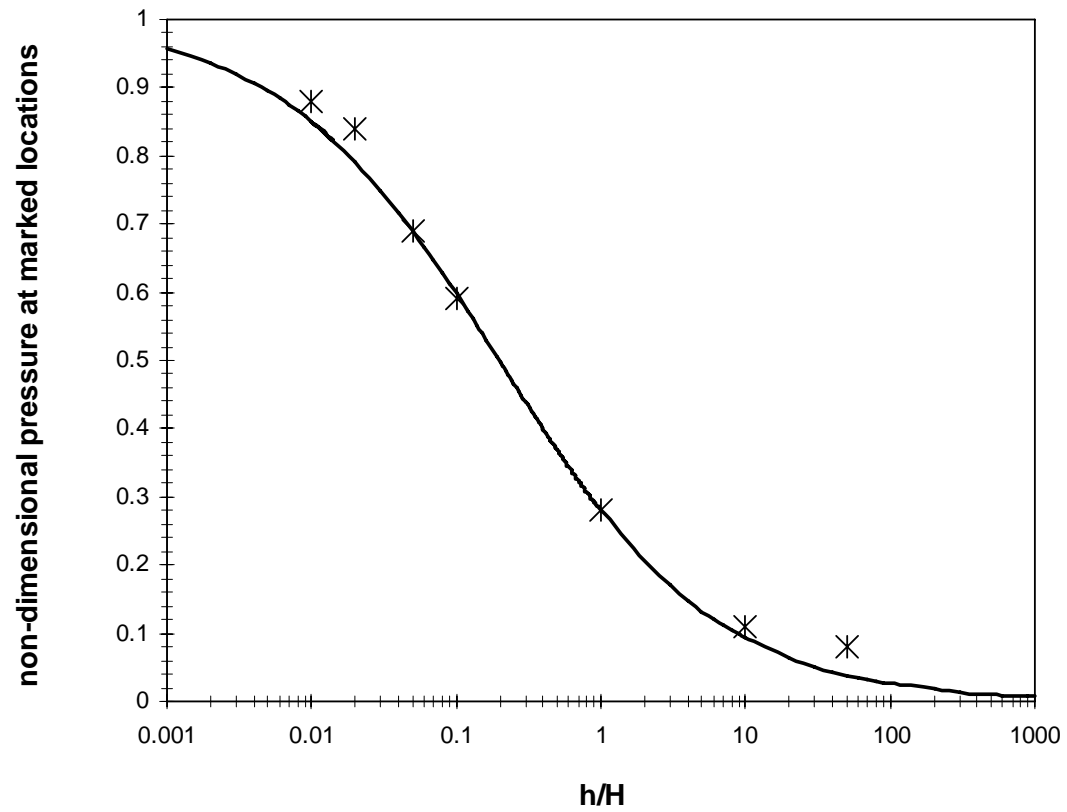


Fig. 3.20 Marked non-dimensional kinetic pressures vs h/H

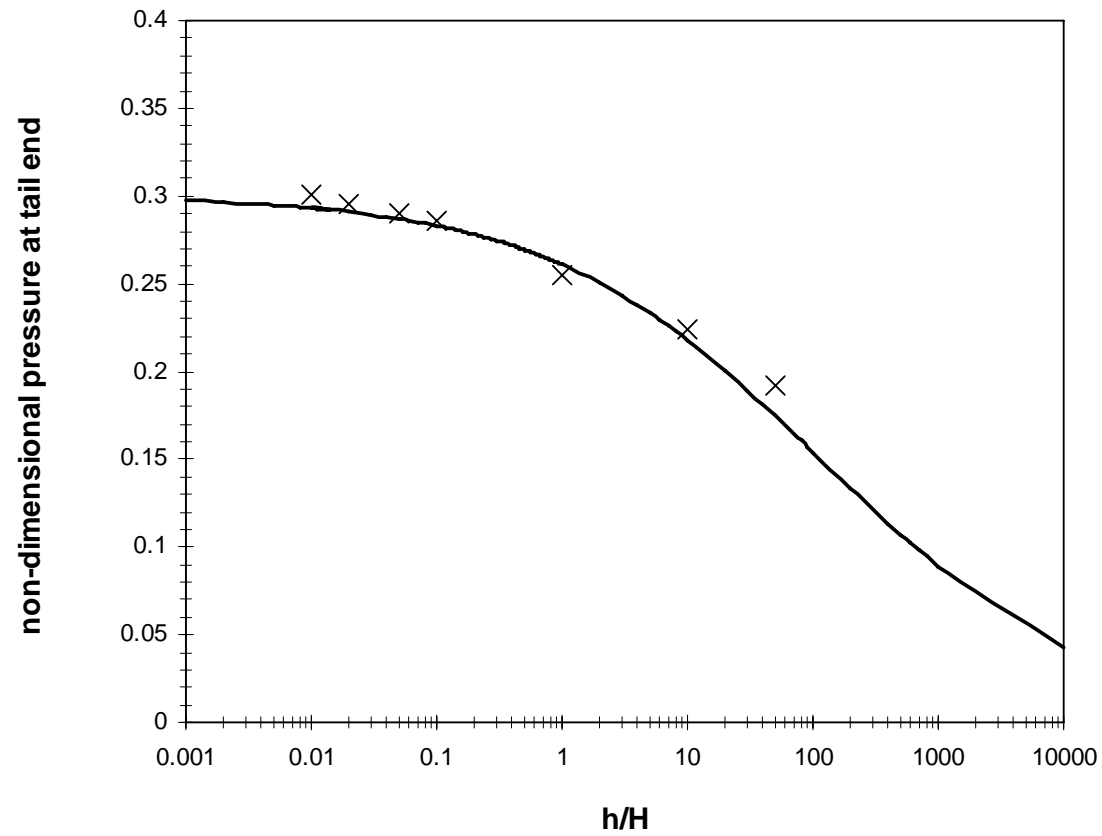


Fig. 3.21 Non-dimensional kinetic pressure at tail end of the slide mass vs h

3.3.3.2 Effect of distance h on viscous shears

The non-dimensional shear stresses for cases 3 to 8 are shown in Figures 3.22 through 3.27, respectively. The shear stresses calculated using Equation 3.4 are normalized by the stagnation pressure p_{stag} and also plotted in Figures 3.22 to 3.27. It can be seen that the shear stresses computed using Equation 3.4 are close to those from the numerical simulations. Therefore the analytical solution for shear stresses developed for flow above a smooth flat plate appears to provide an acceptable approximation for shear stresses on the slide mass regardless of the distance, h .

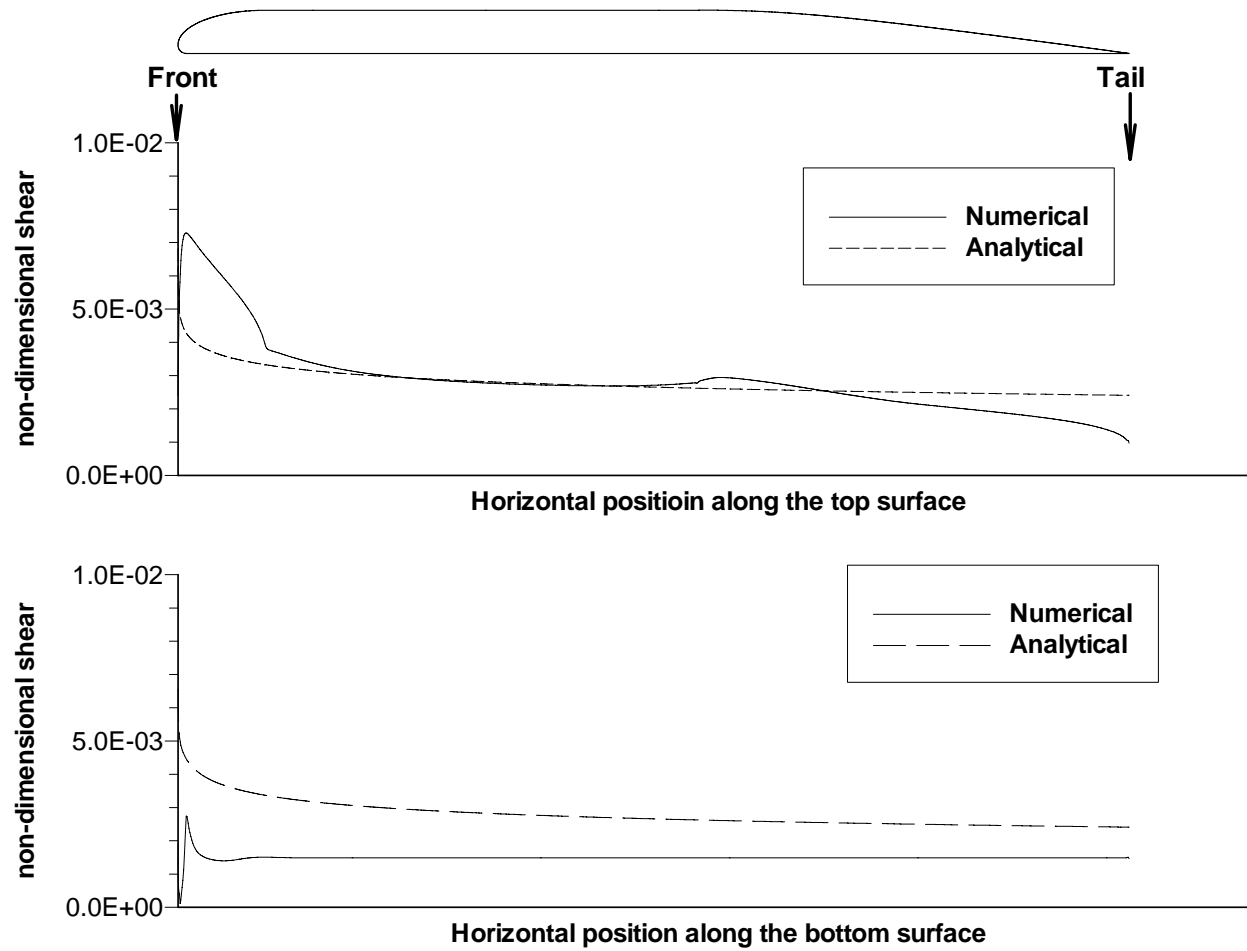


Fig. 3.22 Non-dimensional shear stress for Case 3 ($U = 1 \text{ m/s}$; $h = 0.02 \text{ m}$; $H/w = 0.5$)

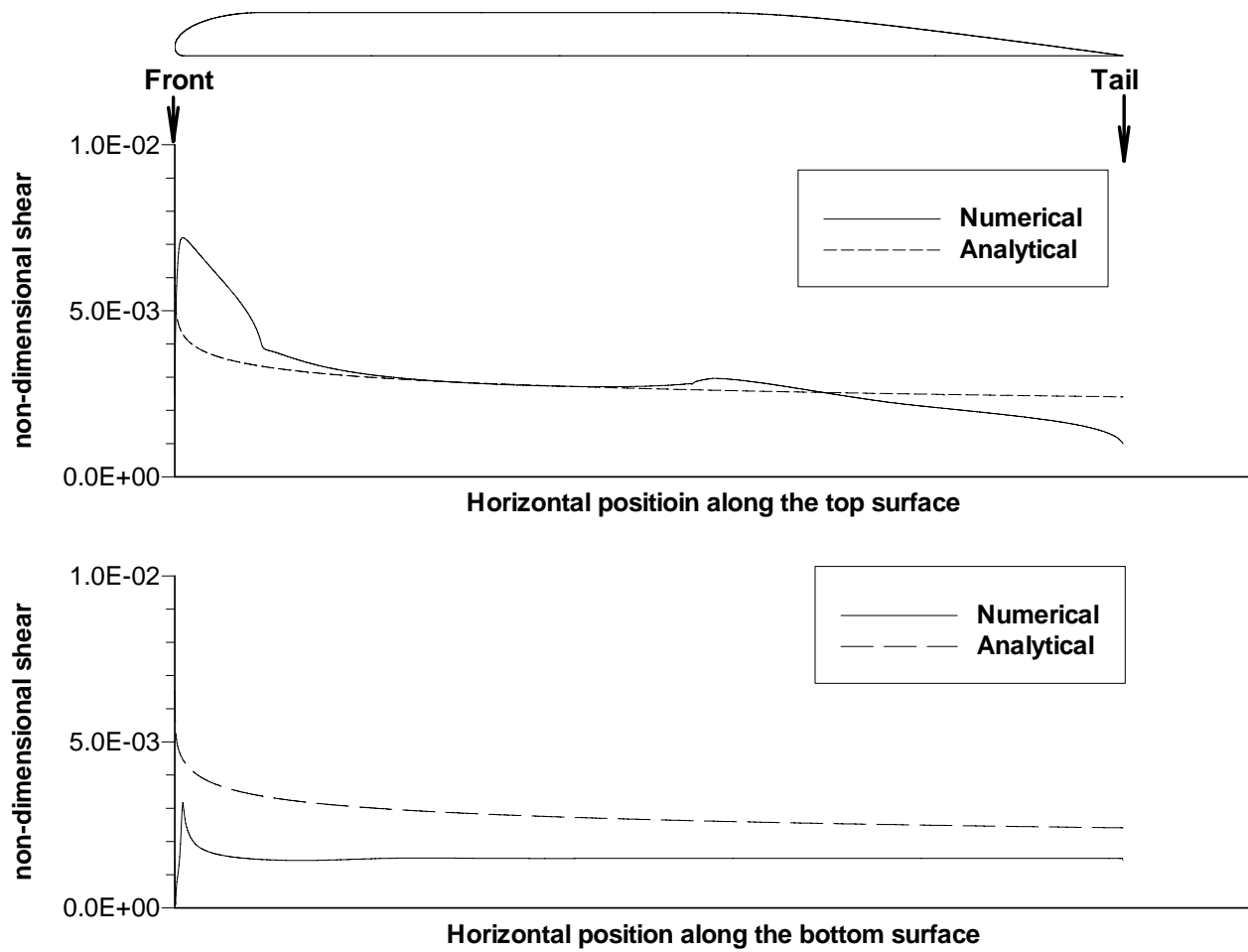


Fig. 3.23 Non-dimensional shear stress for Case 4 ($U = 1 \text{ m/s}$; $h = 0.05 \text{ m}$; $H/w = 0.5$)

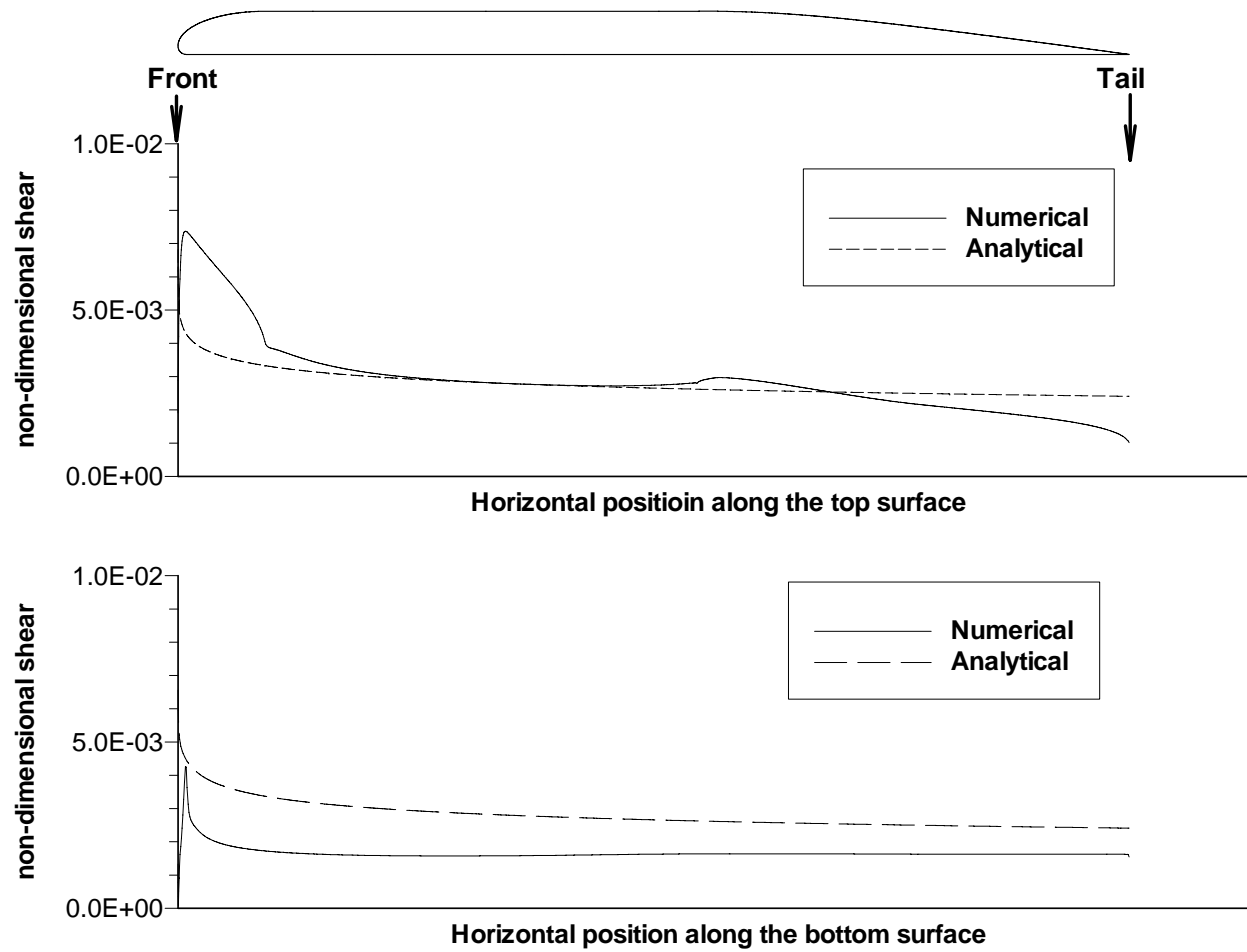


Fig. 3.24 Non-dimensional shear stress for Case 5 ($U = 1 \text{ m/s}$; $h = 0.1 \text{ m}$; $H/w = 0.5$)

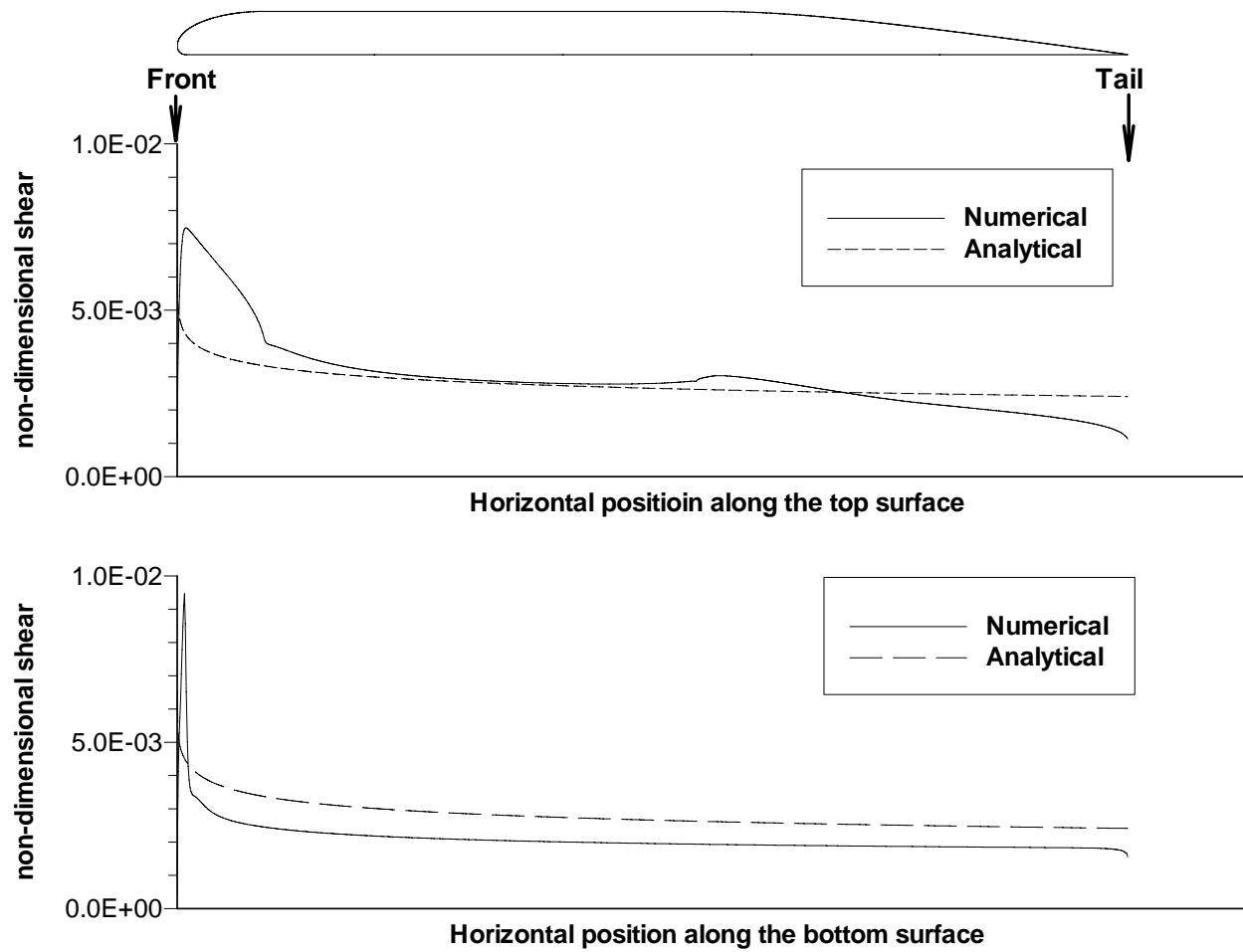


Fig. 3.25 Non-dimensional shear stress for Case 6 ($U = 1 \text{ m/s}$; $h = 1 \text{ m}$; $H/w = 0.5$)

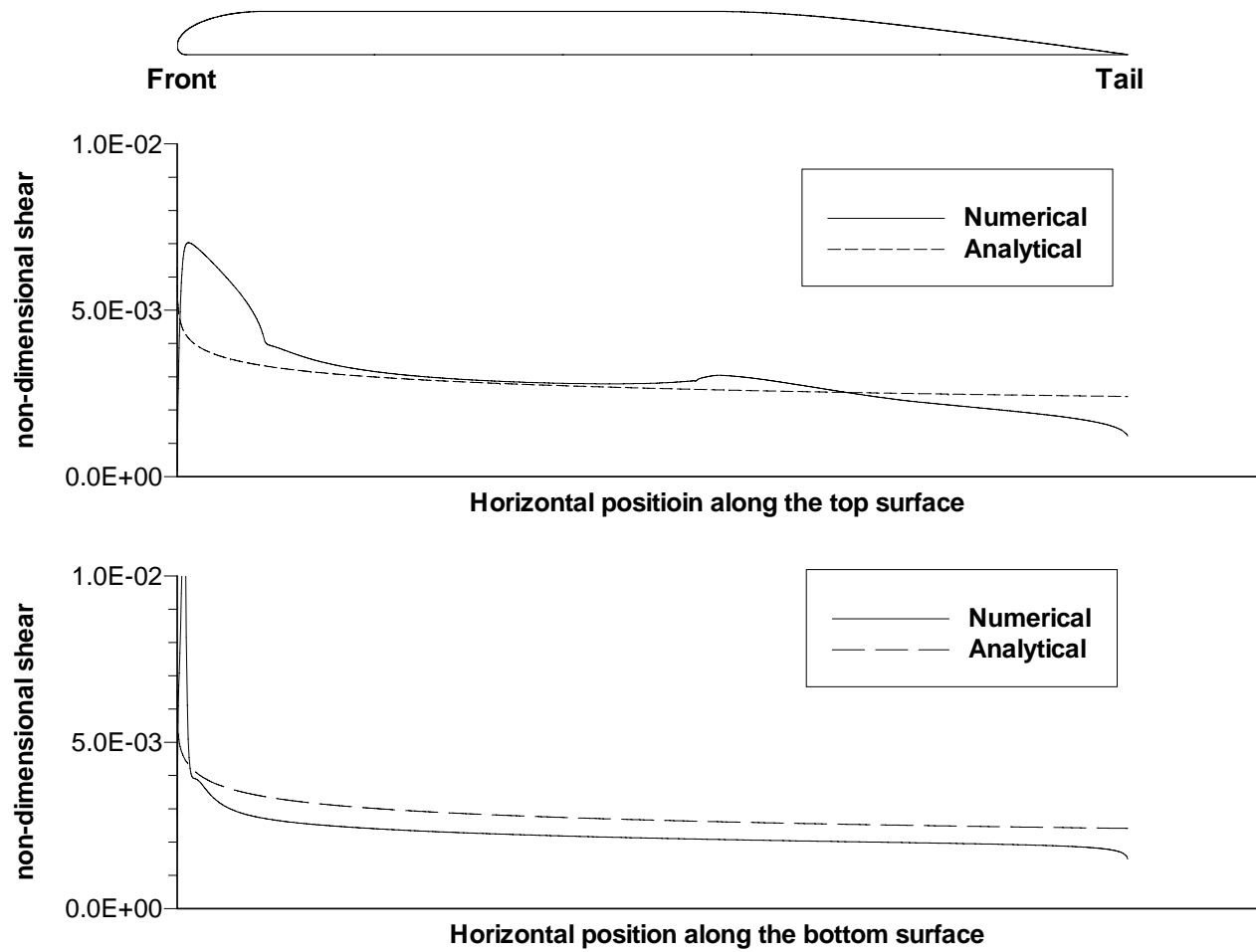


Fig. 3.26 Non-dimensional shear stress for Case 7 ($U = 1 \text{ m/s}$; $h = 10 \text{ m}$; $H/w = 0.5$)

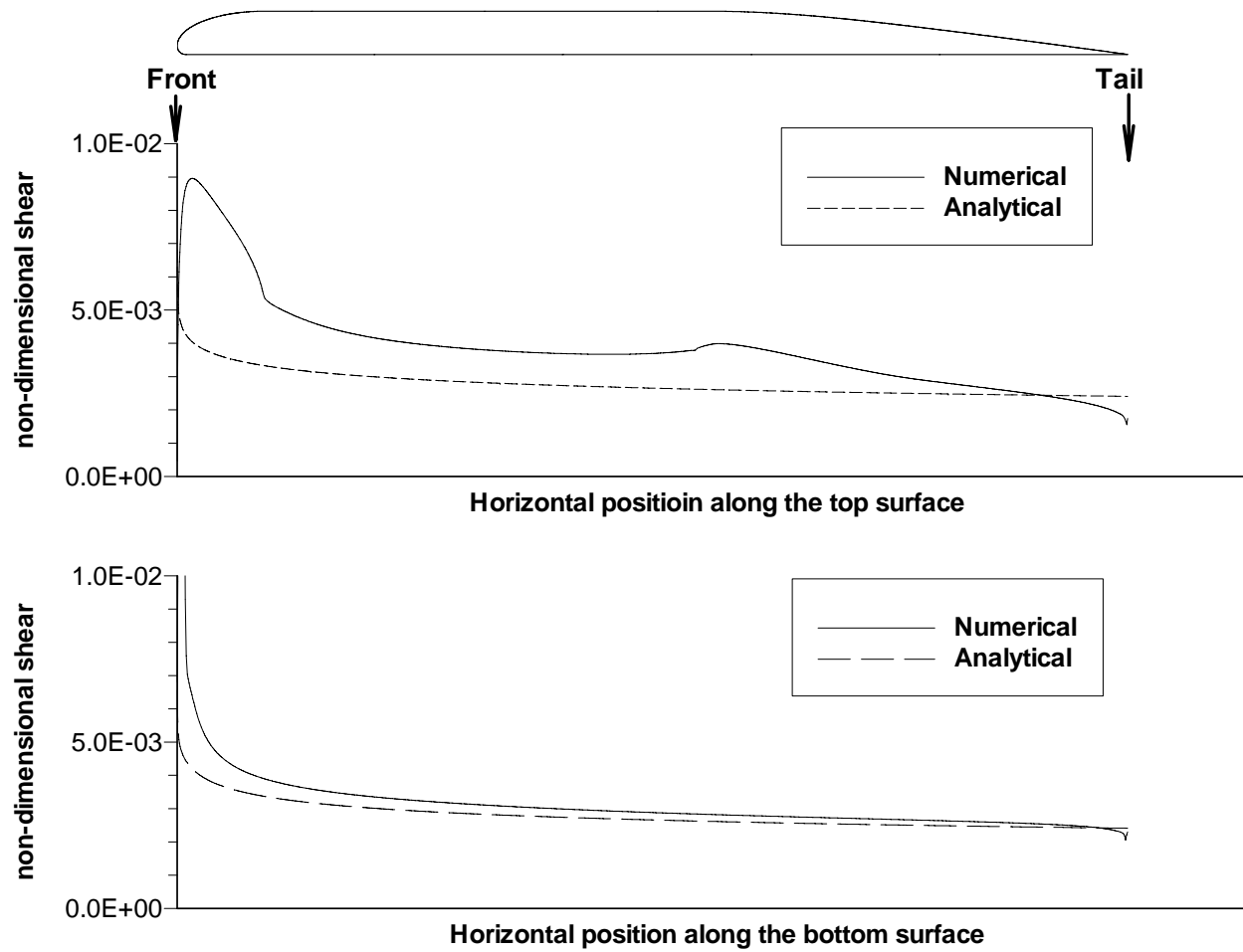


Fig. 3.27 Non-dimensional shear stress for Case 8 ($U = 1 \text{ m/s}$; $h = 50 \text{ m}$; $H/w = 0.5$)

3.3.3.3 Summary on the effect of distance h

As discussed above, a change of distance between the bottom surface of the slide mass and underlying ground h has the following effect on the hydrodynamic stresses:

1. Along the top surface of the slide mass, the non-dimensional kinetic pressures p_t / p_{stag} do not change with the distance h ;
2. Along the bottom surface of the slide mass, the non-dimensional kinetic pressures p_b / p_{stag} vary linearly beginning at a point a very short distance behind the front nose of the slide mass and ending at the tail end of the slide mass. The pressures at the beginning and end of the linear distribution can be estimated by Equation 3.3 for any distance h larger than zero;
3. Along the top and bottom surfaces of the slide mass, the non-dimensional shear stresses τ_t / p_{stag} , τ_b / p_{stag} can be approximated by Equation 3.4 for any distance h larger than zero.

3.3.4 Effect of Hydroplaning

In order to study the effect of hydroplaning on the hydrodynamic stresses, Case 9 was analyzed where the slide mass did not hydroplane. For Case 9, the bottom surface of the slide mass is in contact with the underlying ground. The geometry for Case 9 is shown in Figure 3.28. The exposed surfaces of the slide mass and the underlying ground compose the bottom of the flow domain. The boundary conditions are shown in Figure 3.29. The exposed surface of the slide mass is a stationary non-slip wall because the slide mass does not move relative to itself. The exposed surface of the underlying ground is a sliding non-slip wall because the ground moves relative to the slide mass. The mesh for Case 9 is shown in Figure 3.30 and has 553664 rectangular and triangular elements. When the slide mass does not hydroplane, the hydrodynamic stresses are only applied on the exposed surfaces of the slide mass, not on the bottom surface.

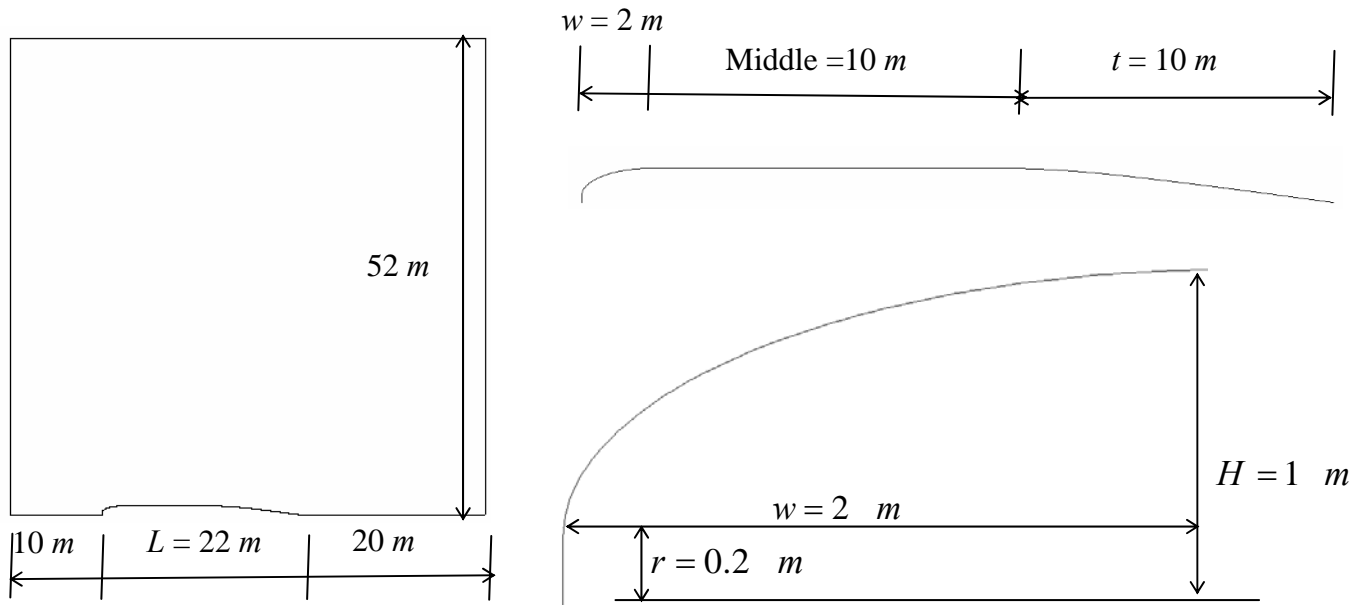


Fig. 3.28 Geometry for Case 9 ($U = 1 \text{ m/s}$; $h = 0$; $H/w = 0.5$)

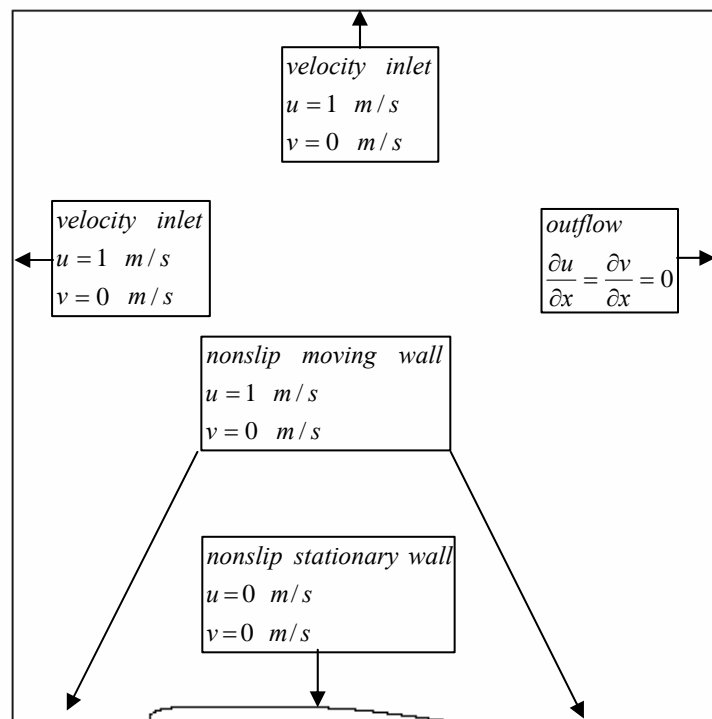


Fig. 3.29 Boundary conditions for Case 9 ($U = 1 \text{ m/s}$; $h = 0$; $H/w = 0.5$)

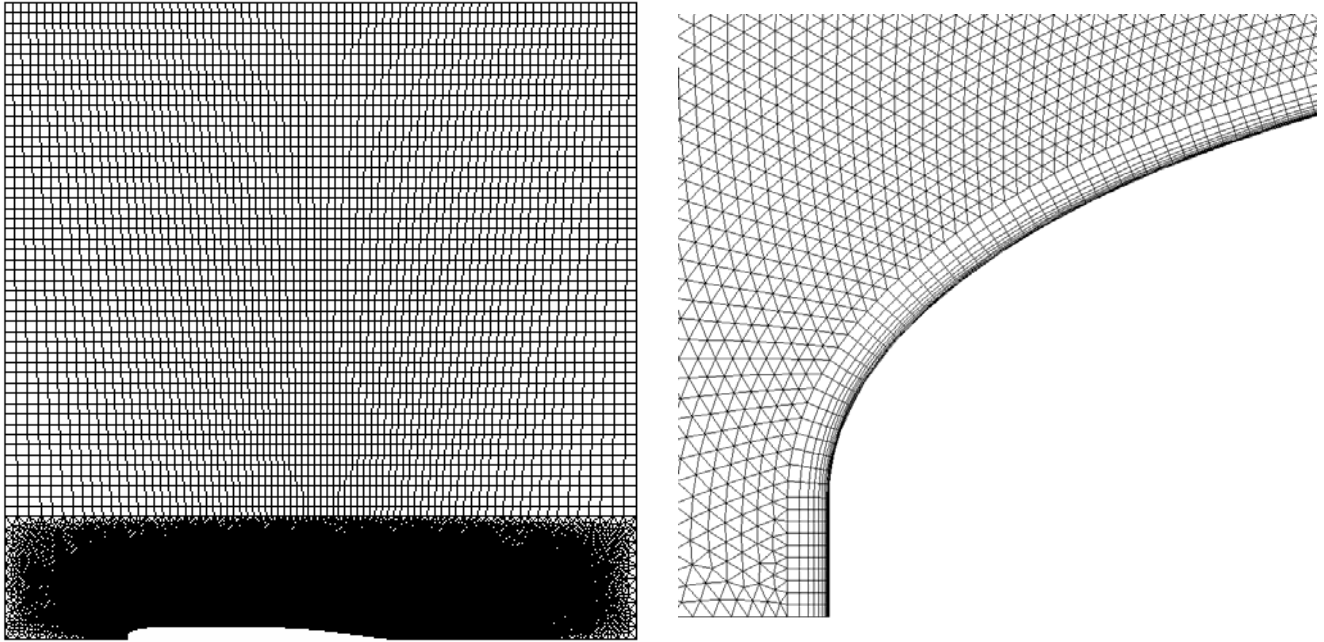


Fig. 3.30 Mesh for Case 9($U = 1 \text{ m/s}$; $h = 0$; $H/w = 0.5$)

3.3.4.1 Effect of hydroplaning on kinetic pressures

For Case 9, the pressures along the top surface of the slide mass p_t / p_{stag} are plotted in Figure 3.31. For comparison, the pressures along the top surface of the slide mass p_t / p_{stag} for Case 1 are also plotted in Figure 3.31. It can be seen that the pressures p_t / p_{stag} are so close that it is hard to distinguish the pressures for Case 1 from those for Case 9. Therefore the influence of hydroplaning on the non-dimensional kinetic pressure along the top surface of the slide mass p_t / p_{stag} is negligible.

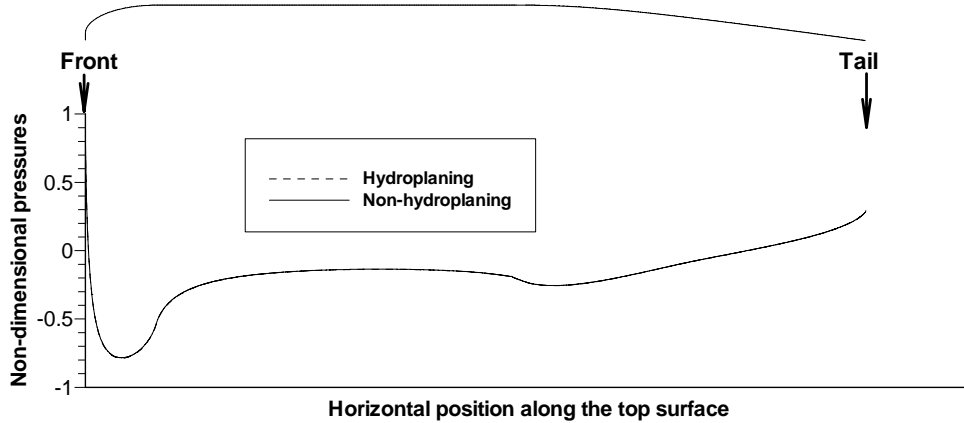


Fig. 3.31 Non-dimensional kinetic pressure for Case 9 ($U = 1 \text{ m/s}$; $h = 0$; $H/w = 0.5$)

3.3.4.2 Effect of hydroplaning on viscous shears

The non-dimensional shears along the top surface of the slide mass τ_t / p_{stag} for Case 9 are shown in Figure 3.32. The computed shears using Equation 3.4 are divided by the stagnation pressure p_{stag} and also plotted in Figure 3.32. It can be seen that the shear stresses calculated using Equation 3.4 are close to the numerical results. Therefore the analytical solution for shear stresses developed for flow above a smooth flat plate provides acceptable approximation for shear stresses on the top surface of the slide mass regardless of the occurrence of hydroplaning.

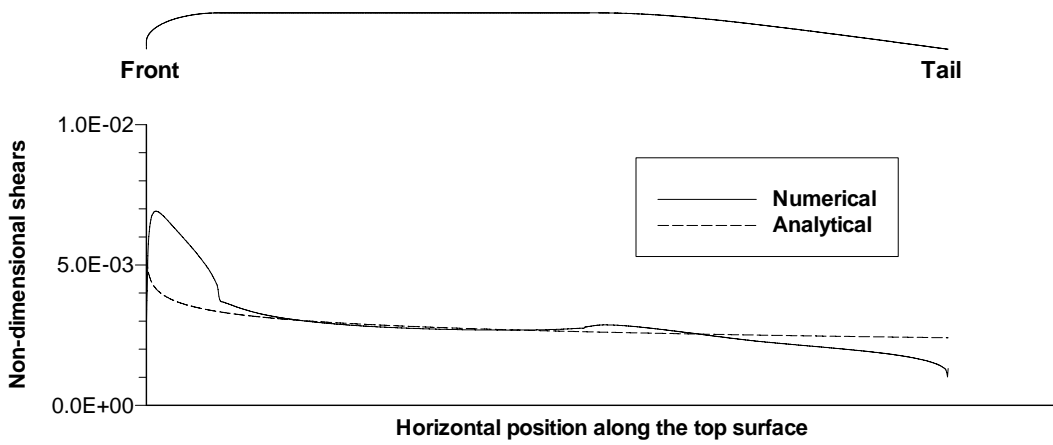


Fig. 3.32 Non-dimensional shear for Case 9 ($U = 1 \text{ m/s}$; $h = 0$; $H/w = 0.5$)

3.3.5 Effect of Height-to-Width Ratio

In order to study the influence of the ratio between the height (H) and the width of the front portion (w) of the slide mass, Case 10 was analyzed and compared with Case 9. In both Cases 9 and 10, the slide masses do not hydroplane ($h = 0$) and the inflow velocity U is 1 m/s. The only difference between Cases 9 and 10 is the height-to-width ratio H/w of the slide mass. The height-to-width ratios (H/w) for Cases 9 and 10 are 0.5 and 2.0 respectively. The front of the slide mass for Case 10 has a more abrupt curvature than that for Case 9. The geometry for Case 10 is shown in Figure 3.33. The mesh for Case 10 is shown in Figure 3.34 and includes 526722 rectangular and triangular elements.

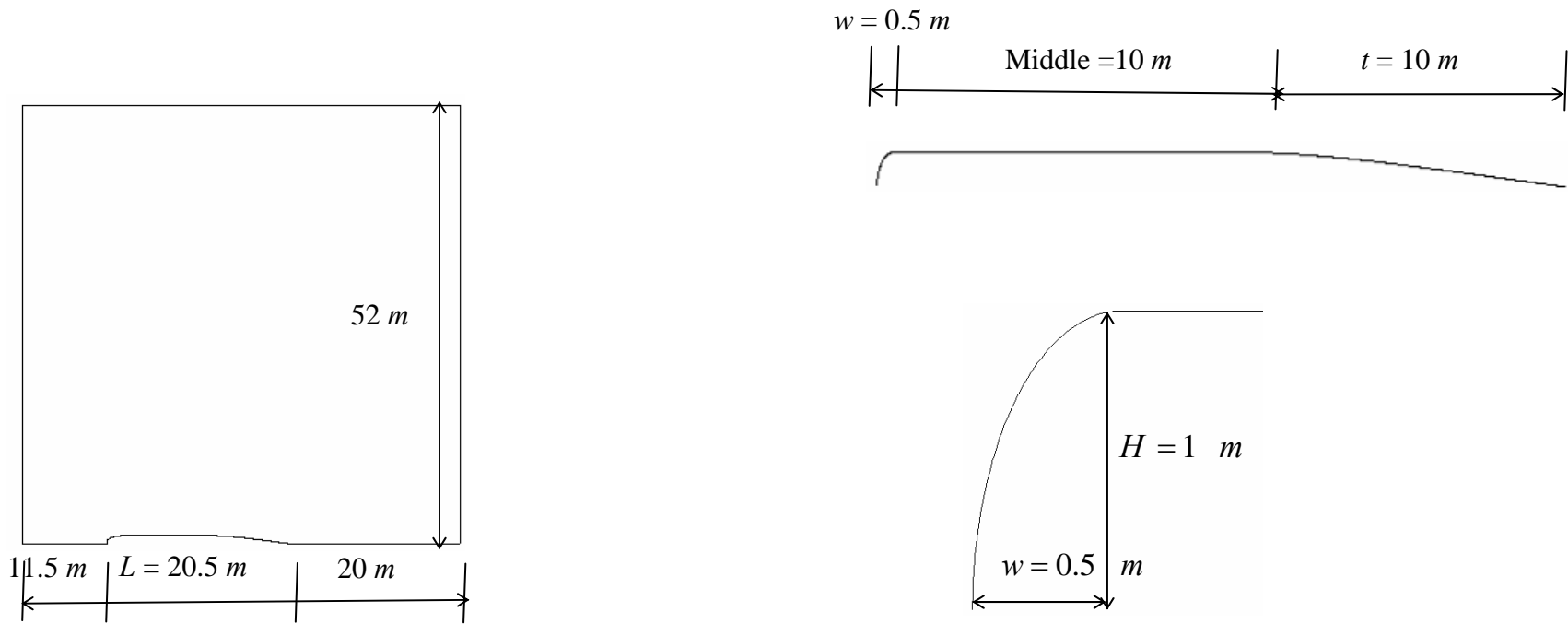


Fig. 3.33 Geometry for Case 10 ($U = 1\text{ m/s}$; $h = 0$; $H/w = 2.0$)

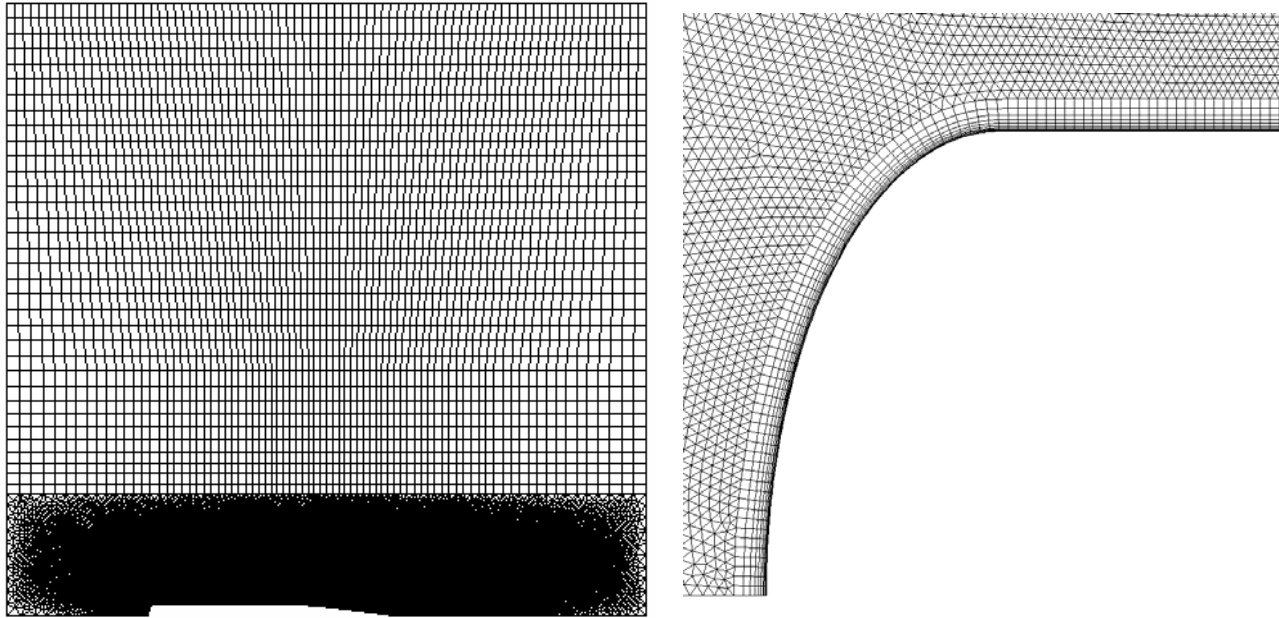


Fig. 3.34 Mesh for Case 10($U = 1$ m/s; $h = 0$; $H/w = 2.0$)

3.3.5.1 Effect of height-to-width ratio H/w on kinetic pressures

The non-dimensional kinetic pressures along the top surfaces of the slide mass p_t/p_{stag} for Cases 9 and 10 are shown in Figure 3.35. The pressures p_t/p_{stag} are similar along the middle and tail portions of the top surfaces. The non-dimensional pressures p_t/p_{stag} at the front noses of the slide masses are also similar and both equal to 1.0. However, the kinetic pressures p_t/p_{stag} along the front portion of the surfaces (from point I to point J in Figures 3.36 and 3.37) are different. The magnitude of the negative pressures on the slide mass with larger height-to-width ratio ($H/w = 2.0$ for Case 10) is much larger than that with smaller height-to-width ratio ($H/w = 0.5$ for Case 9).

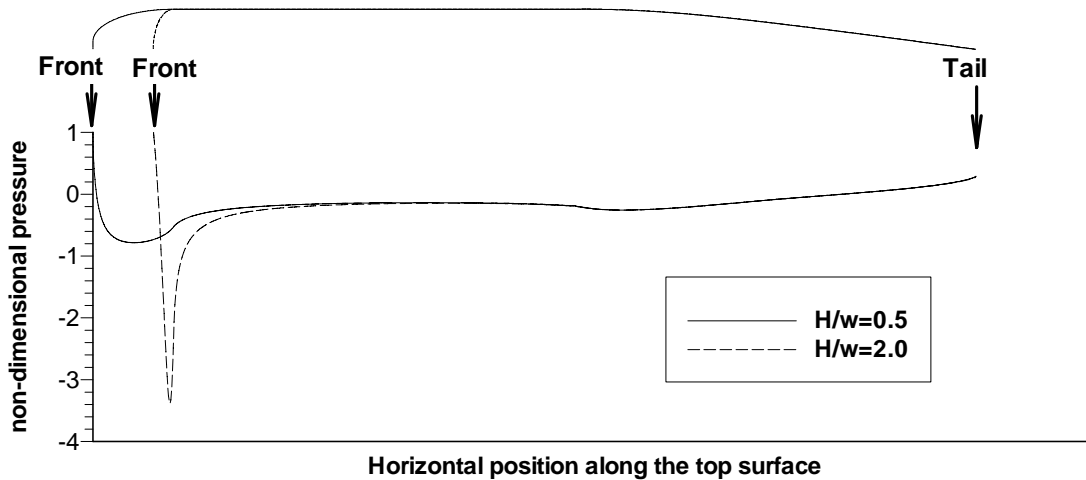


Fig. 3.35 Non-dimensional pressures for Case 9 ($U = 1 \text{ m/s}$; $h = 0$; $H/w = 0.5$) and Case 10 ($U = 1 \text{ m/s}$; $h = 0$; $H/w = 2.0$)

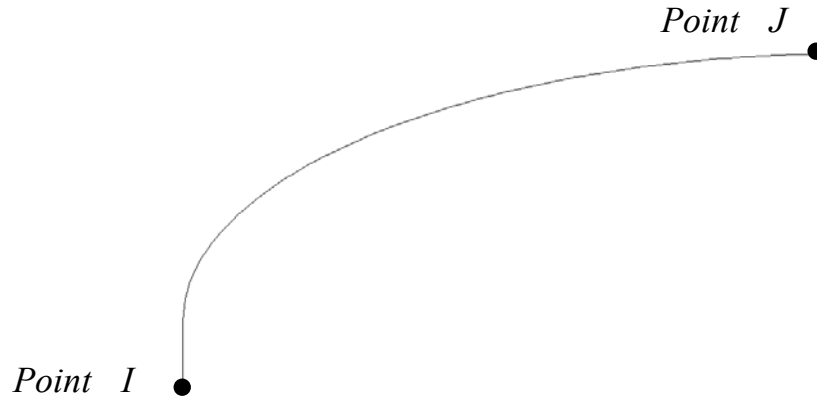


Fig. 3.36 Front portion of the surface for Case 9 ($U = 1 \text{ m/s}$; $h = 0$; $H/w = 0.5$)

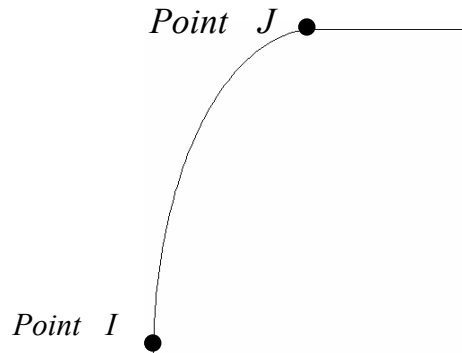


Fig. 3.37 Front portion of the surface for Case 10 ($U = 1 \text{ m/s}$; $h = 0$; $H/w = 2.0$)

3.3.5.2 Effect of height-to-width ratio H/w on the on-set condition of hydroplaning

As discussed in section 3.3.1.2, hydroplaning was expected to happen when the Froude number Fr_d was smaller than $\sqrt{2}$ after considering the negative kinetic pressure along the front portion of the surface of the slide mass (the curved portion from point I to point J shown in Figure 3.2 for Case 1, and the curved portions from point I to point J in Figures 3.36 and 3.37 for Cases 9 and 10). It has been shown in section 3.3.5.1 that the magnitude of the negative pressures on the slide mass increases as the height-to-width ratio H/w increases. Therefore the critical Froude number $Fr_{d,crit}$ for the on-set of hydroplaning should decrease with the increase of the height-to-width ratio H/w of the slide mass. The only way to determine the on-set condition of hydroplaning for a slide

mass is to analyze the dynamic response of the specific slide mass under all the appropriate stresses applied by the surrounding fluid.

3.3.5.3 Effect of height-to-width ratio H/w on viscous shears

The non-dimensional shear stresses along the top surface for Case 10 are shown in Figure 3.38. The shear stresses are also computed using Equation 3.4. After dividing by the stagnation pressure p_{stag} , the shear stresses computed using Equation 3.4 are also plotted in Figure 3.38. It can be seen that the shear stresses calculated using Equation 3.4 are similar to the shear stresses from the numerical analyses. Therefore the analytical solution for shear stresses developed for flow above a smooth flat plate provides acceptable approximation for shear stresses on the top surface of the slide mass regardless of the height-to-width ratio, H/w .

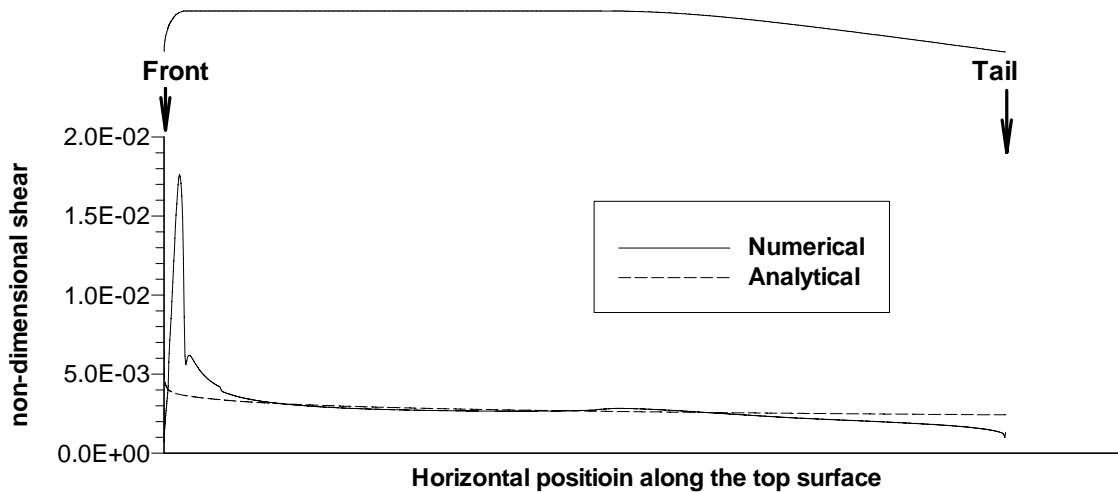


Fig. 3.38 Non-dimensional shear for Case 10 ($U = 1 \text{ m/s}$; $h = 0$; $H/w = 2.0$)

3.3.5.4 Discussions

Although the effect of height-to-width ratio H/w on hydrodynamic stresses was studied for slides that do not hydroplane, the influence of height-to-width ratio H/w for

slides that hydroplane is expected to be similar. As concluded in section 3.3.4, the effect of hydroplaning on hydrodynamic stresses along the top surface of the slide mass is negligible. Therefore the conclusions about the effect of the height-to-width ratio H/w of the slide mass on hydrodynamic stresses along the top surface of the slide mass drawn in sections 3.3.5.1 and 3.3.5.2 for slide masses that do not hydroplane can be applied to slide masses that hydroplane. Along the bottom of slide masses that hydroplane, the hydrodynamic stresses are determined by the flow between the bottom surface of the slide mass and the underlying ground. This flow and the hydrodynamic stresses along the bottom surface of the slide mass are not affected by the height-to-width ratio H/w of the slide mass.

3.4 CONCLUSIONS

A numerical model was developed and used to study the flow around a moving slide mass. The study has produced a better understanding of the flow around the slide mass especially of the resulting pressures and shear stresses exerted on the mass. The following conclusions can be drawn from the numerical modeling:

1. When normalized by the stagnation pressure p_{stag} , the non-dimensional kinetic pressures on the surfaces of the slide mass are not influenced by the magnitude of the inflow velocity;
2. Along the top surface of the slide mass, hydrodynamic stresses are not influenced by the onset of hydroplaning or the distance between the underlying ground and the bottom surface of the slide mass that hydroplanes;
3. The kinetic pressures on the middle portion of the top surface of the slide mass are essentially zero for slides in deep water;

4. The non-dimensional kinetic pressures on the tail portion of the top surface of the slide mass increases linearly from zero at the beginning of the tail portion of the slide mass to 0.3 at the end of the slide mass;
5. The kinetic pressure is negative along the frontal portion of the top surface of the slide mass and provides a lift on the slide mass. The magnitude of this negative pressure increases as the height-to-width ratio of the slide mass increases;
6. Along the bottom surface of slide mass that hydroplanes, the non-dimensional kinetic pressures vary linearly beginning at a point a very short distance behind the front nose of the slide mass and extending to the tail end of the slide mass. The pressures at the point a very short distance behind the front nose and at the tail end of the slide mass can be estimated using Equation 3.3;
7. The shear stress along the top and bottom surfaces of the slide mass can be estimated using Equation 3.4;

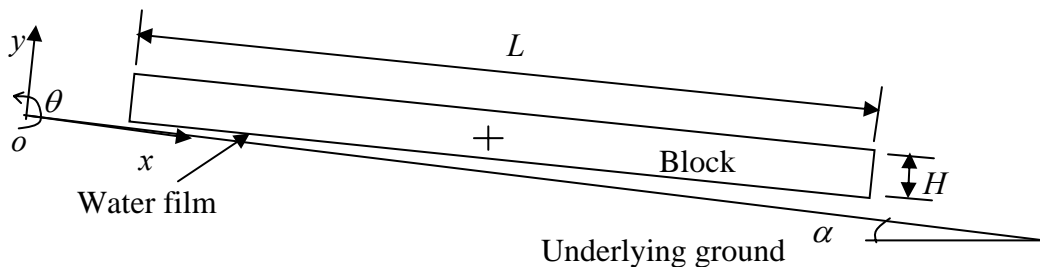
Conclusion 5 explains why a slide mass hydroplanes when the Froude number Fr_d is smaller than $\sqrt{2}$ and suggests that the dynamic response of a specific slide mass under all the appropriate stresses applied by the surrounding fluid needs to be analyzed in order to determine the on-set condition of hydroplaning for the slide mass. A block model is developed in the next chapter to simulate the dynamic response of a slide mass and all the above conclusions derived for the hydrodynamic stresses on the slide mass are applied as stress boundary conditions for the block model. In this block model, the hydrodynamic stresses on the surfaces of the block are estimated based on conclusions 1 to 7 and applied as external stresses on the block. Further details of how the stresses are estimated and applied in the block model are discussed in the following chapter.

Chapter 4: Development of Block Model for Subaqueous Slides involving Hydroplaning

A block model was developed to simulate the sliding process of submarine slides. The results of the numerical modeling of hydrodynamic stresses described in the previous chapter were used to establish the boundary conditions for the sliding block. The block model, including its implementation in a computer code written in the C programming language, is discussed in this chapter.

4.1 GOVERNING EQUATIONS OF MOTION

In the block model, the slide mass is represented as a rigid rectangular block which moves and rotates in the plane $x-o-y$ as shown in Figure 4.1. No change in total volume of the slide mass is assumed during the process of sliding because sliding usually lasts no longer than several minutes and the slide mass of interest usually consists of saturated fine-grained soil particles with very low permeability. Thus there is negligible drainage of water into or out of the soil mass during sliding.



Note: The cross marks the center of the block.

Fig. 4.1 Geometry and coordinate system for the block model

Movement of the block involves three degrees of freedom. The block can translate in the x and y directions and rotate in the $x-o-y$ plane. The translations of

the center of the block (marked by a cross in Figure 4.1) and the rotation of the block relative to the center are computed from the following governing equations:

$$\ddot{x} = \frac{F_x}{M} \quad (4.1)$$

$$\ddot{y} = \frac{F_y}{M} \quad (4.2)$$

$$\ddot{\theta} = \frac{T}{I} \quad (4.3)$$

where \ddot{x} , \ddot{y} are the accelerations in the x and y directions; F_x , F_y are the total external forces on the block in the x and y directions; $\ddot{\theta}$ is the angular acceleration in the $x-o-y$ plane and T is the total external torque about the center of the block in the θ direction. The quantity M in Equations (4.1) and (4.2) is the mass of the block and can be calculated as:

$$M = \rho_s HL \quad (4.4)$$

The quantity I in Equation (4.3) is the moment of inertia about the center of the block and can be calculated as:

$$I = \frac{1}{12} \rho_s HL (H^2 + L^2) \quad (4.5)$$

where ρ_s is the total mass density of the soil, H is the height of the block and L is the length of the block.

4.2 OCCURRENCE OF HYDROPLANING

The occurrence of hydroplaning depends on the contact condition between the bottom surface of the block and the underlying ground. In order to determine the contact condition, the height of roughness h_r at the interface between the block and underlying ground is compared with the displacement of the block in the y direction along the bottom surface.

The height of roughness h_r is a small-scale variation in the height of physical surfaces. At the interface between the block and underlying ground, it is determined by

the size of soil particles in the block and the surface property of the underlying ground. For underlying ground consisting of soil particles, the height of roughness h_r is assumed to be d_{95} of the soil in the block and ground.

The displacement of the block in the y direction may change along the x direction. At the front and tail ends of the block, the displacements are designated as h_f and h_t respectively as shown in Figure 4.2. The displacements h_f and h_t can be calculated as:

$$h_f = y - \frac{1}{2}H + \frac{1}{2}L \sin \theta \quad (4.6)$$

$$h_t = y - \frac{1}{2}H - \frac{1}{2}L \sin \theta \quad (4.7)$$

where y is coordinate of the center of the block in the direction normal to the underlying ground, H is the height of the block, L is the length of the block and θ is the angle between the bottom of the block and underlying ground.

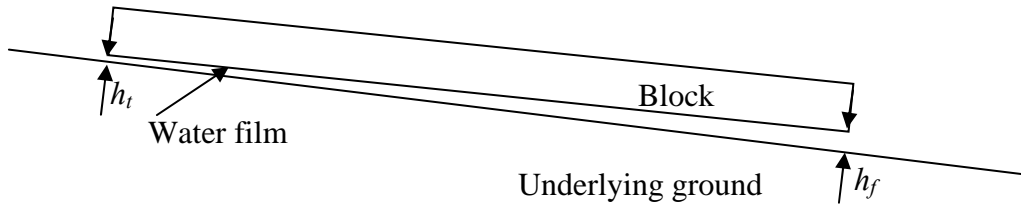


Fig. 4.2 Distance between the block and underlying ground

Three possible contact conditions are defined by comparing the displacements h_f , h_t and the height of roughness h_r as follows:

- 1) No hydroplaning: The bottom surface of the block is in contact with the underlying ground everywhere, i.e.

$$\max(h_f, h_t) \leq h_r \quad (4.8)$$

- 2) Partial hydroplaning: Part of the bottom surface is in contact with the ground and the other part is not, i.e.

$$\min(h_f, h_t) \leq h_r \leq \max(h_f, h_t) \quad (4.9)$$

- 3) Complete hydroplaning: No part of the bottom surface of the block is in contact with the ground surface, i.e.

$$h_r \leq \min(h_f, h_t) \quad (4.10)$$

The forces applied on the bottom surface of the block change with the occurrence of hydroplaning. The stresses on the bottom of the block for the above three conditions are discussed in the following section.

4.3 FORCES ON BLOCK

The external forces on the block represent the forces due to the effective gravitational force, reactive forces applied on the bottom of the block by the underlying ground, and the hydrodynamic stresses applied on the surfaces of the block by the surrounding fluid. The potential stresses and forces on the block are summarized in Table 4.1 and also illustrated in Figure 4.3. The stresses and forces on the block are discussed as in the sections below.

Table 4.1. Possible stresses on the block

Stress	Symbol	No Hydroplaning	Partial Hydroplaning	Complete Hydroplaning
Effective gravitational force at the center of the block	G'	Applied		
Kinetic pressure on the leading edge	p_u	Applied		
Kinetic pressure on the tail surface	p_d	Applied	Applied	Applied
Kinetic pressure on the top surface	p_t	Applied		
Kinetic pressure on the bottom surface (pore water pressure on the bottom surface) due to movement down slope	p_b	Applied as pore water pressure	Applied as kinetic pressure	Applied as kinetic pressure
Kinetic damping force	\tilde{N}_w	Not applied	Applied	Applied
Kinetic damping moment	M_w	Not applied	Applied	Applied
Viscous shear along the leading edge	τ_u	Applied		
Viscous shear along the tail surface	τ_d	Applied	Applied	Applied
Viscous shear along the top surface	τ_t	Applied		
Viscous shear along the bottom surface	τ_b	Not applied	Not applied	Applied
Effective support on the bottom surface applied by the ground surface	N'_{bu}, N'_{bd}	Applied		
Damping force applied by the ground surface	D_{sd}, D_{su}	Applied		
Friction on the bottom surface	c	Applied	Not applied	Not applied

4.3.1 Effective Weight

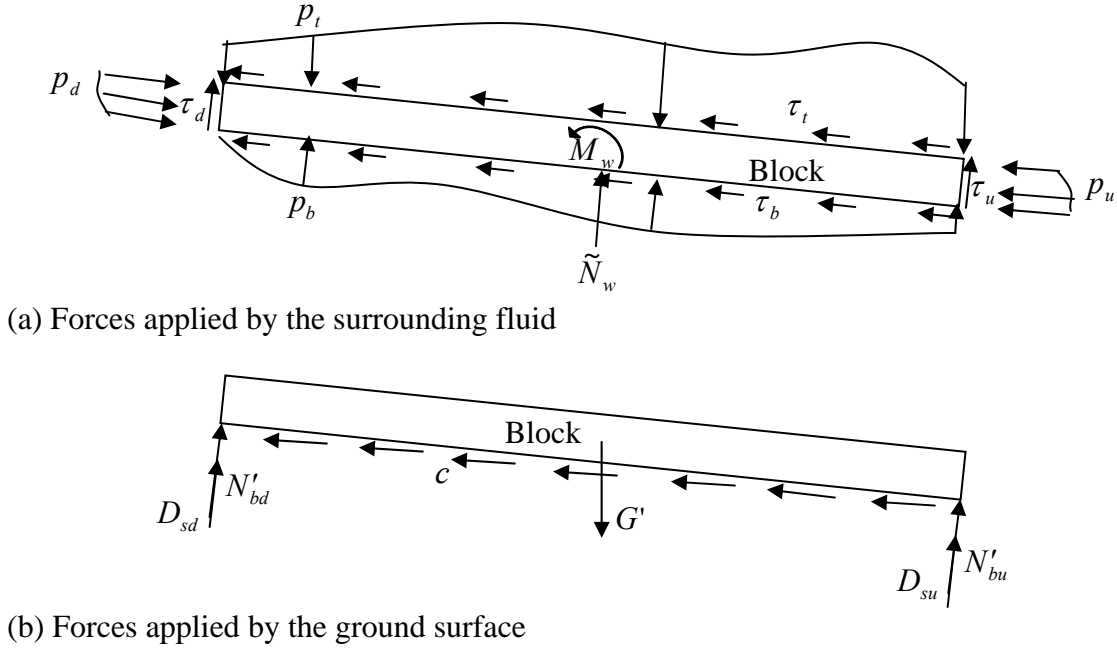


Fig. 4.3 Forces on the block

The effective weight of the block G' is calculated as:

$$G' = (\rho_s - \rho_w)gHL \quad (4.11)$$

where ρ_s is the total density of soil, ρ_w is the density of water, g is the acceleration of gravity, H is the height of the block and L is the length of the block. The force due to the effective weight G' acts through the centroid of the block as shown in Figure 4.3 (b).

4.3.2 Kinetic Pressure

Surrounding fluid applies hydrodynamic stresses on the surface of the block when the block moves. The two types of hydrodynamic stress are kinetic pressure and viscous shear. The kinetic pressures caused by the motion of the block in the x direction include the pressures on all four surfaces of the block, p_u , p_d , p_t and p_b as shown in Figure 4.3 (a). These kinetic pressures are determined based on the numerical modeling of flow around a sliding mass that was discussed in the previous chapter. In order to better explain the kinetic pressures, a local reference system $r-s$ as shown in Figure 4.4 is used.

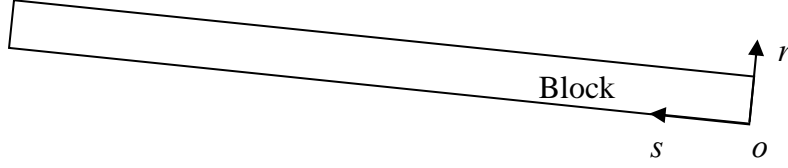


Fig. 4.4 Local coordinate system for the block model

4.3.2.1 Along the leading edge

The kinetic pressure on the leading edge of the block p_u as in Figure 4.3 (a) varies linearly from the stagnation pressure $\frac{1}{2}\rho_w V_x^2$ at $r = 0$ to zero at $r = \alpha H$, where α is the head ratio of the block defined as the ratio of block's height at the front to the average height of the block H . The head ratio α is a non-dimensional constant and is used to consider the effect of the frontal shape on the kinetic pressure p_u . The kinetic pressure p_u can be calculated as:

$$p_u = \frac{1}{2}\rho_w V_x^2 \left(1 - \frac{r}{\alpha H}\right) \quad (4.12)$$

where ρ_w is the density of water, V_x is the velocity of the block in the x direction, r is the local coordinate along the front surface of the block and H is the height of the block.

4.3.2.2 Along the trailing edge

The kinetic pressure along the trailing surface of the block p_d as in Figure 4.3 (a) is assumed to vary linearly in the r direction from zero at $r = H$ to $0.3p_{stag}$ at $r = 0$. The kinetic pressure p_d are calculated as:

$$p_d = 0.3 \left(\frac{1}{2}\rho_w V_x^2\right) \left(1 - \frac{r}{H}\right) \quad (4.13)$$

4.3.2.3 Along the top surface

The kinetic pressure along the top surface of the block p_t as shown in Figure 4.3 (a) is assumed to vary linearly in three ranges. The distribution of kinetic pressure p_t is

shown in Figure 4.5. Along the s direction, the kinetic pressure p_t varies linearly from zero at $s = 0$ to $\lambda \frac{1}{2} \rho_w V_x^2$ at $s = \frac{1}{2} \beta H$, then to zero at $s = \beta H$, and then to zero at $s = L$. The constant β is the ratio of the length where negative kinetic pressure is applied to the height of the block. The constant λ is the ratio of the lowest pressure along the top surface to the stagnation pressure. The kinetic pressure p_t is calculated as:

$$p_t = \begin{cases} \lambda \frac{1}{2} \rho_w V_x^2 \frac{s}{0.5\beta H} & 0 \leq s \leq \frac{1}{2} \beta H \\ \lambda \frac{1}{2} \rho_w V_x^2 \left(2 - \frac{s}{0.5\beta H} \right) & \frac{1}{2} \beta H \leq s \leq \beta H \\ 0 & \beta H \leq s \leq L \end{cases} \quad (4.14)$$

where s is the local coordinate along the top surface of the block as shown in Figure 4.3, and L is the length of the block.

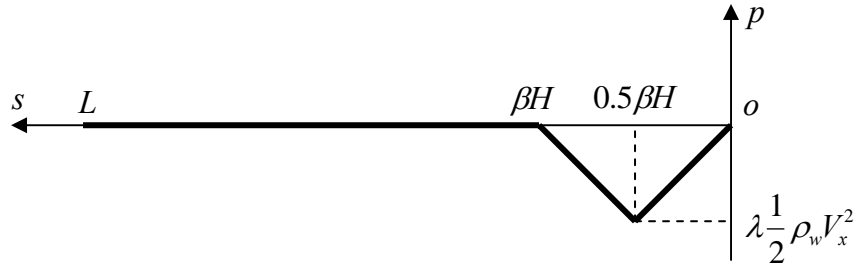


Fig. 4.5 The distribution of pressure p_t along the top surface of the block

4.3.2.4 Along the bottom surface

The pressure along the bottom surface of the block p_b is influenced by the occurrence of hydroplaning. As discussed in section 4.2, three conditions are possible. The pressures for the three conditions are as follows:

- 1) No hydroplaning: Excess pore water pressure is applied along the bottom surface.

The pressure p_b is assumed to be uniform and can be calculated as:

$$p_b = \frac{1}{2} \rho_w V_x^2 \quad (4.15)$$

where ρ_w is the density of water, V_x is the velocity of the block in the x direction;

- 2) Partial hydroplaning: Excess pore water pressure is applied on the non-hydroplaning part of the bottom surface; the kinetic pressure is applied on the hydroplaning part of the bottom surface. The bottom pressure p_b is assumed to be uniform and determined by Equation 3.3. The pressure p_b is calculated as:

$$p_b = \begin{cases} \left[\frac{1}{2} \rho_w V_x^2 \frac{1}{1 + 2.57 \left(\frac{h_f}{H} \right)^{0.58}} \right] & \text{for } h_f \geq h_t \\ \left[\frac{1}{2} \rho_w V_x^2 \frac{0.3}{1 + 0.15 \left(\frac{h_t}{H} \right)^{0.4}} \right] & \text{for } h_t \geq h_f \end{cases} \quad (4.16)$$

where H is the height of the block, h_f is the distance from the front end of the block to the underlying ground and h_t is the distance from the tail end of the block to the underlying ground;

- 3) Complete hydroplaning: Kinetic pressure is applied on the entire bottom surface of the block. Along the s direction, the pressure p_b is assumed to vary linearly. Based on Equation 3.3, the bounding values for the pressure p_b are

$$\frac{1}{2} \rho_w V_x^2 \left[\frac{1}{1 + 2.57 \left(\frac{h_f}{H} \right)^{0.58}} \right] \text{ at } s = 0 \text{ and } \frac{1}{2} \rho_w V_x^2 \left[\frac{0.3}{1 + 0.15 \left(\frac{h_t}{H} \right)^{0.4}} \right] \text{ at } s = L. \text{ The}$$

pressure p_b can be calculated as:

$$p_b = \frac{1}{2} \rho_w V_x^2 \times \left\{ \left[\frac{1}{1 + 2.57 \left(\frac{h_f}{H} \right)^{0.58}} \left(1 - \frac{s}{L} \right) + \left[\frac{0.3}{1 + 0.15 \left(\frac{h_t}{H} \right)^{0.4}} \right] \left(\frac{s}{L} \right) \right] \right\} \quad (4.17)$$

4.3.3 Viscous Shear

The viscous shears caused by the motion of the block in the x direction include τ_u , τ_d , τ_t and τ_b as shown in Figure 4.3 (a). Shear stresses along the leading and trailing (front and tail) surfaces of the block τ_u, τ_d are neglected. The shear stress along the bottom of the slide mass τ_b is only applied when complete hydroplaning occurs as discussed in section 4.2. Along the top and bottom surfaces of the block, shear stress τ_t and τ_b are estimated by the theory for a turbulent boundary layer along a flat plate as

$$\tau_t = \tau_b = \frac{1}{2} \rho_w V_x^2 \left(\frac{0.027}{\left(\frac{V_x s}{\nu} \right)^{1/7}} \right) \quad (4.18)$$

where ν is the kinematic viscosity of water. More details about the theory for turbulent boundary layers can be found in Crowe, et al. (2000).

4.3.4 Support by Underlying Ground

When the block is in contact with the underlying ground, a positive effective normal stress may be applied at the bottom surface of the block by the underlying ground. For simplicity, the effective normal stresses are simulated by two springs. The springs are assumed to produce the same total normal force and moment as produced by the normal stresses in the soil distributed along the bottom of the block. As shown in Figure 4.6, the two springs connect the lower corners of the block to the underlying ground. The forces produced by the springs on the block are designed as N'_{bu} and N'_{bd} respectively for the front and trailing corners.

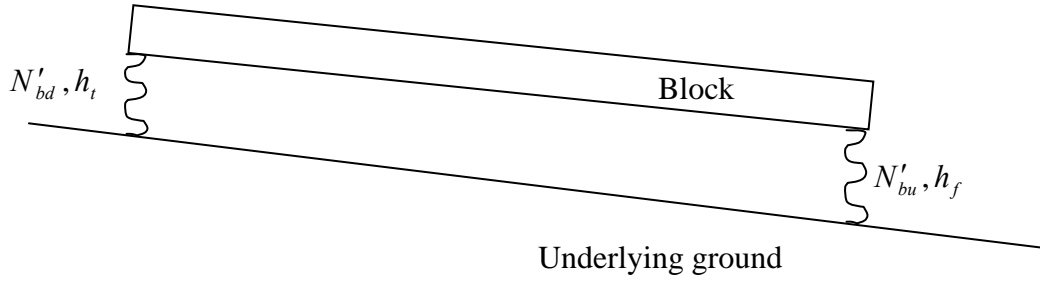


Fig. 4.6 Springs between the block and underlying ground

The forces N'_{bu} and N'_{bd} depend on the displacements of the block at the front and trailing corners h_f and h_t respectively. The force-displacement curve of the springs ($N'_{bu} - h_f$ and $N'_{bd} - h_t$) is shown in Figure 4.7.

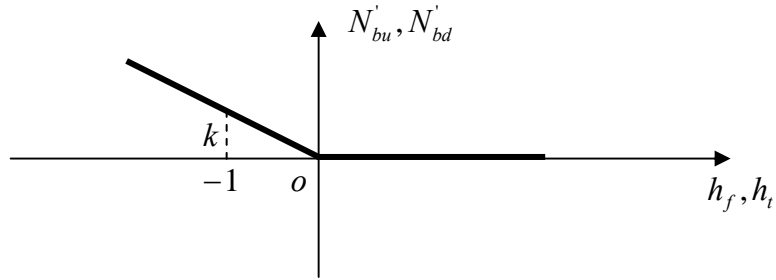


Fig. 4.7 Force-displacement curve of the springs

As shown in Figure 4.7, the tensile strength of the springs is zero. When compressed, the springs are linearly elastic. The forces applied by the springs N'_{bu} and N'_{bd} are zero when displacements h_f and h_t are positive. When the displacements h_f and h_t are negative, the forces N'_{bu} and N'_{bd} can be calculated as:

$$N'_{bu} = \begin{cases} 0 & h_f \geq 0 \\ -kh_f & h_f < 0 \end{cases} \quad (4.19)$$

$$N'_{bd} = \begin{cases} 0 & h_t \geq 0 \\ -kh_t & h_t < 0 \end{cases} \quad (4.20)$$

where k is a spring constant. The constant k is determined based on the settlement at the surface of an elastic ground under a rectangular footing (Das, 1999) as follows:

$$k = \frac{E}{1-\nu^2} \frac{1}{10} \quad (4.21)$$

Where E is the modulus of elasticity and ν is the Poisson's ratio for the underlying soil. The parameters E and ν are parameters defined in terms of effective stresses of the soil.

4.3.5 Resistance by Underlying Ground

When the block is in contact with the underlying ground, a shear stress is applied on the bottom of the block. The stress is assumed to be equal to the un-drained shear strength (c) of soil at the interface for no hydroplaning condition. For partial and complete hydroplaning conditions, the stress is assumed to be zero. The un-drained shear strength c is calculated as

$$c = \tau_y + \mu_s \frac{\dot{x}}{\left(\frac{H}{2}\right)} \quad (4.22)$$

where τ_y is the static shear strength of soil corresponding to infinitely low strain rate, \dot{x} is the slide velocity of the block, H is the height of the block and μ_s is a constant. The second term in Equation 4.22 represents the influence of strain rate on the shear strength of soil c . The strain rate at the bottom surface of the block is assumed to be $\dot{x}/\left(\frac{H}{2}\right)$.

4.3.6 Damping Effect

Two types of damping effects are considered in the block model. One is referred to as kinetic damping which is applied by the surrounding water. The other is soil damping which is applied by the underlying ground. The damping forces are discussed as follows.

4.3.6.1 Kinetic damping

Kinetic damping is produced by the hydrodynamic stresses due to the block's motion in the y direction and rotation in the $x-o-y$ plane. These hydrodynamic

stresses are shown in Figure 4.8. Compared with the kinetic pressure along the bottom surface of the block \tilde{p}_b , the other hydrodynamic stresses are negligible. The kinetic pressure \tilde{p}_b is only applied after the block reaches the complete hydroplaning condition.

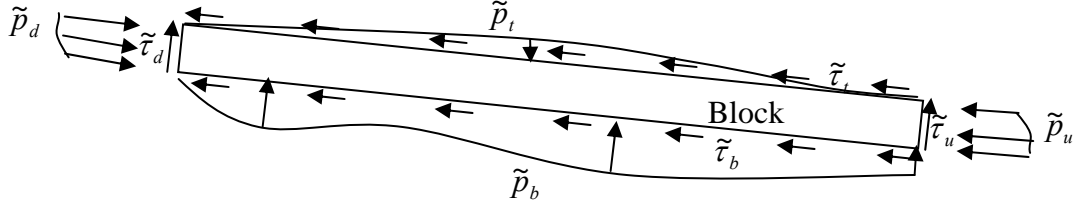


Fig. 4.8 Hydrodynamic stresses producing kinetic damping effect

When the bottom surface of the block is parallel to the underlying ground, i.e. $h_f = h_t$ and $\theta = 0$, the kinetic pressure \tilde{p}_b can be estimated analytically. According to the analytical solution for squeeze film lubrication (Panton, 1984), the kinetic pressure \tilde{p}_b can be expressed as:

$$\tilde{p}_b = \begin{cases} 6 \frac{\mu L^2}{h_f^3} \dot{y} \left[\frac{s}{L} \left(\frac{s}{L} - 1 \right) \right] = 6 \frac{\mu L^2}{h_t^3} \dot{y} \left[\frac{s}{L} \left(\frac{s}{L} - 1 \right) \right] & \text{for } h_f = h_t > h_r \\ 6 \frac{\mu L^2}{h_r^3} \dot{y} \left[\frac{s}{L} \left(\frac{s}{L} - 1 \right) \right] & \text{for } h_f = h_t \leq h_r \end{cases} \quad (4.23)$$

The distribution of kinetic pressure \tilde{p}_b is also plotted in Figure 4.9. As shown in Figure 4.9, the pressure \tilde{p}_b is symmetric about the midpoint of the bottom surface ($x = L/2$).

The peak value of pressure \tilde{p}_b is $-\frac{3}{2} \frac{\mu L^3}{\max(h_f, h_r)^3} \dot{y}$ at the midpoint of the bottom surface, i.e. $x = L/2$. The integration of pressure \tilde{p}_b along the bottom surface of the block yields the total normal force on the bottom surface \tilde{N}_w as:

$$\tilde{N}_w = \int_0^L \tilde{p}_b ds = \begin{cases} \int_0^L 6 \frac{\mu L^2}{h_f^3} \dot{y} \left[\frac{s}{L} \left(\frac{s}{L} - 1 \right) \right] ds & \text{for } h_f = h_t > h_r \\ \int_0^L 6 \frac{\mu L^2}{h_r^3} \dot{y} \left[\frac{s}{L} \left(\frac{s}{L} - 1 \right) \right] ds & \text{for } h_f = h_t \leq h_r \end{cases} \quad (4.24)$$

$$= \begin{cases} -\frac{\mu L^3}{h_f^3} \dot{y} = -\frac{\mu L^3}{h_t^3} \dot{y} & \text{for } h_f = h_t > h_r \\ -\frac{\mu L^3}{h_r^3} \dot{y} & \text{for } h_f = h_t \leq h_r \end{cases}$$

The moment M_w about the center of the block produced by the kinetic pressure \tilde{p}_b is zero.

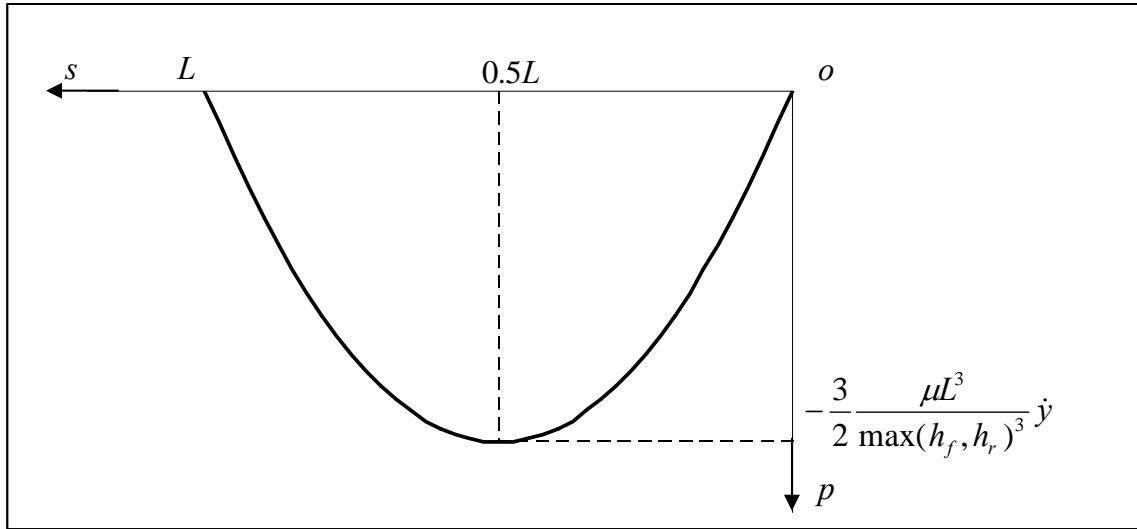


Fig. 4.9 Kinetic pressure \tilde{p}_b for $h_f = h_t$ and $\theta = 0$

When the bottom surface of the block is not parallel to the underlying ground, i.e. $h_f \neq h_t$ and $\theta \neq 0$, the total normal force \tilde{N}_b is approximated by using the average value of the displacements, h_f and h_t , at the leading and trailing ends of the block expressed as:

$$\tilde{N}_w = \begin{cases} -\frac{\mu L^3}{(0.5*(h_f + h_t))^3} \dot{y} & \text{for } 0.5*(h_f + h_t) > h_r \\ -\frac{\mu L^3}{h_r^3} \dot{y} & \text{for } 0.5*(h_f + h_t) \leq h_r \end{cases} \quad (4.25)$$

The moment M_w is assumed to be:

$$M_w = \begin{cases} -\frac{\mu}{0.5*(h_f + h_t)^3} \dot{\theta} L^5 \sin(\theta) & \text{for } 0.5*(h_f + h_t) > h_r \\ -\frac{\mu}{h_r^3} \dot{\theta} L^5 \sin(\theta) & \text{for } 0.5*(h_f + h_t) \leq h_r \end{cases} \quad (4.26)$$

It can be seen that Equation 4.26 yields a moment M_w of zero when the bottom surface of the block is parallel to the underlying ground ($\theta = 0$).

4.3.6.2 Soil damping

When the block is in contact with the underlying ground, the kinetic energy of the block dissipates into the underlying ground by wave propagation. To simulate the effect of energy dissipation, soil damping forces D_{sd} and D_{su} are applied on the lower corners of the block as shown in Figure 4.2 (b). When the downstream corner of the block is not in contact with the underlying ground, i.e. $h_t > 0$, the force D_{sd} is zero. When the downstream corner of the block is in contact with the underlying ground, i.e. $h_t \leq 0$, the force D_{sd} is estimated by Equation 4.27. Similarly, the force D_{su} is calculated by Equation 4.28.

$$D_{sd} = \begin{cases} 0 & \text{for } h_t > 0 \\ -\frac{1}{4} L \frac{\sqrt{\rho_g G}}{1-\nu} (\dot{y} - 0.5L \cos \dot{\theta}) & \text{for } h_t \leq 0 \end{cases} \quad (4.27)$$

$$D_{su} = \begin{cases} 0 & \text{for } h_f > 0 \\ -\frac{1}{4} L \frac{\sqrt{\rho_g G}}{1-\nu} (\dot{y} + 0.5L \cos \dot{\theta}) & \text{for } h_f \leq 0 \end{cases} \quad (4.28)$$

Where ρ_g is the total density of soil in the underlying ground, and G is the shear modulus of the underlying soil. Equations 4.27 and 4.28 are based on the analytic solutions for the dynamic response of footings on elastic ground. More details can be found in Richart, et. al. (1970).

4.4 TIME INTEGRATION SCHEME

The sliding process of the block is discretized into a step-by-step phenomenon using Newmark scheme (Newmark, 1959). The initial conditions, and the updating method between two immediate steps are discussed as follows.

4.4.1 Initial Conditions

At the beginning, i.e. $t = 0$, the coordinate $x(0)$, velocities $\dot{y}(0)$ and $\dot{\theta}(0)$ of the block are assumed to be zero. The block is also assumed to be at static rest along the y and θ directions before any kinetic forces are applied. By equating the component of the effective weight (G') along y direction with the support of the underlying ground (N'_{bu} and N'_{bd}), the initial coordinate $y(0)$ of the block is computed. By setting the resultant moment of the support (N'_{bu} and N'_{bd}) and resistance ($c \cdot L$) by underlying ground to be zero, the initial coordinate $\theta(0)$ of the block is computed. The initial velocity $\dot{x}(0)$ is assumed to be known. The dynamic equilibrium of the block is then solved for to compute the initial accelerations $\ddot{x}(0)$, $\ddot{y}(0)$ and $\ddot{\theta}(0)$.

4.4.2 Newmark Scheme

During any increment of time, the accelerations of the block are assumed to be constant and equal to the average value of the accelerations at the beginning and end of the time increment. For any time step, the variables including accelerations ($\ddot{x}(t)$, $\ddot{y}(t)$, $\ddot{\theta}(t)$), velocities ($\dot{x}(t)$, $\dot{y}(t)$, $\dot{\theta}(t)$) and coordinates ($x(t)$, $y(t)$, $\theta(t)$) at the beginning of the time increment ($time = t$) are given. An iterative method is used to compute the

variables, $\ddot{x}(t + \Delta t)$, $\ddot{y}(t + \Delta t)$, $\ddot{\theta}(t + \Delta t)$, $\dot{x}(t + \Delta t)$, $\dot{y}(t + \Delta t)$, $\dot{\theta}(t + \Delta t)$, $x(t + \Delta t)$, $y(t + \Delta t)$, and $\theta(t + \Delta t)$ at the end of the time increment ($time = t + \Delta t$).

For the first iteration, the accelerations at the end of the increment are assumed to be equal to those at the beginning, i.e.

$$\ddot{x}(t + \Delta t) = \ddot{x}(t) \quad (4.29)$$

$$\ddot{y}(t + \Delta t) = \ddot{y}(t) \quad (4.30)$$

$$\ddot{\theta}(t + \Delta t) = \ddot{\theta}(t) \quad (4.31)$$

For each iteration, the following steps are conducted:

6. The average accelerations during the increment, velocities and displacements at the end of the increment are calculated as follows:

$$\ddot{x}_{(from\ t\ to\ t+\Delta t)} = 0.5 * (\ddot{x}(t) + \ddot{x}(t + \Delta t)) \quad (4.32)$$

$$\ddot{y}_{(from\ t\ to\ t+\Delta t)} = 0.5 * (\ddot{y}(t) + \ddot{y}(t + \Delta t)) \quad (4.33)$$

$$\ddot{\theta}_{(from\ t\ to\ t+\Delta t)} = 0.5 * (\ddot{\theta}(t) + \ddot{\theta}(t + \Delta t)) \quad (4.34)$$

$$\dot{x}(t + \Delta t) = \dot{x}(t) + \ddot{x}_{(from\ t\ to\ t+\Delta t)} \Delta t \quad (4.35)$$

$$\dot{y}(t + \Delta t) = \dot{y}(t) + \ddot{y}_{(from\ t\ to\ t+\Delta t)} \Delta t \quad (4.36)$$

$$\dot{\theta}(t + \Delta t) = \dot{\theta}(t) + \ddot{\theta}_{(from\ t\ to\ t+\Delta t)} \Delta t \quad (4.37)$$

$$x(t + \Delta t) = x(t) + \dot{x}(t) \Delta t + \frac{1}{2} \ddot{x}_{(from\ t\ to\ t+\Delta t)} \Delta t^2 \quad (4.38)$$

$$y(t + \Delta t) = y(t) + \dot{y}(t) \Delta t + \frac{1}{2} \ddot{y}_{(from\ t\ to\ t+\Delta t)} \Delta t^2 \quad (4.39)$$

$$\theta(t + \Delta t) = \theta(t) + \dot{\theta}(t) \Delta t + \frac{1}{2} \ddot{\theta}_{(from\ t\ to\ t+\Delta t)} \Delta t^2 \quad (4.40)$$

7. The forces on the block at the end of the increment are calculated using the displacement and velocity calculated by Equations 4.35 to 4.40.
8. The dynamic equilibrium of the block is solved for to compute the accelerations at the end of the increment ($\ddot{x}(t + \Delta t)$, $\ddot{y}(t + \Delta t)$ and $\ddot{\theta}(t + \Delta t)$).

9. The newly computed accelerations, $\ddot{x}(t + \Delta t)_{new}$, $\ddot{y}(t + \Delta t)_{new}$ and $\ddot{\theta}(t + \Delta t)_{new}$ are compared with $\ddot{x}(t + \Delta t)$, $\ddot{y}(t + \Delta t)$ and $\ddot{\theta}(t + \Delta t)$ used in

step 1. An error for the iteration is computed as:

$$error = \max \left(\left| \frac{\ddot{x}(t + \Delta t)_{new} - \ddot{x}(t + \Delta t)}{\ddot{x}(t + \Delta t)} \right|, \left| \frac{\ddot{y}(t + \Delta t)_{new} - \ddot{y}(t + \Delta t)}{\ddot{y}(t + \Delta t)} \right|, \left| \frac{\ddot{\theta}(t + \Delta t)_{new} - \ddot{\theta}(t + \Delta t)}{\ddot{\theta}(t + \Delta t)} \right| \right) \quad (4.41)$$

10. If the error is not acceptably small, the newly computed accelerations are substituted into Equations 4.32 to 4.40 to start another iteration; Steps 1-5 are repeated until the error is acceptably small.

After the iterations are completed, the next time step is considered. The newly computed variables, $\ddot{x}(t + \Delta t)$, $\ddot{y}(t + \Delta t)$, $\ddot{\theta}(t + \Delta t)$, $\dot{x}(t + \Delta t)$, $\dot{y}(t + \Delta t)$, $\dot{\theta}(t + \Delta t)$, $x(t + \Delta t)$, $y(t + \Delta t)$ and $\theta(t + \Delta t)$ from the last step are given as starting conditions, $\ddot{x}(t)$, $\ddot{y}(t)$, $\ddot{\theta}(t)$, $\dot{x}(t)$, $\dot{y}(t)$, $\dot{\theta}(t)$, $x(t)$, $y(t)$ and $\theta(t)$ for the new step. The iterative method discussed above is then repeated to compute the variables at the end of the new time step.

4.5 IMPLEMENTATION

The scheme of the block model is implemented in a computer code programmed in the C programming language. The program is named rect1.cpp and details on the program including input, output files and flow charts are discussed in the sections below.

4.5.1 Input and Output

The program reads from an input file named rect.in. The parameters specified in the input file and their physical meanings are summarized in Table 4.2. The numerical results are written into a file named output.out. The variables written into output.out and their physical meanings are listed in Table 4.3.

Table 4.2 Input parameters and physical meanings

Parameter	Physical meaning
dt	Time increment for the time integration scheme Δt (second)
timelimit	Time limit on the sliding process (second)
errorlimit	The allowance of errors when iterative methods are involved
H	Height of block H (meter)
L	Length of block L (meter)
Cohesion	The static shear strength of soil at the interface of block and underlying ground τ_y (pa)
viscosity	Non-dimensional constant related to the strain rate effect of shear strength μ_s
roughness	The height of roughness at the interface of block and underlying ground h_r (m)
pou	Total density of soil in the block ρ_s (kg/m^3)
lamida	The absolute value of the ratio of the lowest pressure along the top surface to the stagnation pressure $ \lambda $
headratio	The ratio of block's height at the leading edge to its average height (This ratio only influences the area where the kinetic pressure along the leading edge is applied.)
toppressurerange	The ratio of the length where negative kinetic pressure is applied to the height of the block β
totaldensityofground	The total density of soil in the underlying ground ρ_g (kg/m^3)
E	The effective young' modulus of soil in the underlying ground (pa)
poisson	The effective poisson's ratio of soil in the underlying ground
velox	The initial velocity of the block in the x direction $\dot{x}(0)$ (m/s)
step	
posi	The x coordinate of the starting position for a step (m)
fei	The slope angle of the surface of the underlying ground (degree)

Table 4.3 Output variables and physical meanings

Variable	Physical meaning
time	Time t (s)
accx0	The acceleration in the x direction \ddot{x} (m/s^2)
accy0	The acceleration in the y direction \ddot{y} (m/s^2)
acctheta0	The angular acceleration in the $x - o - y$ plane $\ddot{\theta}$ (rad/s^2)
velox	The velocity in the x direction \dot{x} (m/s)
veloy	The velocity in the y direction \dot{y} (m/s)
velotheta	The angular velocity in the $x - o - y$ plane $\dot{\theta}$ (rad/s)
x	The x coordinate of the center of the block (m)
y	The y coordinate of the center of the block (m)
theta	The rotation of the block θ
front	The force on the leading edge of the block due to kinetic pressure (N/m)
tail	The force on the trailing edge of the block due to kinetic pressure (N/m)
top	The force on the top surface of the block due to viscous shear (N/m)
bottomf	The force on the bottom surface of the block due to viscous shear (N/m)
bottomp	The force on the bottom surface of the block due to kinetic pressure (N/m)
toppressure	The force on the top surface of the block due to kinetic pressure (N/m)
Nf	The support by underlying ground at the front end (N/m)
Nt	The support by underlying ground at the tail end (N/m)
totalcohesion	The resistance on the block by underlying ground (N/m)
M	The total moment on the block ($N \cdot m/m$)
soildampingfront	The damping force applied by underlying ground at the front end (N/m)
soildampingtail	The damping force applied by underlying ground at the tail end (N/m)
waterdampingforce	The damping force applied by surrounding fluid (N/m)
waterdampingmoment	The damping moment applied by surrounding fluid ($N \cdot m/m$)

4.5.2 Flow Chart

The flow chart for the program rect1.cpp is shown in Figure 4.10. The subroutine force computes all the forces and moments applied on the block. The major parameters involved in this subroutine are listed in Table 4.4 and the flow chart for the subroutine is shown in Figure 4.11.

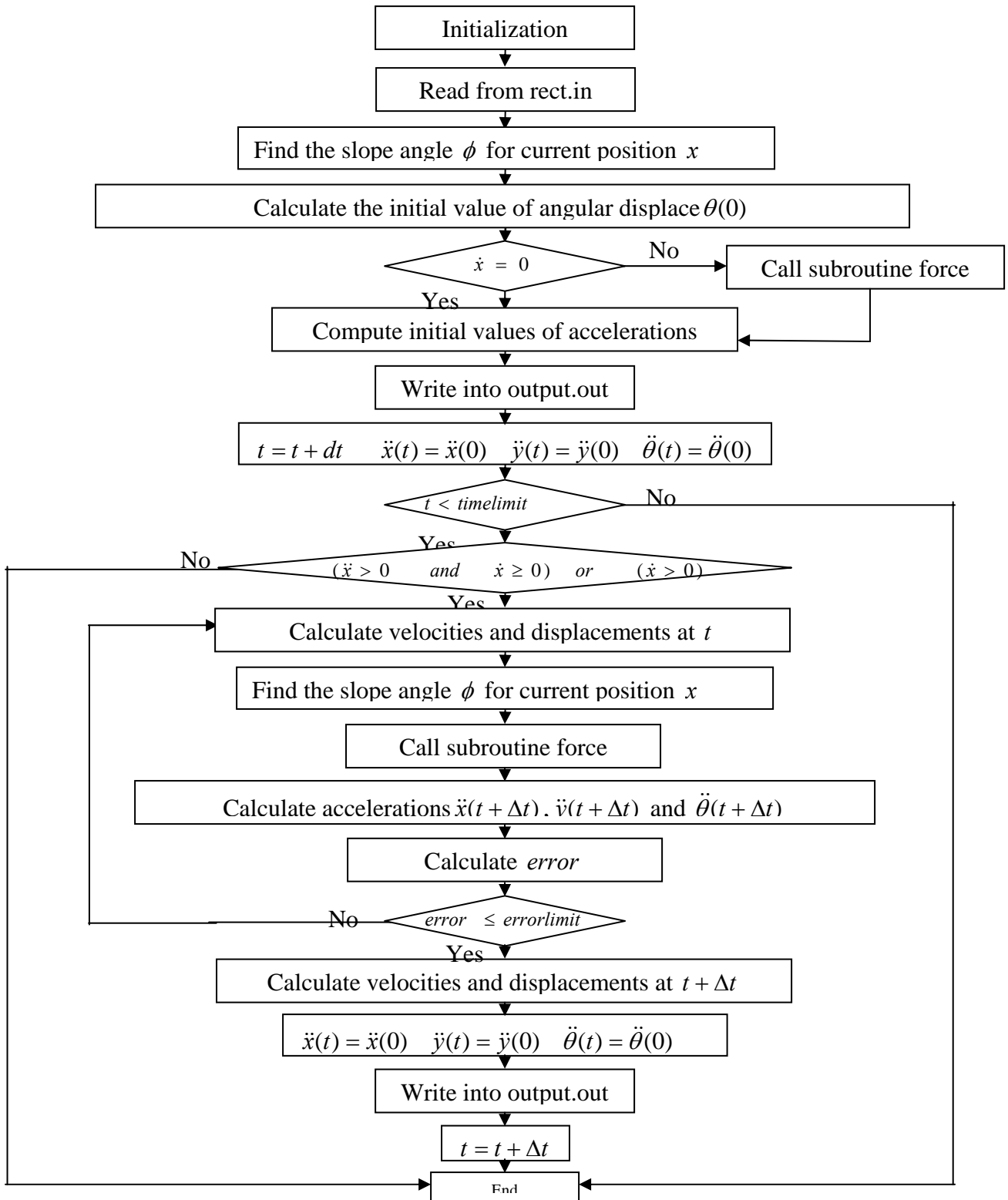


Fig. 4.10 Flow chart of program rect1.cpp

Table 4.4 Parameters in subroutine force and their physical meanings

Variable	Physical meaning
Cohesion	The static shear strength of soil at the interface of block and underlying ground τ_y (pa)
viscosity	Non-dimensional constant related to the strain rate effect of shear strength μ_s
E	The effective young' modulus of soil in the underlying ground (pa)
poisson	The effective poisson's ratio of soil in the underlying ground
topressurerange	The ratio of the length where negative kinetic pressure is applied to the height of the block β
totaldensityofground	The total density of soil in the underlying ground ρ_g (kg/m^3)
roughness	The height of roughness at the interface of block and underling ground h_r (m)
pou	Total density of soil in the block ρ_s (kg/m^3)
lamida	The absolute value of the ratio of the lowest pressure along the top surface to the stagnation pressure $ \lambda $
headratio	The ratio of block's height at the leading edge to its average height (This ratio only influences the area where the kinetic pressure along the leading edge is applied.)
H	Height of block H (meter)
L	Length of block L (meter)
currentfei	The slope angle the underlying ground for current position (rad)
hydroplaning	The variable marks the onset of hydroplaning. This variable is 0 before hydroplaning occurs and 1 after hydroplaning occurs.
velox	The velocity in the x direction \dot{x} (m/s)
veloy	The velocity in the y direction \dot{y} (m/s)
velotheta	The angular velocity in the $x - o - y$ plane $\dot{\theta}$ (rad/s)
x	The x coordinate of the center of the block(m)
y	The y coordinate of the center of the block(m)
theta	The rotation of the block θ
front	The force on the leading edge of the block due to kinetic pressure (N/m)
tail	The force on the trailing edge of the block due to kinetic pressure (N/m)
top	The force on the top surface of the block due to viscous shear (N/m)
bottomf	The force on the bottom surface of the block due to viscous shear (N/m)
bottomp	The force on the bottom surface of the block due to kinetic pressure (N/m)
toppressure	The force on the top surface of the block due to kinetic pressure(N/m)
Nf	The support by underlying ground at the front end (N/m)
Nt	The support by underlying ground at the tail end (N/m)
totalcohesion	The resistance on the block by underlying ground (N/m)

Variable	Physical meaning
M	The total moment on the block ($N \cdot m / m$)
soildampingfront	The damping force applied by underlying ground at the front end (N / m)
soildampingtail	The damping force applied by underlying ground at the tail end (N / m)
waterdampingforce	The damping force applied by surrounding fluid (N / m)
waterdampingmoment	The damping moment applied by surrounding fluid ($N \cdot m / m$)

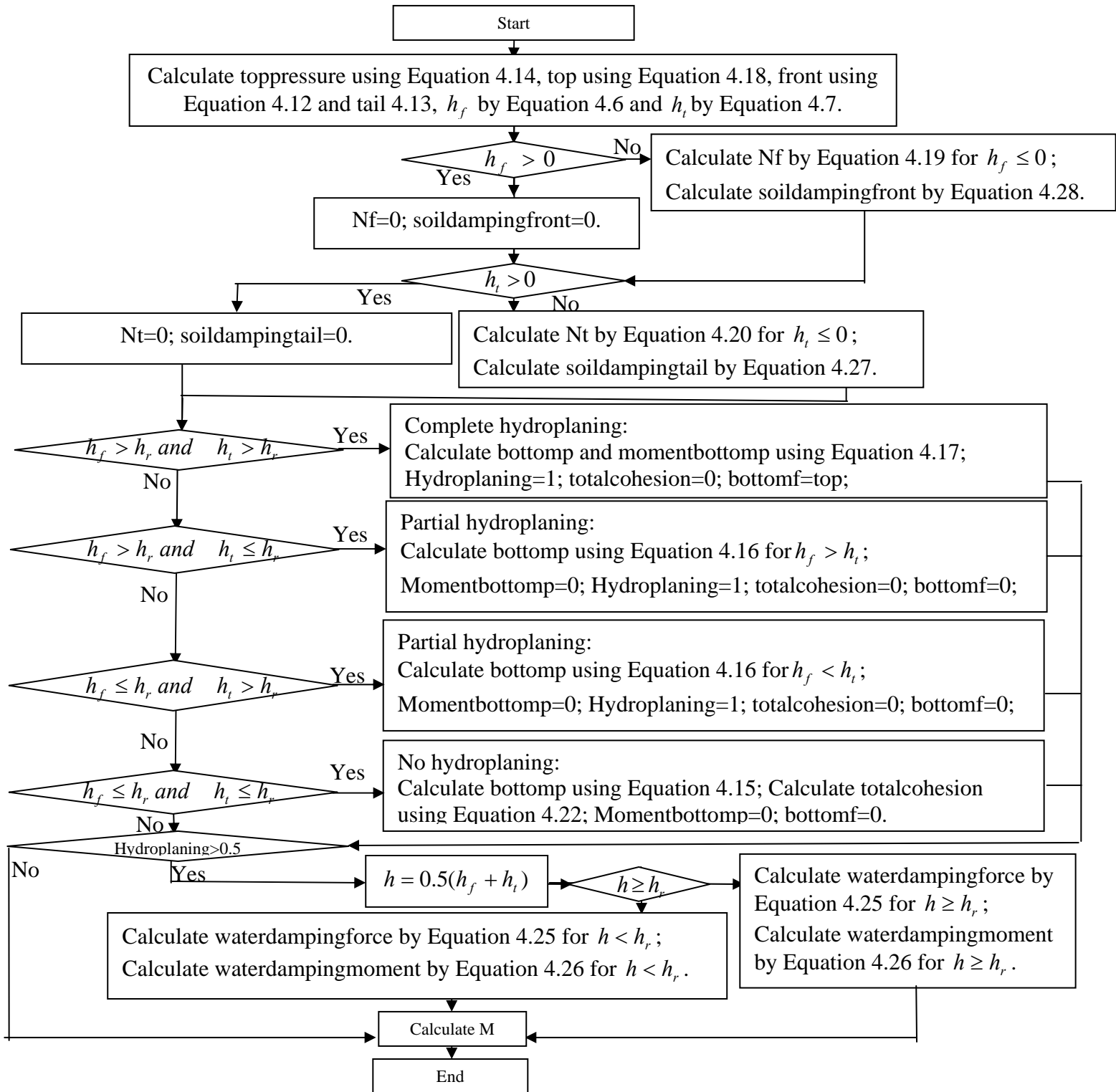


Fig. 4.11 Flow chart of subroutine force

4.6 SUMMARY

In this chapter, a block model has been developed for the dynamic response of submarine slides. The occurrence of hydroplaning was simulated by monitoring and comparing the displacement of the block in the direction normal to the underlying ground with the height of roughness h_r at the interface between the block and underlying ground. The effective weight of the block, the kinetic pressures and viscous shears by surrounding fluid, the support and resistance by underlying ground, and the forces due to kinetic and soil damping effects were considered in the block model. The influence of hydroplaning was also accounted for by making the forces on the block compatible with the contact condition between the block and underlying ground. The sliding process of the block was discretized into a step-by-step phenomenon using Newmark scheme. The block model has been implemented by programming in the C programming language. In order to validate the block model, it is compared with the laboratory experiments by Mohrig, et al. (1999) as discussed in the next chapter.

Chapter 5: Validation of the Block Model

In this chapter, the block model is compared with the laboratory experiments by Mohrig et al. (1999). The conditions of Mohrig, et al.'s experiments are first summarized and the input parameters for the block model are discussed. Numerical results from the block model are then compared with the experimental data. The occurrence of hydroplaning of the slide mass is also analyzed.

5.1 EXPERIMENTAL CONDITIONS

Mohrig, et al. (1999) performed laboratory experiments on subaqueous slides. In their experiments, they released soil from a large box into a channel with transparent sides. The box from which soil was released was at the upper end of the channel and had a slot 20 mm high and 170 mm wide. The channel was approximately 10 m long, 3 m deep and 20 cm wide. It was segmented with a break in slope, the upper and lower slope angles being 6 and 1 degrees, respectively. The break in slope was located approximately 5.7 m downslope from the position where the soil was released. The bottom surface of the channel was a rubber mat which was crenelated into rectangular ridges and grooves. The width of each ridge and groove was 6.4 mm, and the elevation difference between them was 3.2 mm.

In each experiment, approximately 30 liters of soil were released. The total time to empty the soil box was about 3.5 s. The properties of the soil are summarized in Table 5.1. The water content of the soil was 63.9%. The soil consisted of a mixture of 40% kaolin, 40% silt and 20% sand by dry weight. The total density of the soil, ρ_s , was approximately 1.6 t/m^3 . The static shear strength of the soil τ_y varied from 33 to 49 Pa. The effect of strain rate on the shear strength c was considered as follows:

$$c = \tau_y + \mu_s \dot{\gamma} \quad (5.1)$$

Where μ_s is a constant and $\dot{\gamma}$ is shear strain rate. The constant μ_s varied from 0.019 to $0.035 \text{ kg} \cdot \text{m}^{-1} \cdot \text{s}^{-1}$. A grain-size analysis was conducted on the soil and D_{95} was 0.7 mm.

Table 5.1 Input parameters for experimental cases

Run	Bottom surface of channle	Static shear strength τ_y (Pa)	μ_s ($\text{kg} \cdot \text{m}^{-1} \cdot \text{s}^{-1}$)	Height of the slide mass H (mm)
1w	Clean	49	0.035	18
2w	Clean	49	0.035	18
3w	Clean	36	0.023	16
4w	Soil	49	0.035	6.5
5w	Soil	33	0.019	16

Mohrig, et al performed five experiments named Run 1w to Run 5w. For Runs 1w to 3w, the bottom surface of the channel was clean when the soil was released. For Runs 4w and 5w, a layer of soil was placed on the bottom of the channel. For all five runs, the heights of the slide masses H were measured and listed in Table 5.1. The velocities, U , of the front of the slide mass were reported as functions of run-out distances, x , and are plotted in Figure 5.1.

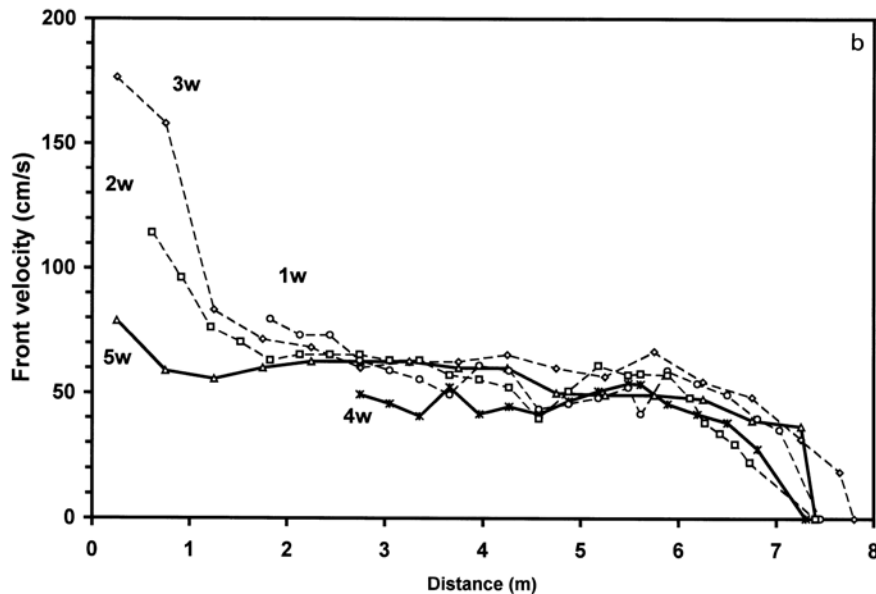


Fig. 5.1 Reported front velocity vs run-out distance (Mohrig, et al. (1999))

5.2 INPUT PARAMETERS

The input parameters used for the block model were based on the experimental conditions reported by Mohrig, et al. (1999). Some parameters were determined directly based on the data reported by Mohrig, et al; other parameters were determined by trial and error. The parameters are listed in Table 5.2 and discussed below.

Table 5.2 Input parameters for block model

Run	3w	1w	2w	4w	5w
Slope angle δ	6° for the first 5.7m downslope, and 1° for the rest				
Head ratio α	2				
Non-dimensional constant λ	5				
Non-dimensional constant β	0.5				
The modulus of elasticity for the underlying ground E (kpa)	8000				
Poisson's ratio for the underlying ground ν	0.4				
Density of soil ρ_s (kg/m^3)	1600				
Height of roughness h_r (mm)	3.2	3.2	3.2	0.7	0.7
Static shear strength τ_y (Pa)	36	49	49	49	33
μ_s ($kg \cdot m^{-1} s^{-1}$)	2.3E-02	3.5E-02	3.5E-02	3.5E-02	1.9E-02
Height of the block H (m)	1.6E-02	1.8E-02	1.8E-02	6.5E-03	1.6E-02
Initial velocity (m/s)	3.0	2.5	1.5	0.6	0.8
Dynamic viscosity of surrounding fluid μ (Pa s)	2.3E-03	3.5E-03	3.5E-03	3.5E-03	1.9E-03
Time increment Δt (s)	1.0E-04	1.0E-04	1.0E-04	1.0E-05	1.0E-05
Block length L (m)	0.46	0.52	0.52	0.17	0.46

5.2.1 Parameters Determined Directly

The height of roughness h_r was assumed to be equal to the elevation difference of the ridges and grooves for the runs where the bottom surface of the channel was clean. For the runs where the bottom of the channel was covered by soil, the height of roughness h_r was assumed to be D_{95} of the soil. The head ratio α of the block is based on the frontal shape of the sliding mass as shown in Figure 5.2. The non-dimensional constants λ and β are based on the frontal shape of the sliding mass and the numerical modeling of hydrodynamic stresses. The modulus of elasticity for the underlying ground E and the Poisson's ratio for the underlying ground ν are based on general properties for loose sandy silt (Das, B. 1999). Considering mixing of soil and surrounding fluid, the viscosity of the surrounding fluid μ was taken as 10% of the quantity μ_s . The height of the block H was assumed to be the average height of the slide mass over the length of the channel with a slope of 6 degrees. The initial velocity of the block is based on Figure 5.1. The plot of front velocity vs run-out distance was extrapolated to estimate the initial front velocity at a run-out distance of zero. The estimated front velocity is assumed to be the initial velocity of the block.



Fig. 5.2 Frontal shape of the sliding soil mass (Mohrig, et al. 1999)

5.2.2 Parameters determined by trial and error

The increment of time Δt used in the block model computations was determined by trial and error. Three values for Δt of 0.001 s, 0.0001 s and 0.00001 s were tried. For Runs 1w to 3w, the numerical results for $\Delta t = 0.001$ s are the same as those for $\Delta t = 0.0001$ s. Thus using Δt of 0.0001 s was assumed to be sufficient. For Runs 4w and 5w, the numerical results for $\Delta t = 0.001$ s were different from those for $\Delta t = 0.0001$ s. However, the numerical results for $\Delta t = 0.0001$ s were the same as those for $\Delta t = 0.00001$ s. Thus using Δt of 0.00001 s was assumed to be sufficient.

The length of the block L was also determined by trial and error. For every experiment, the length of the slide mass was zero at the beginning of the experiment, but it increased as the soil slide down in the channel. At the end of the experiment, the length of the slid mass was equal to the run-out distance. However, in the block model, the length of the block was assumed to be constant. In order to determine the appropriate lengths L of the block for every experiment, it was assumed that the length-to-height ratios of the block L/H were the same for all five experiments. As shown in Figure 5.1, over run-out distances smaller than 2 meters, more data points were reported for Run 3w than most of the other runs. Therefore, Run 3w was analyzed as a representative case to find the optimum length-to-height ratio L/H for all runs. Five values for length-to-height ratio L/H were tried. The length-to-height ratio of the block L/H is assumed to be constant for all the runs. The length-to-height ratios and corresponding lengths of the block are listed in Table 5.3. The computed front velocities vs run-out distances are shown in Figure 5.3. The reported velocities vs run-out distances for Run 3w are also shown in Figure 5.3. It can be seen that when the length of the block L is 0.46 m and length-to-height ratio L/H is 28.75, the numerical results fit the reported experimental values the best. Therefore the length-to-height ratio L/H is assumed to be 28.75 for all the runs. The lengths of the block L calculated based on the length-to-height ratio L/H as 28.75 for all the runs are listed in Table 5.2.

Table 5.3 Trial for length-to-height ratio L/H

Length-to-height ratio L/H	18.75	25.00	28.75	31.25	37.50
Length of the Block L (m)	0.30	0.40	0.46	0.50	0.60

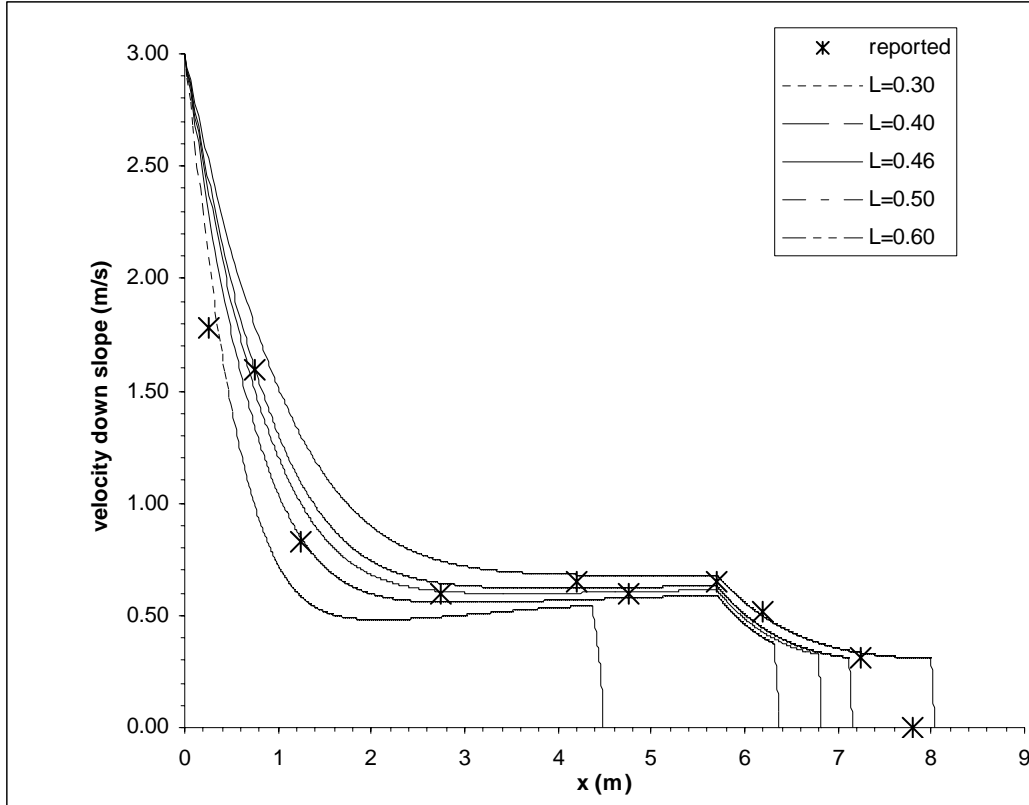


Fig. 5.3 Front velocity vs run-out distance for Run 3w

5.3 COMPARISON OF NUMERICAL RESULTS WITH EXPERIMENTAL DATA

Mohrig, et al. reported the front velocities vs run-out distances for the five tests. They also observed that hydroplaning occurred in all five of the tests. The calculated front velocities vs run-out distances are compared with the experimental data and the occurrence of hydroplaning predicted by the block model are discussed in this section.

5.3.1 Front Velocity vs Run-out Distance

The calculated and measured front velocities vs run-out distances for Run 3w are shown in Figure 5.3. The calculated front velocities vs run-out distances for runs 1w, 2w,

4w and 5w are shown in Figures 5.4 to 5.7 together with the reported data. It can be seen that the numerical results agree favorably with the experimental data for all five runs.

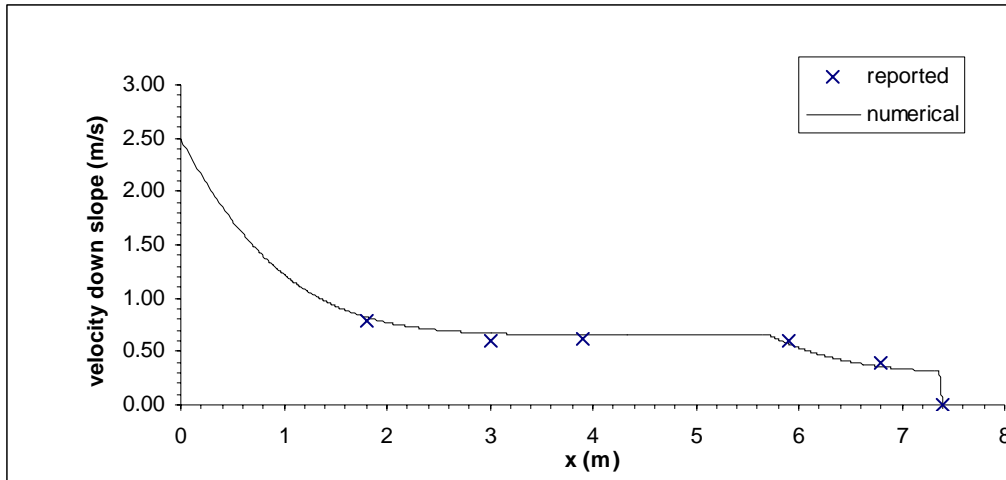


Fig. 5.4 Front velocity vs run-out distance for Run 1w

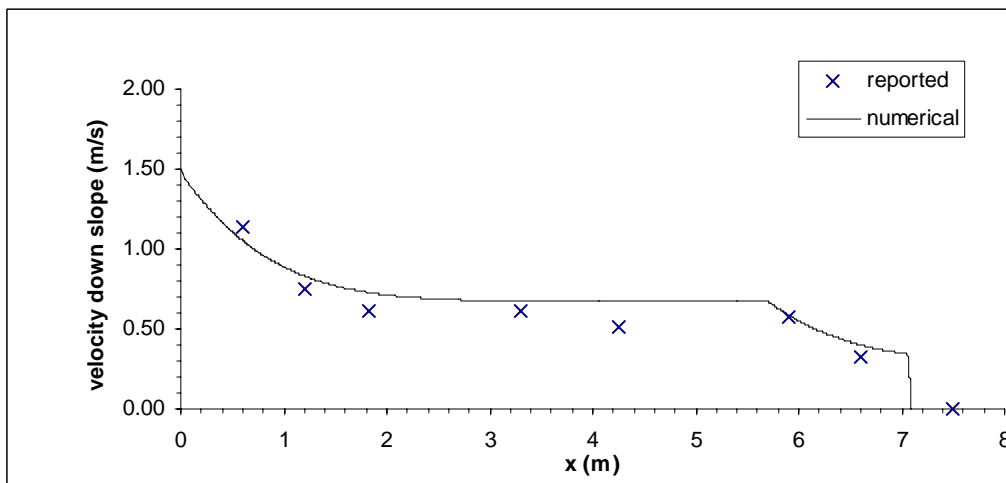


Fig. 5.5 Front velocity vs run-out distance for Run 2w

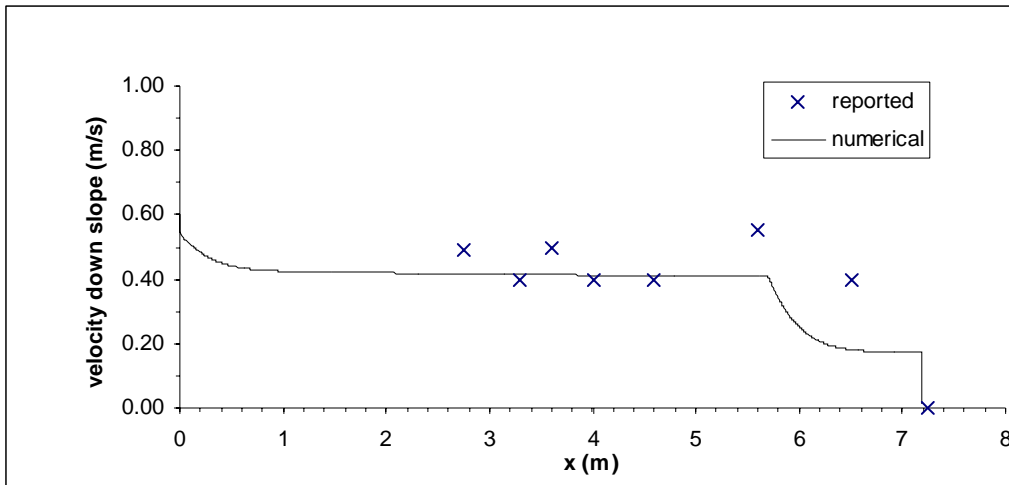


Fig. 5.6 Front velocity vs run-out distance for Run 4w

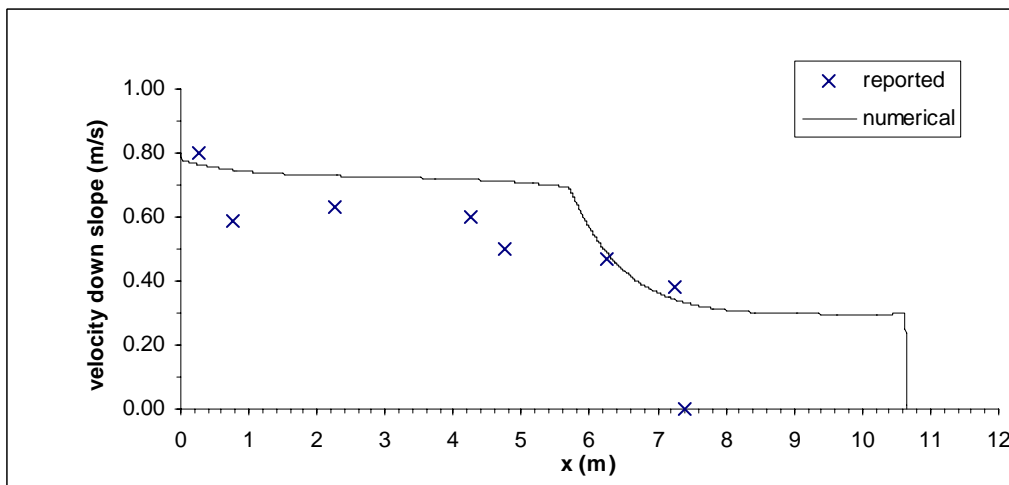


Fig. 5.7 Front velocity vs run-out distance for Run 5w

5.3.2 Occurrence of Hydroplaning

The calculated displacements, h_f and h_t , in the y direction normal to the underlying slope at the front and tail ends of the block, respectively, are plotted against the run-out distances for Runs 1w to 5w in Figures 5.8 to 5.12. The heights of roughness h_r are also plotted in Figures 5.8 to 5.12. It can be seen that the one or both of the displacements h_f and h_t are larger than the heights of roughness h_r over a portion of the

run-out distance for all five tests. The ranges of run-out distances over which the displacements h_f and h_t are larger than the heights of roughness h_r are listed in Table 5.4 for Runs 1w to 5w. Thus the block model indicated that the slide masses should hydroplane in all tests. This prediction is consistent with the observations by Mohrig, et al and provides further confirmation of the block model.

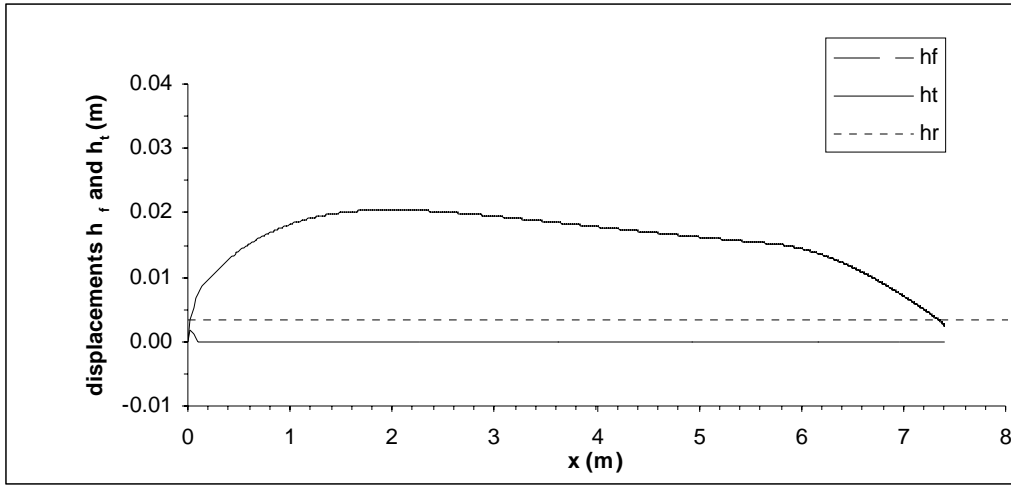


Fig. 5.8 Displacements h_f and h_t vs run-out distance for Run 1w

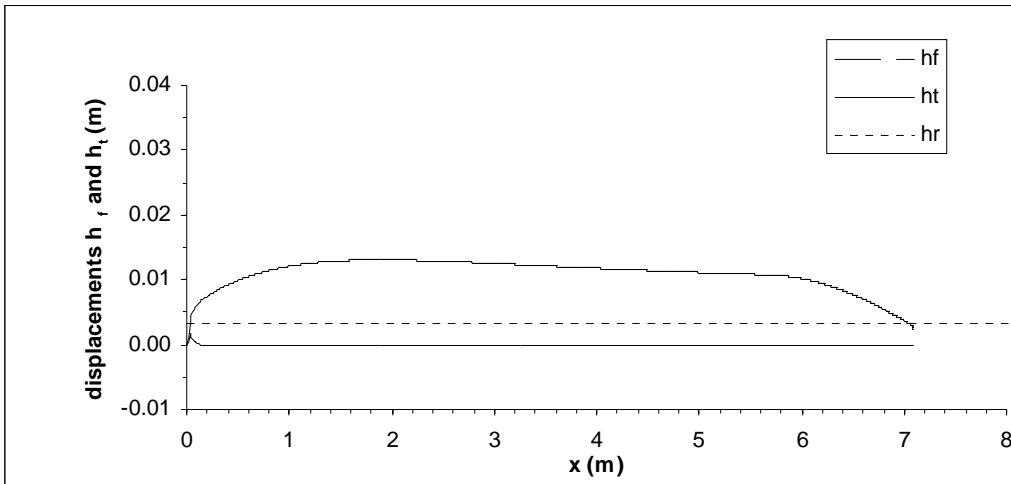


Fig. 5.9 Displacements h_f and h_t vs run-out distance for Run 2w

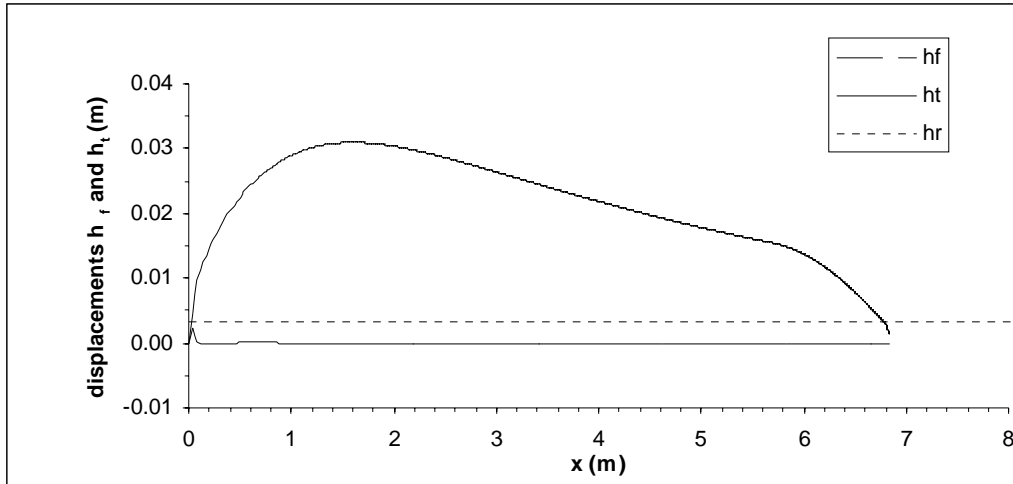


Fig. 5.10 Displacements h_f and h_t vs run-out distance for Run 3w

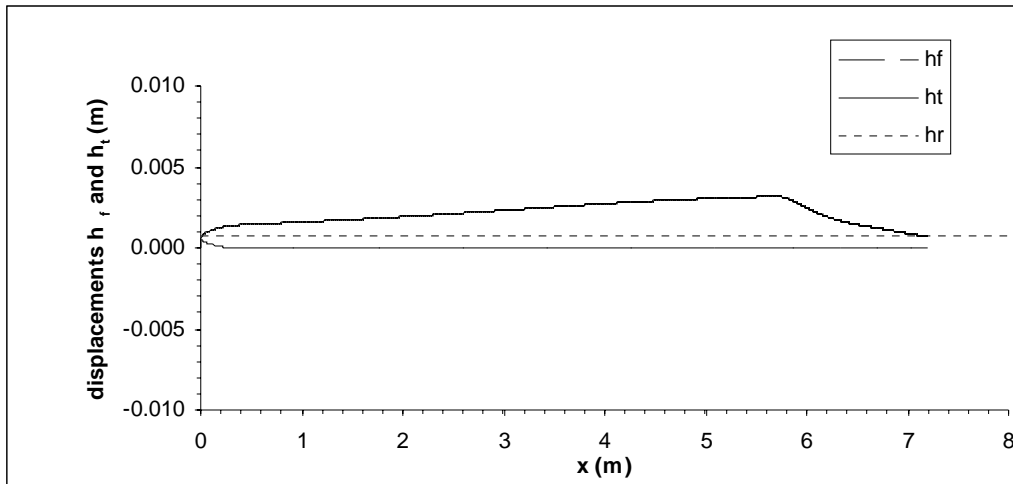


Fig. 5.11 Displacements h_f and h_t vs run-out distance for Run 4w

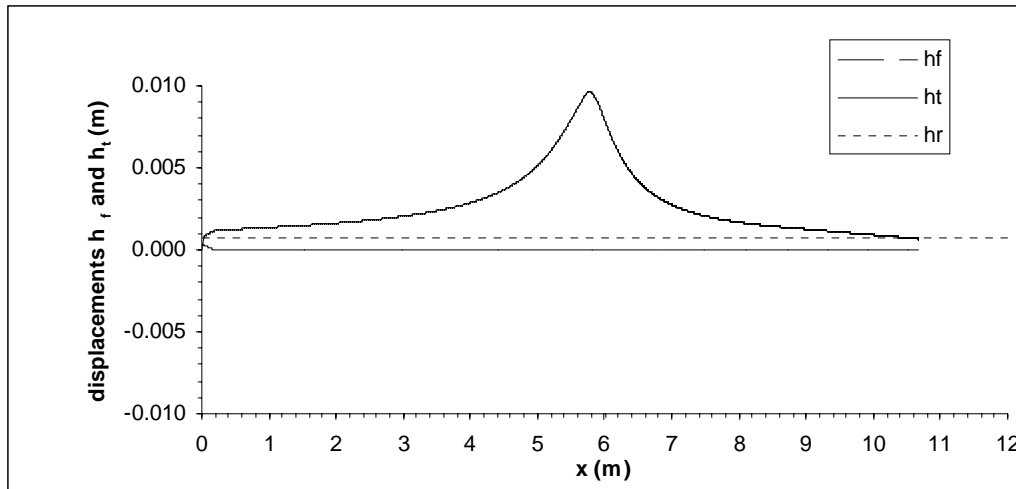


Fig. 5.12 Displacements h_f and h_t vs run-out distance for Run 5w

Table 5.4 Ranges of run-out distance over which the block hydroplanes

Run	1w	2w	3w	4w	5w
Minimum run-out distance where $\max(h_f, h_t) \geq h_r$ (m)	0.02	0.03	0.03	0.01	0.02
Maximum run-out distance where $\max(h_f, h_t) \geq h_r$ (m)	7.36	7.05	6.78	7.18	10.62

5.4 CONCLUSIONS

The block model has been applied to simulate the five experiments for subaqueous slides performed by Mohrig, et al. The numerical results from the block model agree well with the experimental data. The block model also predicted the occurrence of hydroplaning successfully.

5.5 SEQUENCE OF SLIDING STAGES

To illustrate the sliding process, the motion of subaqueous slides can be divided into six stages. The sequence of six stages for Run 1w is illustrated in Figure 5.13. In Stage 1, the slide mass starts moving with an initial velocity down slope. At Stage 2, the slide mass starts to hydroplane when the maximum distance, $\max(h_f, h_t)$, between the

bottom surface of the slide mass and the underlying ground is larger than the height of roughness, h_r , at the interface of the slide mass and the underlying ground. Stage 3 represents steady-state hydroplaning where the velocity of the slide mass is constant. In Stage 4, the slide mass decelerates due to the change in inclination of the underlying slope. During Stage 5, the slide mass stops hydroplaning when the maximum distance, $\max(h_f, h_t)$, between the bottom surface of the slide mass and the underlying ground is smaller than the height of roughness, h_r , at the interface of the slide mass and the underlying ground. Finally, in Stage 6, the final stage of the sliding process, the slide mass stops moving.

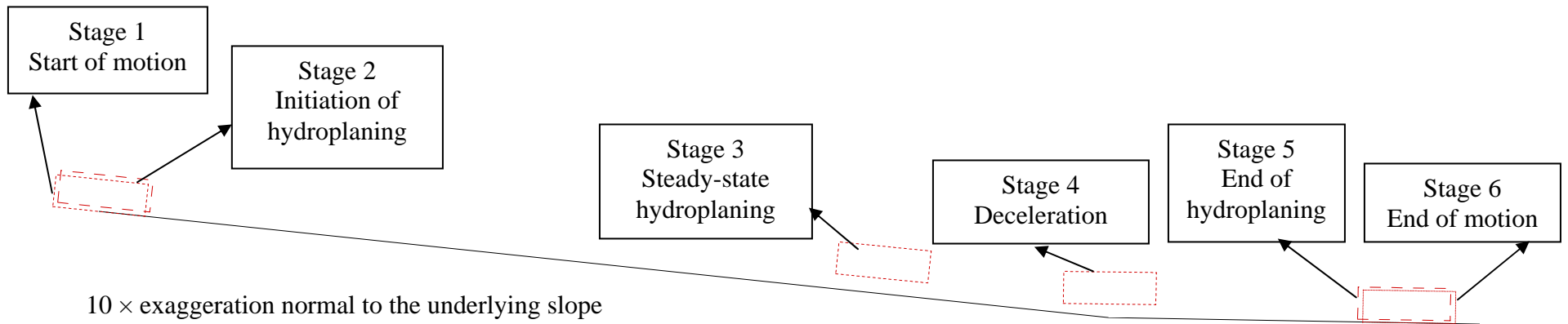


Fig. 5.13 Sequence of sliding stages for Run 1w

Chapter 6: Summary and Conclusions

Many submarine slides travel large distances that are much greater than those of comparable subaerial slides. One possible reason for the large travel distances is that hydroplaning occurs. The research presented in this report was undertaken to understand better the mechanism of hydroplaning of submarine slides.

Previous studies on hydroplaning of submarine slides have two major limitations. One limitation is due to a lack of understanding of the hydrodynamic stresses applied on the slide mass by the surrounding fluid. The other limitation is that the onset of hydroplaning is based on arbitrary assumptions. The objective of this research was to develop a better understanding of the hydrodynamic stresses and incorporate this into a new model for hydroplaning of subaqueous slides.

6.1 SUMMARY OF WORK

The hydrodynamic stresses, i.e. kinetic pressures and viscous shears, applied on the slide mass by the surrounding fluid were studied numerically. For the numerical modeling, the slide mass was assumed to be a streamline shaped rigid body with a constant velocity. Steady two-dimensional flow around the slide mass was simulated using commercial software known as, Fluent 6.1. A Reynolds-Stress turbulent model was applied to simulate the flow. The kinetic pressures and viscous shears along the surfaces of the slide mass were analyzed for slide masses with varying slide velocities, distances between the slide mass and underlying ground, and height-to-width ratios of the front portion of the slide mass. The study produced a better understanding of the interaction between the slide mass and surrounding fluid. The findings regarding the hydrodynamic stresses exerted on the slide mass are summarized in section 6.2.

Once the hydrodynamic stresses were understood better a “block model” was developed for subaqueous slides, with emphasis on possible hydroplaning. In the block model, the slide mass was represented as a rigid rectangular block which moves and rotates in a vertical plane. The occurrence of hydroplaning was determined by the contact condition between the bottom surface of the block and the underlying ground, i.e. by comparing the height of roughness at the interface between the block and underlying ground with the displacement of the block in the direction normal to the underlying ground along the bottom surface of the slide mass. Conclusions derived for the hydrodynamic stresses on the slide mass were applied as stress boundary conditions for the block model. The sliding process of the block was discretized in a step-by-step manner using a Newmark scheme. A computer program was also written to implement the block model.

Once the block model was developed, laboratory experiments on subaqueous slides conducted by Mohrig, et al (1999) were simulated using the model. The numerical results from the block model were compared with data reported by Mohrig, et al, i.e. the variation in the computed velocities of the front of the slide mass with run-out distances of the slides were compared with measured values. The occurrence of hydroplaning was also analyzed by comparing the calculated displacements of the block normal to the underlying ground with the heights of roughness over the run-out distances. Conclusions drawn from the comparison between the block model and experiments are also summarized in Section 6.2.

6.2 CONCLUSIONS

The research reported herein provides a better understanding of subaqueous slides by considering the interactions between the slide mass and the surrounding fluid and between the slide mass and the underlying ground. Unlike previous models for

subaqueous slides, the block model involves no arbitrary assumptions for the hydrodynamic stresses on the slide mass or the on-set condition of hydroplaning.

The numerical study of the interaction between the slide mass and surrounding fluid has produced the following conclusions regarding the hydrodynamic stresses on the surfaces of the slide mass:

1. When normalized by the stagnation pressure p_{stag} , the non-dimensional kinetic pressures on the surfaces of the slide mass are not influenced by the magnitude of the inflow velocity;
2. Along the top surface of the slide mass, hydrodynamic stresses are not influenced by the onset of hydroplaning or the distance between the underlying ground and the bottom surface of the slide mass that hydroplanes;
3. The kinetic pressures on the middle portion of the top surface is essentially zero for slides in deep water;
4. The non-dimensional kinetic pressures on the tail portion of the top surface of the slide mass increases linearly from zero at the intersection of the middle and tail portions to 0.3 at the tail end of the slide mass;
5. The kinetic pressure is negative along the frontal part of the top surface. This kinetic pressure provides a lift on the slide mass. The magnitude of this negative pressure increases as the height-to-width ratio of the slide mass increases;
6. Along the bottom surface of slide mass that hydroplane, the non-dimensional kinetic pressures vary linearly beginning a short distance behind the front nose of the slide mass to the tail end. The pressures at a short distance behind the front nose and at the tail end of the slide mass can be estimated using Equation 3.3;

7. The shear stress along the top and bottom surfaces of the slide mass can be estimated using Equation 3.4;

Incorporating the above conclusions about hydrodynamic stresses, the block model also adjusts the forces applied on the slide mass by the underlying ground according to the contact condition between the slide mass and underlying ground. Using the block model, the mechanism of hydroplaning has been successfully simulated by analyzing the dynamic response of the slide mass under proper stresses applied by the surrounding fluid and underlying ground. The simulations using the block model have also yielded numerical results that agree well with the experimental data reported by Mohrig, et al.

6.3 SUGGESTIONS ON FUTURE RESEARCH

To continue the research reported herein, the understanding of submarine slides can be improved by the following approaches:

1. Case studies can be performed by using the block model to simulate natural submarine slides. Motions of the submarine slides and whether hydroplaning occurs can be predicted for comparison with field observations. For slides that hydroplane, the influence of hydroplaning on run-out distances can be studied;
2. The block model can be improved by considering the deformation of the slide mass and the influence of the acceleration of the slide mass on hydrodynamic stresses. The dynamic response and deformation of the slide mass can be simulated using the finite element method. The hydrodynamic stresses on the surfaces of the slide mass can be studied by modeling the unsteady flow around the slide mass. The new numerical model can then be used to simulate subaqueous slides of any scale and

predict the deformation and movement of the slide mass in time and space based on the initial geometry of the slope when failure occurs, the geomorgraphy of the nearby seafloor, and the mechanical properties of the slide material (including shear strength, stress-deformation properties and unit weight).

References

- Blight, G. E. (1997). "Destructive Mudflows as a Consequence of Tailings Dyke Failures". *Proceedings Institution of Civil Engineers, Geotechnical Engineering*. Vol. 125, pp. 9-18.
- Blight, G. E. and Fourie, A. B. (2005). "Catastrophe Revisited – Disastrous Flow Failures of Mine and Municipal Solid Waste". *Geotechnical and Geological Engineering*. Vol 23, pp 219-248.
- Browne, A. L. and Whicker, D. (1983). *An Interactive Tire-Fluid Model for Dynamic Hydroplaning. Frictional Interaction of Tire and Pavement*. ASTM STP 793.
- Crowe, C. T., Roberson, J. A., and Elger, D. F. (2000). *Engineering Fluid Mechanics*. John Wiley and Sons, Inc. New York.
- Dafalias, Y. F. (1986). "Bounding Surface Plasticity I: Mathematical Foundation and Hypoplasticity." *Journal of Engineering Mechanics*. ASCE. Vol. 112, No. 9, pp. 966-987.
- Dafalias, Y. F. and Hermann, L. R. (1982). *Bounding Surface Formulation in Soil Plasticity, Chapter 10 in Soil Mechanics – Transient and Cyclic Loads*. Edited by G.N. Pande and O.C. Zienkiewicz. John Wiley & Sons Ltd. New York.
- Dafalias, Y. F. and Hermann, L. R. (1986). "Bounding Surface Plasticity II: Application to Isotropic Cohesive Soils." *Journal of Engineering Mechanics*. ASCE. Vol. 112, No. 12, pp. 1236-1291.
- De Blasio, F. V., Engvik, L., Harbitz, C. B. and Elverhøi, A., (2004), "Hydroplaning and submarine debris flows," *Journal of geophysical research*, Vol. 109, C01002, doi: 10.1029/2002JC001714.
- Dobry, R. and Alvares, L. (1967). *Seismic Failures in Chilean Tailings Dams*. *Journal of Soil Mechanics and Foundation Engineering*. Div. ASCE. Vol. 93, SM6, pp. 237-260.
- Egolf, P.W. and Weiss, D. A. (1995). "Model for Plane Turbulent Couette Flow." *Physical Review Letters*. 75. pp2956-2959.
- Ewart, W. D. (1962). *Hydroplanes and Hovercraft*. Frederick Muller Limited. London.
- Ferziger, J. H., Peric, M. (2002). *Computational Methods for Fluid Dynamics*. Springer-Verlag Berlin Heidelberg, New York.
- Fluent 6.2 User's Guide. (2005). *Fluent Inc*.
- Fourie, A. B., Blight, G. E. and Papageorgiou, G. (2001). *Static Liquefaction as a Possible Explanation for the Merriespruit Tailings Dam Failure*. *Canadian Geotechnical Journal*. Vol. 38, pp. 707-719.
- Fread, D.L. (1984). "A breach erosion model for earthen dams". *Proceedings of the Speciality. Conference on Delineation of Landslide, Flash Flood, and Debris Flow Hazards in Utah*. Utah State University, Logan, Utah, 30 pp.

- Gambit 2.2 Modeling Guide. (2004). Fluent Inc.*
- Hampton M. A. (1972). The Role of Subaqueous Debris Flows in Generating Turbidity Currents. Journal of Sedimentary Petrology. Vol. 42, pp. 775-793.*
- Hampton, M. A. and Locat, J. (1996). Submarine Landslides. Reviews of Geophysics. Vol. 34, pp.33-59.*
- Hance, J. J., (2002), Development of a database and assessment of seafloor slope stability based on published literature, M.S. thesis, the university of Texas at Austin.*
- Harbitz, C.B., Parker, G., Elverhøi, A., Marr, J.G., Mohrig, D., and Harff, P.A (2003). "Hydroplaning of subaqueous debris flows and glide blocks: Analytical solutions and discussion," J. Geophys. Res., 108(B7), 2349, doi:10. 1029/2001 JB001454.*
- Harrin, E. N. (1958). Low Tire Friction and Cornering Forces on a Wet Surface. NACA TN 4406.*
- Heim, A. (1882). Der Bergsturz von Elm: Zeitschrift der deutschen geologischen Gesellschaft. Vol 34. pp 74-115.*
- Horne, W. B. and Dreher, R. C. (1963). Phenomena of Pneumatic Tire Hydroplaning. NASA TN D-2056.*
- Hsü, K. J. (1975). Catastrophic Debris Streams (Sturdy Storms) Generated by Rockfalls. Geological Society of America Bulletin. Vol. 86, pp. 129-140.*
- Hutchinson, J.N. 1986. A sliding-consolidation model for flow slides. Canadian Geotechnical Journal, 23: 115–126.*
- Imran, J, and Parker, G (2001). "A Numerical Model of Muddy Subaqueous and Subaerial Debris Flows," Journal of hydrodynamic engineering, Vol 127, Issue 11, pp. 959-968.*
- Iverson, R. M. and LaHusen, R. G. (1993). Friction in Debris Flows: Inferences from Large-scale Flume Experiments. In Shen, H. W., Su, S. T. and Wen F., eds. Hydraulic Engineering 1993. Proceedings of the 1993 Conference: New York. ASCE. pp. 1604-1609.*
- Johnson, A. M. (1970). Physical Processes in Geology; A Method for Interpretation of Natural Phenomena; Intrusions in Igneous Rocks, Fractures, and Folds, Flow of Debris and Ice. San Fransisco, California, Freeman, Cooper and Co., p. 577.*
- Kaliakin, V. N. and Hermann, L. R. (1991). Guidelines for Implementing the Elastoplastic-viscoplastic Bounding Surface Model. Technical Report, Department of Civil Engineering, University of California, Davis.*
- Kokusho, T., Watanabe, K. and Sawano, T. (1998). Effect of Water Film on Lateral Flow Failure of Liquefied Sand. Proceedings of the 11th European Conference on Earthquake Engineering, A. A. Balkema, Rotterdam, The Netherlands, pp. 1-8.*
- Körner HJ (1976) Reichweite und Geschwindigkeit von Bergstürzen und Fleisschneelawinen. Rock Mech 8:225–256.*

- Laval, A., Cremer, M., Beghin, P. and Ravenne, C. (1988). *Density Surges: Two-dimensional Experiments. Sedimentology. (1988) Vol. 35, pp 73-84.*
- Major, J. J. and Pierson, T. C. (1992). *Debris Flow Rheology: Experimental Analysis of Fine-grained Slurries. Water Resources Research. Vol. 28, pp. 841-857.*
- Maniar, D. R. (2004). *A Computational Procedure for Simulation of Suction Caisson Behavior under Axial and Inclined Loads. PhD dissertation. The University of Texas at Austin.*
- Marr, JG, Harff, PA, Shanmugam, G. and Parker, G (2001). "Experiments on Subaqueous Sandy Gravity Flows: The Role of Clay and Water Content in Flow Dynamics and Depositional Structures," *Geological Society of America Bulletin, Vol 113, No. 11, pp1377-1386.*
- Miao, T., Liu, Z. and Niu, Y. (2001). *A Sliding Block Model for Run-out Prediction of High-speed Landslides. Canadian Geotechnical Journal. Vol. 38 (2), pp. 217-226.*
- Mohrig, D., Ehipple, K. X., Hondzo, M. Ellis, C. and Parker, G (1998). *Hydroplaning of subaqueous debris flows, Geol. Soc. Am.Bull., 110, pp 387-394.*
- Mohrig, D, Elverhøi, A and Parker, G (1999). "Experiments on the Relative Mobility of Muddy Subaqueous and Subaerial Debris Flows, and Their Capacity to Remobilize Antecedent Deposits," *Marine Geology, Vol 154, pp 117-129.*
- Moriwaki, H., inokuchi, T., Hattanji, T., Sassa, K., Ochiai, H. and Wang, G. (2004). *Failure Processes in a Full-scale Landslide Experiment Using a Rainfall Simulator. Landslides. Vol. 1, pp. 277-288.*
- Moriwaki, H., Yazaki, S. and Oyagi, N (1985). *A gigantic debris avalanche and its dynamics at Mount Ontake caused by the Naganoken-seibu earthquake, 1984. Proc. 4th Int. Conf. Field Workshop on Landslides, Tokyo, pp. 359-364.*
- Newman, JN (1977). *Marine Hydrodynamics, MIT Press, Cambridge, Mass.*
- Newmark, N.M. (1959) "A method for computation of structural dynamics", *Proc. American Society of Civil Engineers, 85. EM3. pp. 67-94.*
- Panton, R. L. (1984). *Incompressible Flow. John Wiley and Sons, Inc. New York.*
- Perla R, Cheng TT, McClung D (1980) *A two-parameter model of snow-avalanche motion. J Glaciol 26(94):197-207.*
- Schlichting, H (1979). *Boundary-layer theory, 7th ed. McGraw-Hill, New York, pp 598-641.*
- Shreve, R. L. (1968a). *The Blackhawk landslide: Geological Society of America Special Paper 108.*
- Shreve, R. L. (1968b). *Leakage and Fluidization in air-layer lubricated avalanches: Geological Society of America Bulletin. Vol. 79, pp 653-658.*
- Tacher, L. , Bonnard, C., Laloui, L. and Parriaux, A. (2005). "Modeling the behavior of a large landslide with respect to hydrogeological and geomechanical parameter heterogeneity". *Landslides. 2:3-14.*

- Tzavaris, G. (2000). Calculation of Complex Turbulent Flows. Southampton, Boston, WIT.*
- Terzaghi, K. (1950). Mechanism of landslides. Application of Geology to Engineering Practice (Berkey volume). New York. Geol. Soc. America. Pp. 83-123.*
- Voight, B. and Sousa, J. (1994). Lessons from Ontake-san: A comparative analysis of debris avalanche dynamics. Engineering Geology. Vol 38. pp 261-297.*
- Wagener, F. (1997). The Merriespruit Slimes Dam Failure: Overview and Lessons Learned. Journal of the South African Institution of Civil Engineering. Vol. 39(3), pp. 11-15.*